Université de Montréal

Advances in Calibration and Tracking Techniques for Pixelated Si Timepix3 Detectors

par

Constantine Papadatos

Département de physique

Faculté des arts et des sciences

Thèse présentée en vue de l'obtention du grade de

Philosophiæ Doctor (Ph.D.)

en Physique

July 14, 2023

Université de Montréal

Faculté des arts et des sciences

Cette thèse intitulée

Advances in Calibration and Tracking

Techniques for Pixelated Si Timepix3 Detectors

présentée par

Constantine Papadatos

a été évaluée par un jury composé des personnes suivantes :

Sjoerd Roorda

(président-rapporteur)

Claude Leroy

(directeur de recherche)

Jean-Francois Arguin

(membre du jury)

Luc Marleau

(examinateur externe)

Nikolay Kornienko

(représentant du doyen de la FESP)

Résumé

Cette thèse présente un travail ciblé sur les fonctionnalités d'un détecteur Timepix3 (TPX3) en ce qui concerne son utilisation dans le programme expérimental ATLAS-TPX3 au grand collisionneur de hadrons. Une évaluation directe d'un TPX3-Si a été complétée, ciblant plusieurs variables importantes connectées à la mesure du champ de radiation dans l'expérience ATLAS, par des études de retraçage de particules, de spectrométrie, ainsi que de stabilité du détecteur dans cet environment. Tout les résultats sont décrits dans trois publications formant la base de cette oeuvre.

Le Timepix utilisé dans cette thèse consiste en un senseur de silicium ayant une épaisseur de 500 μm divisée en 256×256 pixels. Chaque pixel a une aire de 55×55 μm^2.

La première étude porte sur la réponse du détecteur aux fluctuations de température qui ont été étudiées avec le but de déterminer la stabilité du détecteur dans le vide ainsi que dans des environments ou des situations dans lesquels les températures de matériaux entrant en contact avec le détecteur sont variables. Il a été observé que l'augmentation de la température correspond à une croissance dans la taille des amas de pixels. Cela indique que la température réduit le biais effectif interne, ce qui a comme conséquence la diminution de la zone de désertion, par la suite réduisant le champ électrique auquel sont soumis les porteurs de charge.

La deuxième étude vise à déterminer les paramètres affectant le regroupement des amas de pixels (clustering). Une technique impliquant l'utilisation de plusieurs faisceaux d'ions est appliquée pour déterminer l'effet de l'énergie ainsi que de la masse d'une particule sur la taille des amas de pixels, avec le résultat que les énergies plus élevées produisent des amas

plus grands. Pourtant, il est aussi trouvé que la taille des amas s'accroit aussi selon la masse des ions, bien que plus faiblement. Ces résultats ont des conséquences sur les algorithmes de retraçage qui sont cruciaux pour l'identification des particules.

La troisième étude décrit une évolution de la présente technique d'étalonnage en énergie utilisée dans le réseau de détecteurs ATLAS-TPX3. Des protons possédant des énergies entre 2-4 MeV sont utilisés comme particules d'étalonnage, dans le but de réduire la saturation de charge qui se produit aux énergies élevées dans chaque pixel, étant vue dans la technique d'étalonnage conventionnelle. Pour développer une extension de cette technique pixel-par-pixel, seules les hauteurs d'amas de ces protons sont gardées dans les amas, avec leurs énergies corrigées pour ajuster pour la perte de charge causée par la saturation. Appliquant ce nouvel étalonnage à des protons dans la gamme énergétique de 1,3 à 8,4 MeV, l'énergie reconstruite s'approche de la vraie valeur à 30% en moyenne. Les ions de lithium et de carbone dans la gamme énergétique de 8 à 25 MeV ont également été mesurés avec des énergies reconstruites améliorées.

Mots clés : Timepix3, Si, température, taille d'amas, étalonnage en énergie, ions

Abstract

This thesis presents research focused on the functionalities of a Tmepix3 (TPX3) detector as they relate to the operation of this device in the ATLAS-TPX3 experimental program at the Large Hadron Collider. A direct testing of one TPX3-Si detector is performed, focusing on several important variables relevant to the measurement of the radiation field in ATLAS through tracking and spectrometry, as well as stability of the detector in that environment. All results are described in the three publications which form the basis of this work.

This Timepix3 detector consists of a segmented Si sensor layer with a thickness of 500 μm divided into 256×256 pixels. Each pixel has an area of 55×55 μm^2.

The first study deals with the detector's response to temperature fluctuations that were studied with the aim of determining the detector's stability in vacuum as well as in environments or situations where contact temperatures can vary. It has been observed that temperature increases correspond to larger clusters and lower measured energies for protons measured over the course of this temperature increase. This indicates that, in effect, the temperature reduces the internal bias, decreasing the size of the depletion region and weakening the electric field to which charge carriers are subjected.

The second study focuses on parameters that affect clustering. A technique involving the use of multiple ions is developed to determine the respective independent effect of energy as well as particle mass on the sizes of clusters produced by those ions. It is found that energy is the primary driver in determining cluster sizes, with higher energy particles producing larger clusters. However, it is also determined that cluster size increases as ion mass increases, albeit

much more weakly. This has implications for tracking algorithms which are crucial to particle identification efforts.

The third study focuses on an adaptation to the current conventional energy calibration procedure used in the ATLAS-TPX3 network of detectors. Protons with energies between 2-4 MeV are used as calibration particles in order to reduce the impact of charge saturation that occurs at high per-pixel energies, seen in the conventional calibration. To achieve an extension to the current per-pixel technique, only the cluster heights of these protons are kept in the clusters, with their energies corrected to compensate for the lost charge due to saturation. When applying this new calibration to protons in the energy range of 1.3 - 8.4 MeV, the energy that is reconstructed approaches the true energy by 30% on average. Likewise, Li and C ions with energies in the range of 8 - 25 MeV were also measured with similarly improved energy reconstructions.

Keywords: Timepix3, Si, temperature, cluster size, energy calibration, ions.

Contents

List of tables

List of figures

List of abbreviations

AC   Alternating current

^{241}Am   Americium - 241

ASIC   Application-specific integrated circuit

ATLAS   A Toroidal LHC Apparatus

C   Carbon

CdTe   Cadmium telluride

CERN   Centre europeen de recherche nucleaire

CH   Cluster height

clk	clock
cm	centimeter
CMS	Compact Muon Solenoid
CS	Cluster Size
Cu	Copper
eV	electron-Volt
FWHM	Full-Width at Half-Maximum
GaAs	Gallium arsenide
GaP	Gallium phosphide
GeV	Gigaelectron-Volt

H	Hydrogen
He	Helium
IEAP	Institute of Experimental and Applied Physics
InSb	Indium antimonide
keV	kiloelectron-Volt
LAr	Liquid argon
LHC	Large Hadron Collider
^{6}Li	Lithium - 6
MeV	Megaelectron-Volt
Mg	Magnesium

MIP	Minimum Ionizing Particle
n	neutron
NIST	National Institute of Standards and Technology
ns	nanoseconds
p	proton
PET	Positron emission tomography
RBS	Rutherford Backscattering
SCT	Semiconductor tracker
Si	Silicon
SPECT	Single photon emission computed tomography

SRIM	Stopping and Range of Ions in Matter
Ti	Titanium
ToA	Time of Arrival
ToT	Time over Threshold
TPX	Timepix
TPX3	Timepix3
TRT	Transition radiation tracker
USB	Universal Serial Bus
V	Volt
VdG	Van der Graaff

XRF	X-Ray Fluorescence
ZnS	Zinc sulfide
Zr	Zirconium
α	alpha particle
μm	micrometer

Acknowledgements

I would like to thank my PhD supervisor, Prof. Claude Leroy, for having given me the opportunity to work on this project and for his guidance and insight throughout. Appreciation and gratitude go to Prof. Jean-François Arguin for his help in facilitating many important challenges over the course of this degree. Thanks to my former research and office colleague, Thomas Billoud as well as to all my colleagues in the *bunker*, in the *Groupe de Physique des Particules*, and at the IEAP in Prague for their help and company — in particular Benedikt Bergmann and Yesid Mora for sharing with me their technical expertise and time during my stays in Prague.

Thanks and appreciation go out to Chen Wen Chao, without whom I would likely still be debugging software issues to this day. Thanks to Louis Godbout for managing the Tandem accelerator, providing the particle beams, and helping with any hardware issues related to experimental setups.

I wish to thank Serena Sinno, for her indefatigable encouragement during this PhD. Lastly, I thank my parents, Olga Zafiriou and Dimitrios Papadatos, for a lifetime of guidance and support that has led to this work.

For my parents

Introduction

Particle tracking and calorimetry together form the two pillars of detection in experimental particle physics. At the LHC, the ATLAS experiment [1] is an enormous network of detectors that each serves one of those two roles. The TPX3 [2] network of silicon detectors located within the ATLAS detector and on the ATLAS cavern walls allows one to measure the radiation environment inside the ATLAS detector and its environment during collisions, and in real time [3]. The network also allows for the measurement of the proton head-on collision, luminosity, and of the collision background. As a hybrid pixelated tracking detector, capable of measuring particle energy, these detectors also present a number of possibilities related to the future of particle detectors to be used in such large scale collision experiments.

Si detectors are widely used in particle physics because of their long history of development, fabrication and the bulk of research dedicated or associated to them. Of all semiconductor materials, they are also the most commonly produced and, as a consequence, possess few lattice impurities when compared to other semiconductor materials like GaAs or CdTe, whose production methods have not been as refined over the years by comparison [4, 5].

Beyond uses in particle physics, medical applications in SPECT and in PET are also possible and commonplace [6]. The ability to measure precisely the energies of photons from a few tens to hundreds of keV allows the measurement of photons in these imaging devices. Si detectors are also used in space, in satellite experiments, and on the International Space Station as a dosimeter sensor material, not to mention the numerous applications of silicon as a material in computer electronics and consumer goods [7, 8, 9, 10, 11, 12].

When an ionizing particle interacts with the sensor of a silicon particle detector, a charge cloud is created made up of free charges possessing either negative or positive charge (electrons or holes, respectively). A bias voltage applied across the electrodes triggers the drift of these two types of charges in opposite directions. The speed with which each charge drifts towards the electrode depends on a number of factors: the bias voltage, the structure of the crystal lattice of the material, and its temperature[**13, 14, 15**].

The macroscopic result of these charge drifts from the experimenter's point of view is the formation of particle clusters — regions of pixels that can be recognized as belonging to a group, representing a common particle event. For the experimenter, the detector's ability to correctly identify particles, their trajectories, and their energies is what is ultimately of interest. Therefore, an understanding of the influence of each process affecting this drift is vital.

In practice, temperature stability is of great importance to the functioning of any detector, whether it be positioned in a vacuum-like environment like that of space or in air, as it is in large accelerator experiments, where it is often in contact with other electronic or structural components that can heat up or cool down during long term operation. Temperature variations not only can have negative effects on the presence of electronics noise in a detector, but may even lower the particle identification and reconstruction efficiency in pixel detectors [**5**]. Similarly, as energy calibrations are almost always performed at a single constant temperature (usually room temperature), a detector which is subject to an environment where its temperature can undergo change will be compromised insofar as its ability to reconstruct deposited energy is concerned [**16**].

A detector with spectroscopic capabilities should also be able to accurately reconstruct incident particle energies. For a high granularity pixel detector, this poses a challenge due to the creation of large amounts of charge carriers concentrated in small pixel volumes. The resulting charge saturation [**19**], caused by the charge acceptance threshold of the detector chip's electronics can cut off the total measured energy in that pixel and reduce the overall measured energy of the particle event, once the energies of all such saturated pixels are

summed. Remedying this through a corrective calibration is the most immediate practical solution in the absence of improved electronics developments.

A multi-faceted investigation into each of these phenomena is not only of interest, but is necessary for the continued use of these TPX3 detectors in experiments such as ATLAS, where these types of studies cannot be done.

0.1. Structure of the Thesis

An overview of detection principles in particle physics is presented in the first chapter, placing the Timepix3 detectors in the ATLAS context. The second chapter provides a detailed look at important principles in the interaction of particles with matter, using silicon as the material through which these topics can be discussed. Chapters 3, 4, and 5 present the main research that was performed during this doctorate, organized in three journal publications along with dedicated explanatory sections. The first of the three papers discusses the temperature stability of the TPX3 device during extended operation [20]. The second paper provides a comprehensive survey of the parameters affecting cluster properties, and by extension, builds off of the first paper's results [21]. The final paper presents a method for high energy calibrations which can be used in tandem with the conventional calibration techniques employed by the ATLAS-TPX collaboration [22].

Chapter 1

Detection in Particle Physics

The applications of semiconductors as particle detection materials vary widely from medical through to space environments [**23, 24, 25, 26**]. They are primarily used in particle physics experiments as trackers, as in the ATLAS and CMS experiments at the Large Hadron Collider (LHC) at CERN, but also as dosimeters to measure radiation fields and personal dose rates for individuals working in high radiation environments [**27**]. Silicon, in particular, is a popular sensor material due to its historical association with the field and the research and development which centred around it.

1.1. Classification of Semiconductors and Band Structure

Semiconductors can be classified into three large families corresponding to their position on the periodic table. Group IV materials display a tetragonal binding structure, with four valence electrons. These are referred to as elemental semiconductors [C, Si, Ge] and their crystal lattice is characterized by a diamond structure, as shown in Figure 1.1.1.

The second family of materials occupies the III-V group and possesses a cubic crystal (*zincblende*) structure, again with tetragonal bonds. The members of this group are GaAs, InSb, GaP, etc. Lastly, in the II-VI group materials such as CdTe and ZnS can be found.
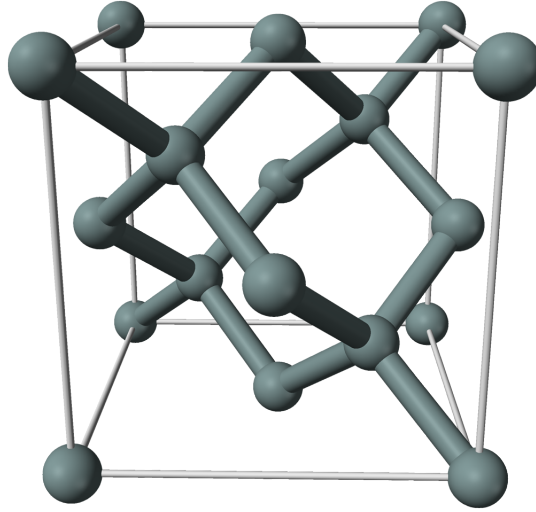
Fig. 1.1.1. A unit cell showing a diamond lattice structure.[**29**]

These semiconductors also possess cubic (*zincblende*) structures. The bonds of these materials are also covalent and ionic, but are even more ionic than those of group III-V [**28**].

At temperature $T = 0$ K, a semiconductor contains energy bands that are either completely empty in the case of the conduction band, or completely full, in the case of the valence band. The electrons occupy the valence band completely while the conduction band remains empty. Between the valence and conduction bands exists a band gap, a range in energy that must be overcome by an excited electron to participate in electrical conduction.

Figure 1.1.2 illustrates the differences between metals whose energy bands overlap, semiconductors and insulators in the context of energy bands. The conduction and valence bands are indicated in blue and red respectively. The position of these bands with respect to the Fermi level dictates how charges are conducted within the material. For conduction to occur, electrons are displaced from the valence band to the conduction band. For alkaline-earth metals, the two bands overlap, thus the energy required to excite an electron is small. For these materials, conduction can result simply by thermal excitation. Other metals posses partially filled valence bands. Consequently, the electrons in these bands are also free to move, leading to conduction. In the case of insulators, the large separation between the bands prohibits electrons from jumping from the valence band to the conduction band.
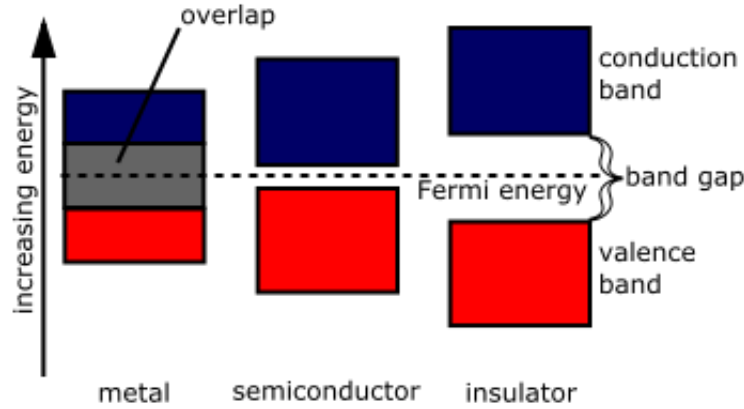
Fig. 1.1.2. A comparison between the position of the energy bands of a metal with over-lapping valence and conduction bands, a semiconductor and an insulator with respect to the Fermi energy. [**30**].

The bands of a semiconductor do not overlap as they do in metals, yet their separation in energy is not nearly as wide as it is for insulators. Their band gap is on the order of a few eV, which significantly limits conduction by thermal excitation but also allows for conduction by virtue of the energy transferred by radiation entering the material.

Compared to metals, the density of charge carriers in a semiconductor is far lower and depends greatly on the temperature of the material. Only the valence and conduction bands play any role in the overall conduction process, while the energy bands that are found above the conduction band and below the valence band play no part whatsoever [**28**].

1.2. Electrical Conductivity and Mobility

The current density j of a semiconductor with respect to its electrical conductivity, σ, and the electric field, $\vec{E}$, to which charges are subjected, is given by [**28, 31**]

$$j = \sigma|\vec{E}| \tag{1.2.1}$$

The electric field causes charge carriers to drift with a velocity

$$\vec{v}_{de,h} = \mu_{e,h}\vec{E} \tag{1.2.2}$$

with a mobility, expressed in $cm^2V^{-1}s^{-1}$,

Material	Electrons	Holes
Si	1350	480
GaAs	8000	300
Ge	3600	1800

Table 1.2.1. Mobility values of common semiconductors at 300 K, expressed in $\text{cm}^2\text{V}^{-1}\text{s}^{-1}$.[**31**]

$$\mu_{e,h} = \frac{q_{e,h}\tau_{e,h}}{m_{e,h}}, \tag{1.2.3}$$

$m_{e,h}$ and $\tau_{e,h}$ are the mass and the lifetime of the electron or the hole. The lifetime represents the elapsed time prior to which the charge carrier undergoes a collision or is captured by a trap in the crystal lattice [**32**]. For Si, the lifetime of carriers is comparatively high because of this, as sample fabrication techniques have been improved over its many years of use. A few mobility values for common materials are presented in Table 1.2.1.

1.3. Properties of Si

1.3.1. The Absorption Process

Si possesses an indirect band gap, meaning that the trough of the conduction band does not lie directly above the peak of the valence band. The band width is the difference in energy between these two points. Figure 1.3.1 shows and compares the basic energy band structure of direct and indirect band gaps.

In fundamental absorption, an electron absorbs an incident photon and jumps from the valence band to the conduction band. This photon must have an energy greater than or equal to the energy of the band gap. Its frequency must therefore be

$$\nu \geq \frac{E_g}{h} \tag{1.3.1}$$

where E_g is the energy of the band gap. For a material possessing an indirect band gap, like Si ($E_g = 1.12$ eV)[**31**], the electron cannot make the transition between bands in the
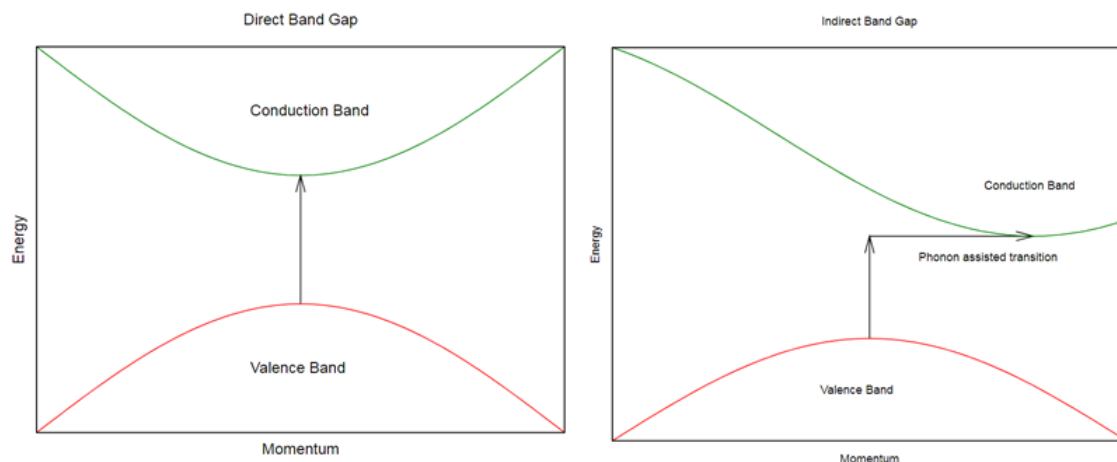
Fig. 1.3.1. a) A direct band gap, like for GaAs. b) An indirect band gap, like for Si. The photon absorption process is illustrated for each case with an arrow indicating the transition of an electron from the top of the valence band to the bottom of the conduction band.[**33**]

same way. In this case, the process takes two steps. The electron absorbs a photon and a phonon [1] simultaneously. The photon provides the energy necessary to make the jump while the phonon provides the momentum required to transition to the bottom of the conduction band.

1.4. The TIMEPIX3 Detector

The Timepix3 (TPX3) detector [**2**], presented in Figure 1.4.1, is a pixelated semiconductor detector that is a member of the Medipix/Timepix family of hybrid pixel detectors which in some iteration have been installed in the ATLAS cavern since 2008 [**34, 35, 36**]. In this study, the detector used is made up of a sensor layer of 500 μm which is connected by bump-bonding to a readout chip. The Si chip is equipped with a common backside electrode and with a matrix of electrodes (256 $\times$ 256 pixels squared, each with an area of 55 $\times$ 55 μm^2) on the front side. Figure 1.4.2 shows the different components of the TPX3. Each pixel contains its own amplification circuit, composed of a preamp, a discriminator and a counter. The Timepix3 electronics scheme is shown in Figure 1.4.3.

---

[1]A phonon is a quasi-particle corresponding to an excitation of the vibrational energy of the crystal lattice

Fig. 1.4.1. A Timepix3 detector equipped with a Katherine readout system interface.
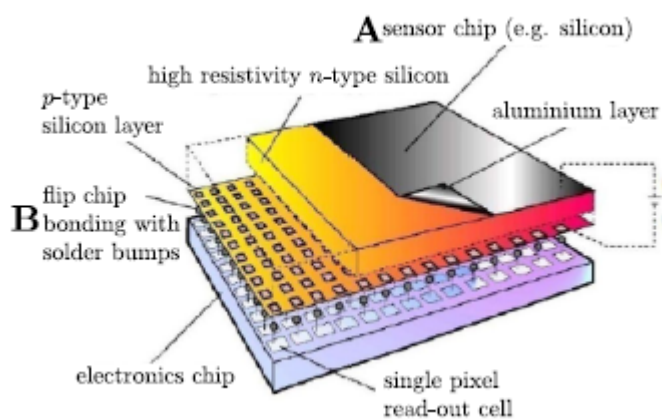
Fig. 1.4.2. A Timepix detector. (A) is the semiconductor sensor layor. (B) shows the readout chip and the electronic bump bonds.[**35**]

The device is connected with a Katherine readout system [**38**], which is then connected to a computer via ethernet cable. The data acquisition and device control is done using the *Burdaman* software.
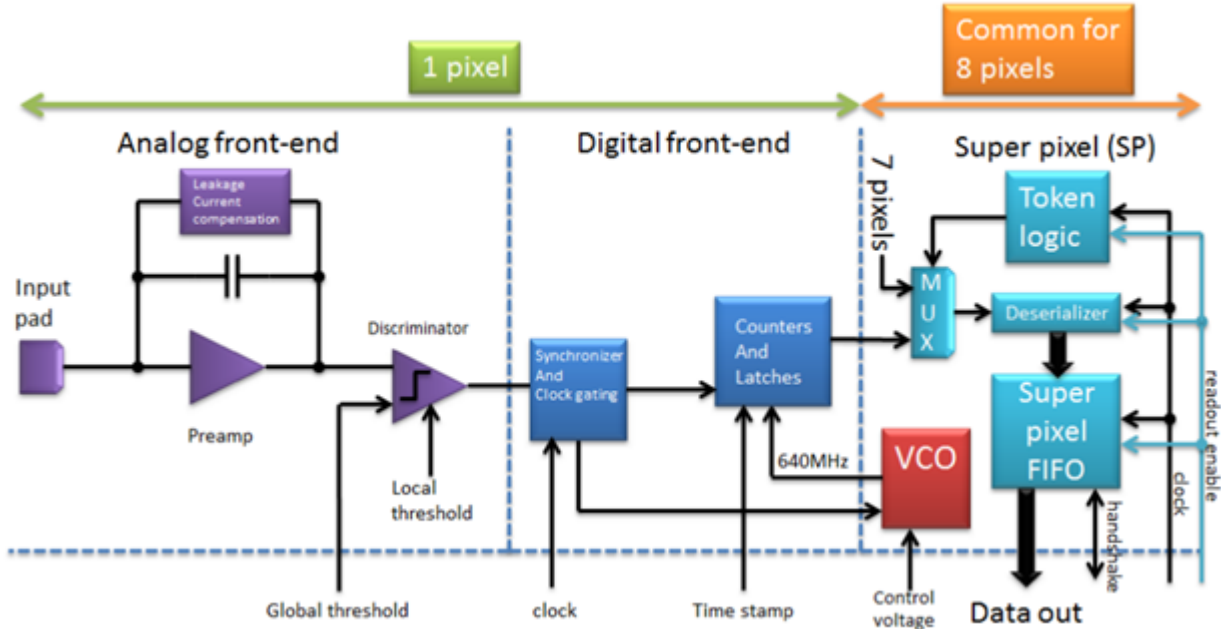
Fig. 1.4.3. The electronics scheme of a single pixel in a Timpepix3 detector.[**2**]

The charges produced from electron-hole pair creation migrate towards the electrodes under the influence of an electric field induced by the bias voltage applied across the detector. At the cathode of each pixel, the charge is collected and the signal is amplified by the current amplifier. This signal is then compared to a threshold. If it is greater than the threshold, the counter increments by 1, otherwise it stays at 0. Unlike the frame based acquisition of previous Timepix-Medipix generations, TPX3's acquisition is data-driven. Once a pixel is hit, the dead time until the next possible hit is 475 ns. This leads to the possibility of measuring up to 40 million hits cm^{-1} s^{-1}.

The adjacent pixels that also have counter values greater than 0 are collectively called a *cluster* or a *track*, whose shape depends upon the type of interaction of the incident particle with the detector's active layer. The shape varies according the energy, the incidence and the species of the particle. It is by studying these shapes that particle identification is possible. Examples of clusters are shown in Figures 1.4.4a and 1.4.4b.

The measurement of events can be accomplished in three possible modes of operation: 1) tracking and counting mode, 2) ToT (*Time-over-Threshold*) mode and 3) ToA (*Time of Arrival*) mode. An important distinction between TPX and TPX3 is that, in the latter,
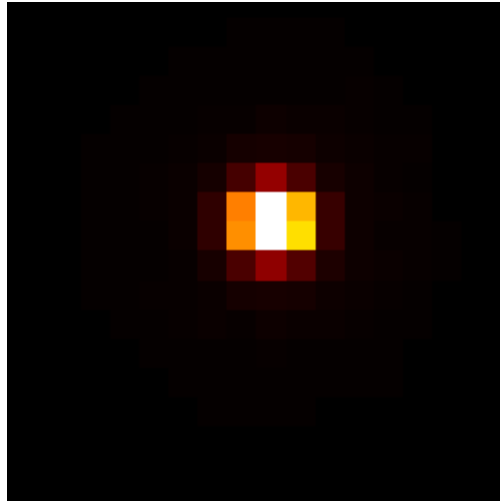
(a)
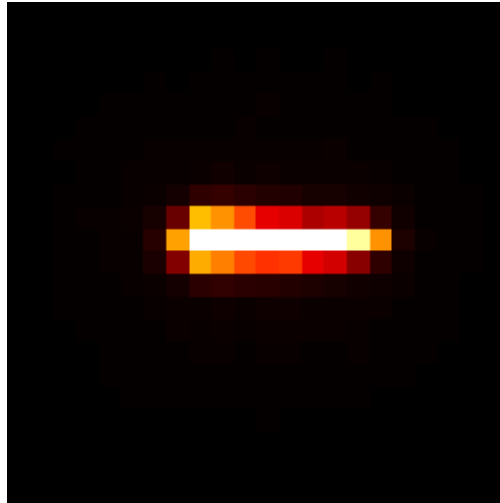
(b)

Fig. 1.4.4. 8 MeV proton clusters measuring ToT (time-over-threshold) for (a) normal incidence and (b) 75° incidence.

the ToT and ToA modes can be operated simultaneously. In ToT mode, an internal clock counts the time during which the signal is above the threshold. This clock operates at a defined frequency of 10 MHz. The maximum clock frequency achievable with a TPX3 is 40 MHz, however, 10 MHz has been applied in this work to conform to the settings used for the TPX3 network of detectors in ATLAS, which operate under low power settings. Thus, the TOT values obtained are simply the clock frequency multiplied by the measured time. It is, therefore, possible to measure energy values of incident particles using an appropriate ToT-energy calibration. ToA mode allows one to perform coincidence measurements with the
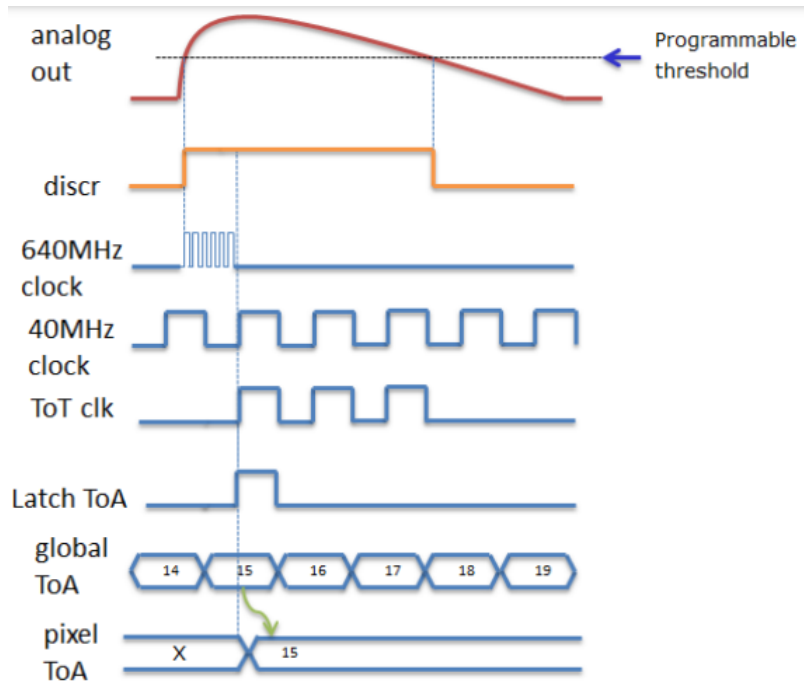
Fig. 1.4.5. The operational principle in a TPX3 pixel for an event caused by an incident charged particle. Once the signal achieves the threshold value, the 640 MHz clock counts up until the beginning of the next ToT clock interval, determined by the constantly running 40 MHz clock. At this point the ToT registers its first non-zero value. The ToA clock counts time continuously during the pixel's entire operation and assigns a time stamp (pixel ToA) once the ToT clock (ToT clk) begins its count. [**2**]

aim of measuring time of flight (ToF). The operation principle of the TPX3 is summarized in Figure 1.4.5.

1.5. The ATLAS detector

One of the two general-purpose experiments at the Large Hadron Collider is ATLAS [**1**] (the other one being CMS). It has been tasked, since the measurement of first beams at the LHC, to probe new physics. It is composed of a large barrel region made up of concentric cylindrical detector arrays that span 50 m in diameter and 44 m in length as shown in Figure 1.5.1.
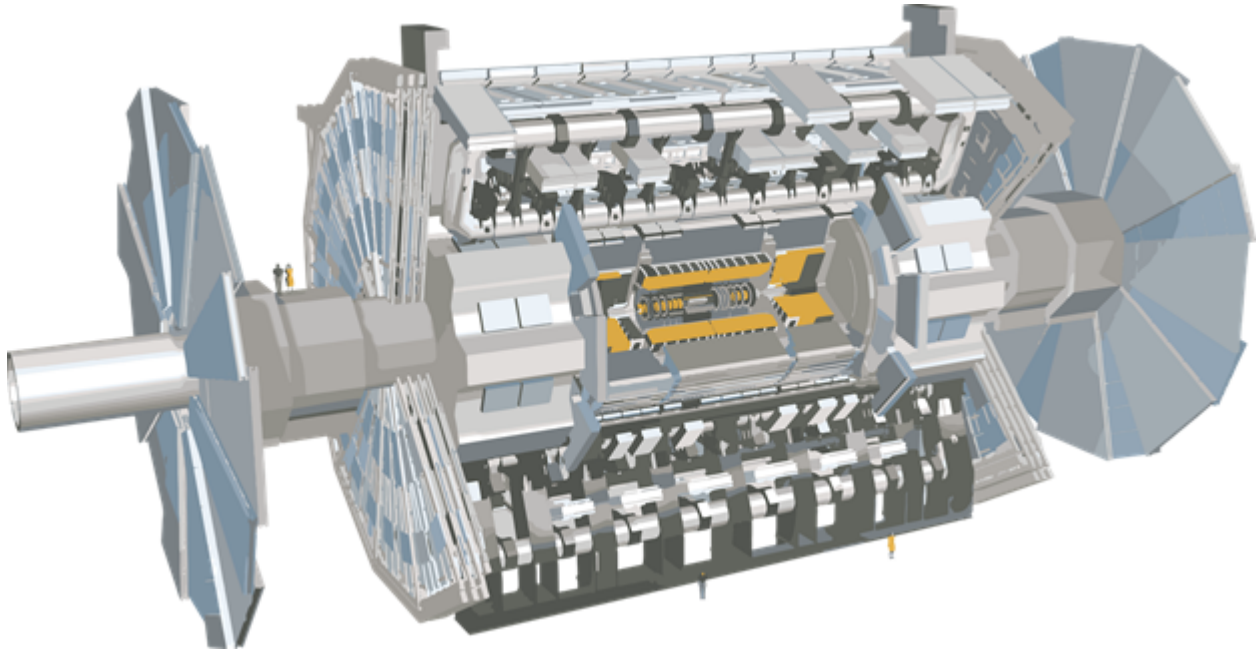
Fig. 1.5.1. The ATLAS detector [**37**].

In its central barrel region, the inner tracker can be found. The detectors that form this region have high spatial granularity for the purposes of precise track reconstruction and ver-texing. At the innermost of these layers is the pixel detector, followed by the semiconductor tracker (SCT), and lastly the transition radiation tracker (TRT), moving radially outwards.

Continuing outwardly from the central axis of the cylinder, the calorimeters make up the next layers. The innermost of these layers is the electromagnetic calorimeter, composed of liquid argon and lead as active and passive absorber layers respectively. Layers of these are also positioned on the end cap and forward regions. The Tile barrel surrounds the barrel LAr layer and is designed as the hadronic calorimeter, with scintillator tiles and steel as active and passive absorber layers. The ATLAS forward calorimeter has LAr as an active medium and tungsten as a passive medium.

Finally, the last detection layer is the muon spectrometer, which is integrated with three large toroidal magnets. It allows for the high precision tracking of muons exiting the barrel region.

Chapter 2

Interaction of Particles with Matter

2.1. Direct Ionization

Particles such as electrons, protons and α-particles (alphas), as well as other ions, directly ionize the matter through which they pass. They lose their kinetic energy over the course of their path through collisions or radiative processes. The energy loss of these particles over the distance travelled is quantified as the stopping power $-dE/dx$,

$$\frac{dE}{dx} = \left(\frac{dE}{dx}\right)_{col} + \left(\frac{dE}{dx}\right)_{rad} = \left(\frac{dE}{dx}\right)_{elec} + \left(\frac{dE}{dx}\right)_{nucl} + \left(\frac{dE}{dx}\right)_{rad} \qquad (2.1.1)$$

The collision stopping power, $(-dE/dx)_{col}$, is composed of two parts. The first part describes collisions between the particle and the atomic electrons, $(-dE/dx)_{elec}$. The second part describes nuclear collisions, $(-dE/dx)_{nucl}$. The interaction cross-section with electrons is much greater than that for nuclear interactions at high energy (E > 100 keV),

$$\left(\frac{-dE}{dx}\right)_{elec} \gg \left(\frac{-dE}{dx}\right)_{nucl}, \qquad (2.1.2)$$

as is shown in Figure 2.1.1.

Heavy particles, such as protons, alphas, and other ions, undergo substantially greater energy losses due to collisions than those produced by radiation. For lighter particles like electrons or positrons, radiative losses become increasingly important at energies greater than 10 MeV. The energy loss by collisions represents losses from excitation and ionization.
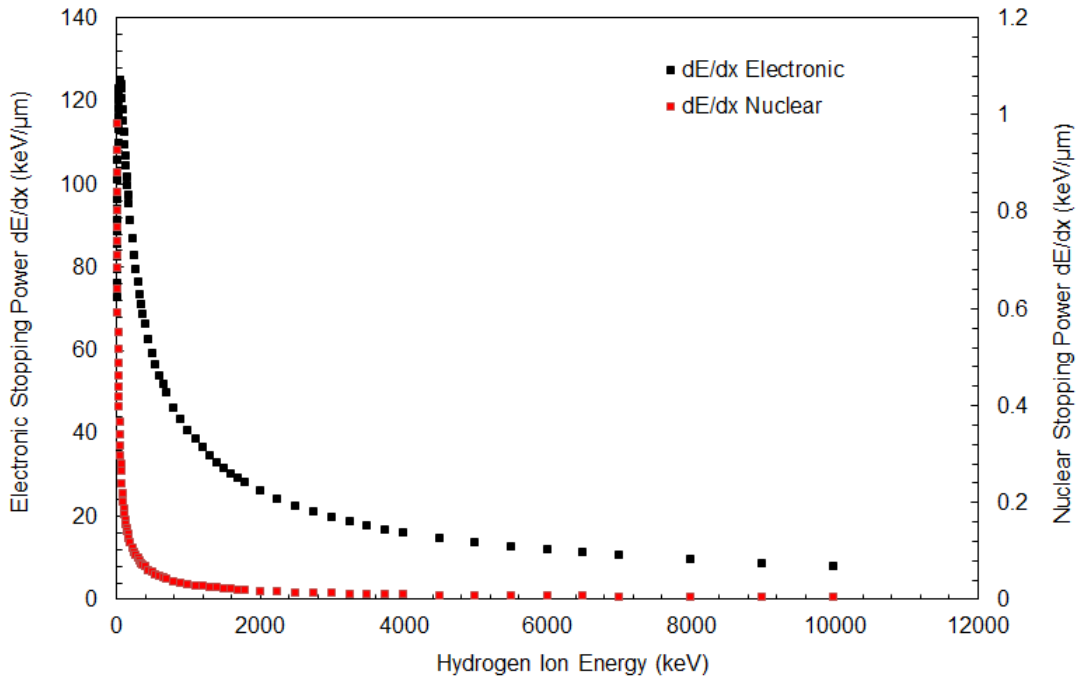
Fig. 2.1.1. The electronic (black) and nuclear (red) stopping powers for hydrogen ions in Si. The contribution of dE/dx_{nucl} is small compared to dE/dx_{elec}. The plot is graphed based on data from the SRIM program.[**39**]

Excitation is the process that moves an electron from a given shell to a more energetic shell. Consequently, an incident particle can lose energy without removing an electron from an atom. Ionization removes one or more electrons from the atom. It creates electron-hole pairs in a semiconductor and electron-ion$^+$ pairs in a gas. The number of pairs created is given by the ratio (E/ϵ) of the energy, E, deposited by the particle in the material and ϵ, the energy required to create a pair. ϵ varies from one material to another ($\epsilon_{Si} = 3.62$ eV et $\epsilon_{Ar_{gas}} = 26.4$ eV)[**40**].

2.1.1. The Bethe-Bloch Equation

The average rate of energy loss per unit length of a heavy charged particle is given by the Bethe-Bloch equation [**41**] which assumes 1) that the mass of the incident particle is greater than that of an atomic electron and 2) that the motion of the atomic electron is negligible. If T_{max} is defined to be the maximum energy transferred to an atomic electron by a massive charged particle,

$$T_{max} = 2m_e c^2 \beta^2 \gamma^2 \left(1 + 2\gamma \frac{m_e}{M} + \frac{m_e^2}{M^2} \right)^{-1} \tag{2.1.3}$$

$\gamma^2 = (1 - \beta^2)^{-1}$ is the Lorentz factor, m_e is the mass of the electron, M is the mass of the incident particle and $\beta = v/c$ (i.e., the speed of the particle in units of the speed of light). When the mass of the incident particle is much greater than the mass of the electron, $M \gg m_e$ and when γ is not very large, (2.1.3) becomes

$$T_{max} \approx 2m_e c^2 \beta^2 \gamma^2 \tag{2.1.4}$$

The Bethe-Bloch equation gives the average energy loss per unit length:

$$-\frac{dE}{dx} = 4\pi N_A r_e^2 m_e c^2 \frac{Z}{A} \rho \frac{z^2}{\beta^2} B \tag{2.1.5}$$

where the factor B is given by

$$B \equiv \ln \left(\frac{2m_e c^2 \beta^2 \gamma^2 T_{max}}{I^2} \right) - \beta^2 - \frac{\delta}{2} - \frac{C}{Z}. \tag{2.1.6}$$

Z is the atomic number of the target atom, A is its atomic mass, N_A is Avogadro's number, ρ is the atomic density and z is the electric charge of the incident particle. The classical electron radius is defined as $r_e = e^2/m_e c^2 = 2.82 \times 10^{-13}$cm. I is the average ionization energy. The factor δ takes into account the shielding of atomic electrons through density effects in the material. This is due to polarization of the atomic electrons by the electric field created by the incident particle. Inner shell electrons are not sensitive to this field and, as a consequence, contribute less to the energy loss. The C/Z term is associated with the non-participation of inner shell electrons (primarily coming from the K-shell) in the collision process at low energy[42]. This shielding effect is produced when the incident particle has a speed that is, at its maximum, comparable to the orbital speed of atomic electrons. It is at these speeds that the assumption of a stationary electron with respect to the incident particle becomes invalid. On the whole, the contribution of this correction is relatively small.
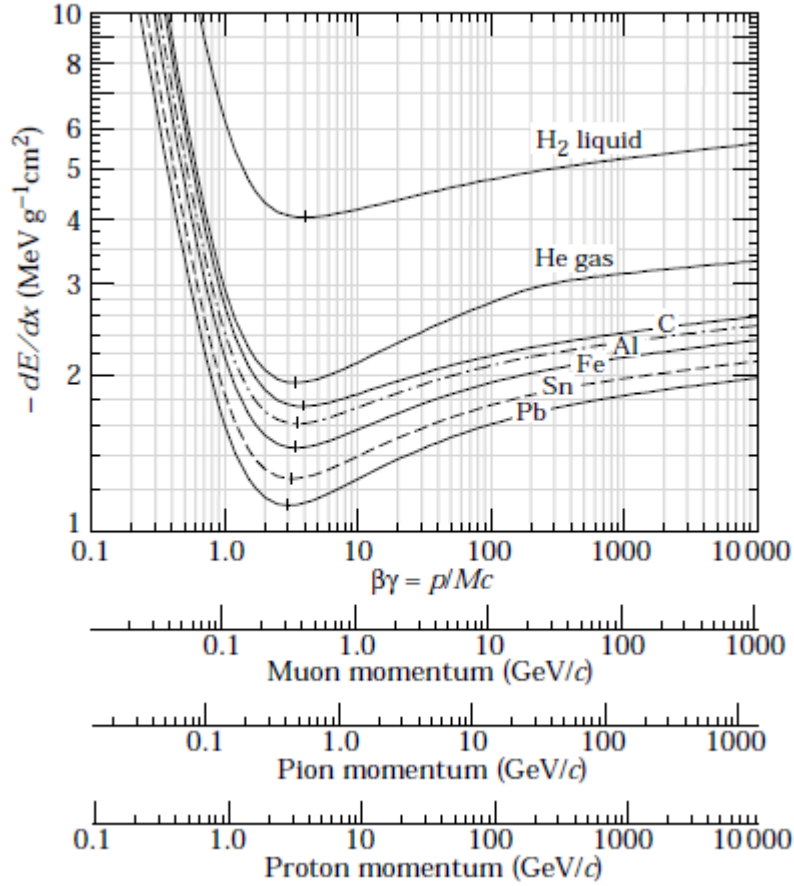
Fig. 2.1.2. The rate of average energy loss in various materials. The energy of minimum ionization of each aligns roughly at the same value (3.5 MeV). Different particles (muon, pion and proton) become MIPs at different momenta.[**45**]

2.1.2. Minimum Ionizing Particles (MIPs)

Energy loss is not strongly dependent on the mass of the incident particle unless its mass is much greater than that of an electron. The stopping power $(-dE/dx)$ is proportional to z^2/β^2 where z is the particle's charge. The stopping power depends on the absorber, according to Z/A. The quantity dE/dx is at a minimum when $\beta\gamma \approx 3.5$, as shown in Figure 2.1.2. Particles that undergo a minimal energy loss are called minimum ionizing particles, or MIPs. The rate of average energy loss of particles in different materials is shown in Figure 2.1.2.

Particle identification is possible if one measures the stopping power and momentum ($\beta\gamma = p/Mc$, where $p[\text{GeV/c}] = 0.3B[T]R[m]$, and R is the curvature of the magnetic field B).

For example, the proton, whose mass is close to the GeV scale (938 MeV/c^2), must have a kinetic energy of many GeV in order to become a MIP. For an electron, whose mass is 0.511 MeV/c^2, only a few MeV (~ 2 MeV) are necessary. The stopping power's value at minimum ionization is roughly the same for all particle's possessing the same charge. However, each particle attains minimum ionization with a different momentum, as is seen in Figure 2.1.2, which allows for its identification. A particle with a charge $z \geq 2$ (α-particle, $z = 2$) has a rate of loss that is larger because of the proportionality of $-dE/dx$ to the square of the charge. Such a particle can become a MIP for much higher energies, as is the case with cosmic rays or in relativistic energy ion accelerators.

2.1.3. Bragg Curve and Range

Due to the dependence of dE/dx on $1/\beta^2$ for heavy charged particles, these particles lose the majority of their energy immediately before being completely stopped in the medium. Bragg curves can be observed in TPX3 measurements of heavy particles that are incident at high angles by plotting the deposited energy over the pixel area that is activated by the incident particle. This is seen in Figure 2.1.3, where a proton, incident on the detector at 75° is shown as a track event in various representations. The particle's range is its distance travelled for a given energy in a given material. It is obtained experimentally by sending a monoenergetic beam of particles across layers of identical materials of different thickness. The current of particles transmitted across the layer is compared to the initial intensity of the beam. Figure 2.1.4 illustrates the difference between the ranges of heavy and light charged particles. Heavy particles are not subject to strong deviations from their trajectories because only a small fraction of kinetic energy is lost with each Coulomb interaction of the particle with an electron.
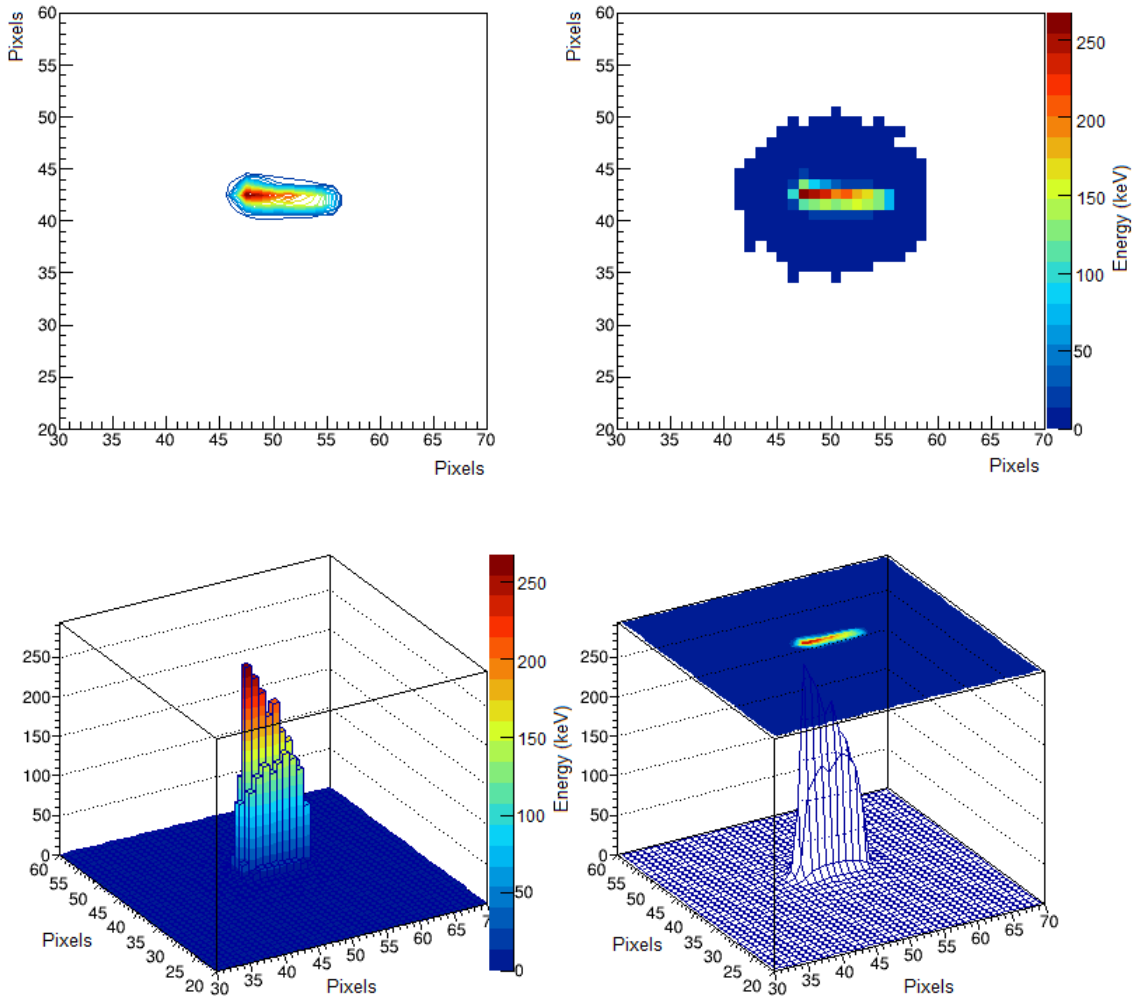
Fig. 2.1.3. A measured 8 MeV proton incident at 75° on a TPX3-Si detector. The proton track is displayed as a so-called "cluster volume" where the measured energy in keV is plotted on the vertical axis for each pixel.

In practice, the statistical nature of the energy loss causes fluctuations in the value of the range of the particle across a material. These fluctuations manifest themselves as lateral and longitudinal *straggling*[43]. Consequently, two identical particles having the same initial energy and travelling through the same material will not lose the same amount of energy along their trajectory and will therefore not have the same range values. The range is expressed as a Gaussian distribution. The straggling effect diminishes with an increase of the particle's mass.
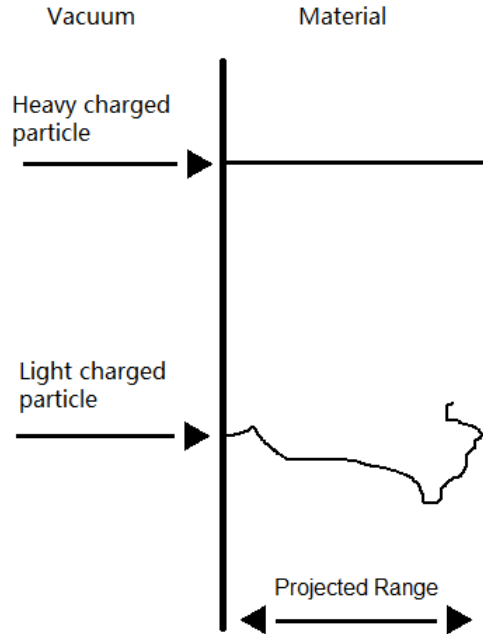
Fig. 2.1.4. The difference between the trajectories of heavy and light charged particles.

In determining the Continuous Slow Down Approximation range, the rate of energy loss along the length of the range is assumed to be equal to that of the total stopping power. It is thus calculated by integrating the inverse of the Bethe-Bloch formula [**44**].

$$R\left(E_0\right) = \int_{E_0}^0 \frac{1}{-\frac{dE}{dx}} dE \qquad (2.1.7)$$

2.1.4. Electrons and Positrons

For electrons and positrons, whose mass is much smaller than that of a proton, the radiative losses (bremsstrahlung) are much more significant at energies ≥ 10 MeV.[1] In addition, $(dE/dx)_{col}$, given by Bethe-Bloch is also modified because the incident particle possesses the same mass as the atomic electron. It can then no longer be assumed that the motion of the atomic electron is negligible compared to the incident electron. The effects, including bremsstrahlung, that contribute to the total energy loss per radiation length (X_0) for electrons and positrons are presented in Figure 2.1.5. Up to 0.255 MeV, electron or positron scattering occurs through ionization. Above 0.255 MeV, losses result from Bhabha and

---

[1]Bremsstrahlung is the radiation created by the acceleration of electric charges.
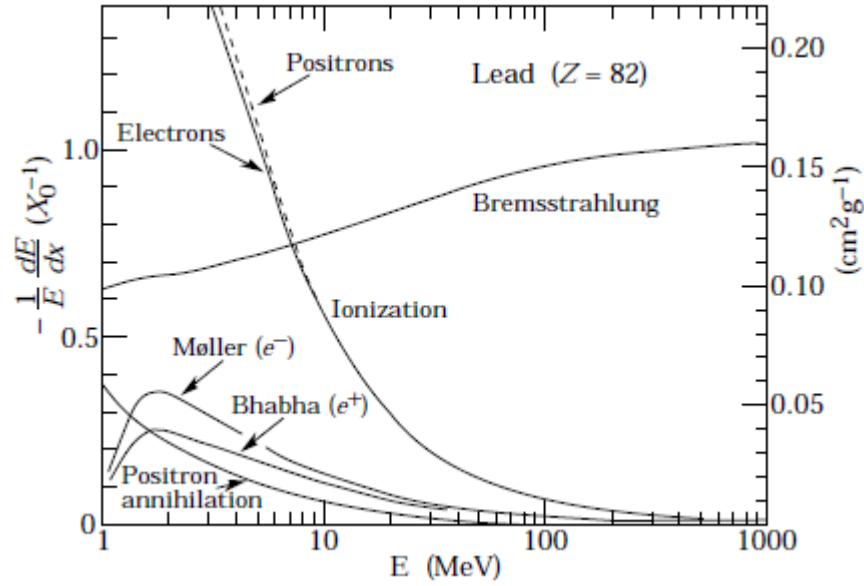
Fig. 2.1.5. The energy loss per radiation length, X_0 (see Eq. (2.8)) in lead as a function of the electron or positron energy, for the indicated interactions.[**45**]

Moller scattering for electrons and positrons respectively. For electrons, the radiation length is defined as,

$$X_0 = \frac{A}{4\alpha N_A Z^2 r_e^2 \frac{\log 183}{Z^{1/3}}}, \tag{2.1.8}$$

where α is the fine structure constant of the electromagnetic force.

2.2. Indirect Ionization

Photons interact indirectly with matter according to three principle interaction processes. These interactions are photoelectric absorption, Compton scattering and pair production. The dependence on the energy and on the atomic number of the absorber dictates which process dominates. This is illustrated in Figure 2.2.1. Thus, for a silicon sensor, the dominant interaction is the photoelectric effect up to photon energies of roughly 50 keV. Above that, up to about 10 MeV, Compton scattering is the main interaction. Indeed, the photoelectric contribution is insignificant above 1 MeV. For energies greater than 10 MeV, the pair production cross section is higher than the one for the Compton process. This is expressed visually in Figure 2.2.2.
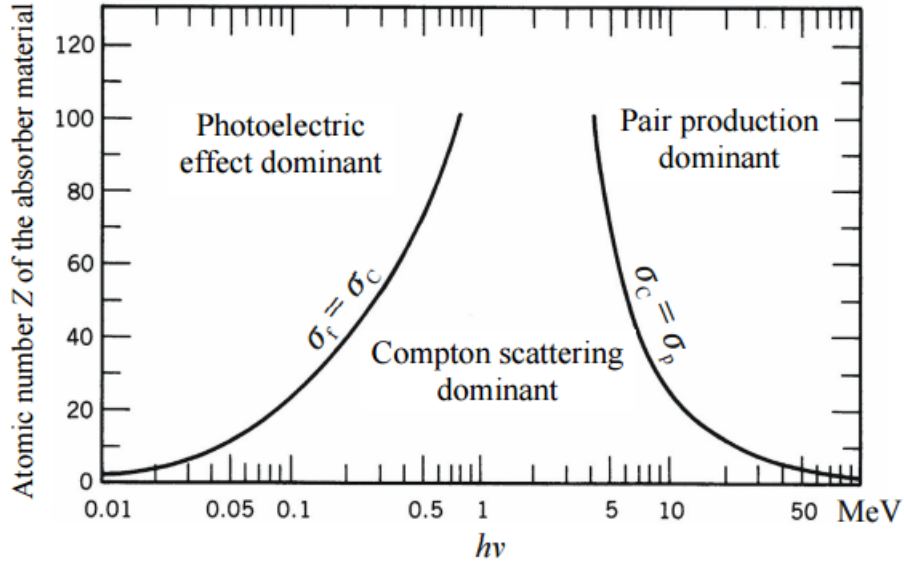
Fig. 2.2.1. The cross sections of the three principle interactions of photons with matter. The dominant interaction depends upon the energy of the photon $(h\nu)$ and the atomic number (Z) of the material.[**46**]
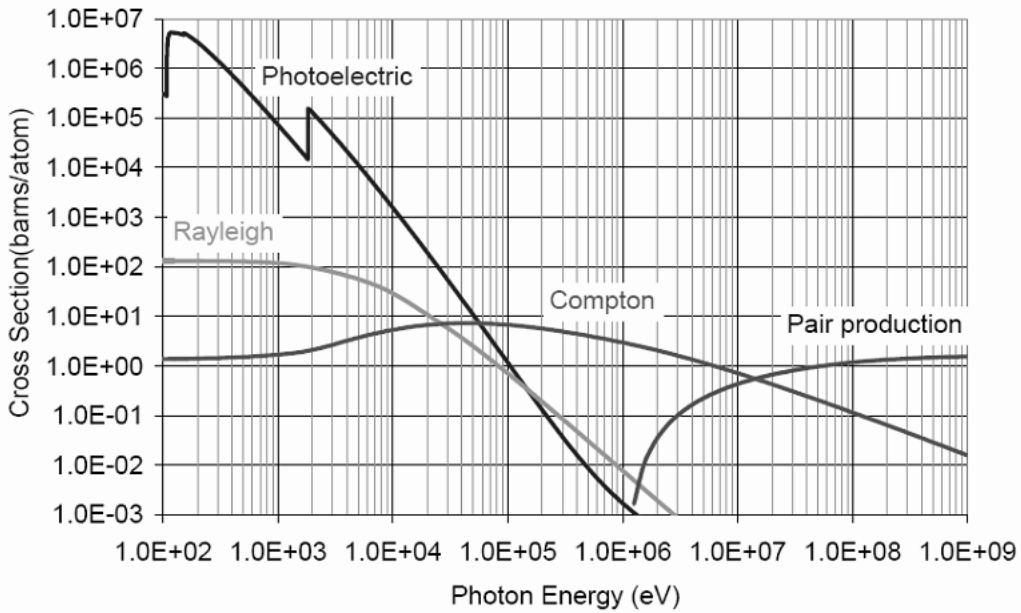
Fig. 2.2.2. The cross sections of the photoelectric, Compton, pair production and Rayleigh interactions for photons in silicon. For low energy photons, the photoelectric process, followed by Compton scattering are the two ionizing modes of interaction with the material. For higher energy photons (above about 1 MeV), Compton scattering and pair production will be more important, with the latter dominating above 10 MeV. [**47**]

2.2.1. The Photoelectric Effect

Photoelectric absorption occurs when an incident photon of energy E_γ interacts with an atomic electron. The photon is converted into a photoelectron with kinetic energy $KE = E_\gamma - BE_i$, where BE_i is the binding energy of the electron to the i shell. This is the dominant effect for low energy photons, typically less than ~ 50 keV. The resulting photoelectrons also possess low energies. The binding energy depends on the atomic number Z and on the electronic shell. The binding energies of the K, L and M shells are given by,

$$BE_K = Ry(Z-1)^2 eV \tag{2.2.1}$$

$$BE_L = \frac{Ry}{4}(Z-5)^2 eV \tag{2.2.2}$$

$$BE_M = \frac{Ry}{9}(Z-13)^2 eV \tag{2.2.3}$$

where $R_y = 13.62$ eV is the Rydberg constant.

When the photon energy increases, electrons having higher binding energies and which are located in internal shells can be ejected from the atom, provided the photon's energy is at least as high as that shell's binding energy. The photoelectron is thus emitted, creating a vacancy that can be occupied by the transition of an electron on an external shell. This transition is accompanied by the emission of an X-ray.

A photon with a lower energy can only reach the external shells, producing an *edge*. An edge corresponds to the minimum photon energy necessary to eject an electron in a given shell. This threshold effect is characteristic to each atom.

The photoelectric interaction cross section of low energy photons for the K edge is given by

$$\sigma_{pe}^K = \frac{8}{3}\left[2\left(\frac{m_e c^2}{E_\gamma}\right)^7\right]^{1/2} 4\pi r_e^2 \alpha^4 Z^n \tag{2.2.4}$$

where n is a number that varies between 4 and 5. For $n = 5$, the photoelectric cross section displays a general dependence of

$$\sigma_{pe}^{K} \sim \frac{Z^5}{E_\gamma^{7/2}} \qquad (2.2.5)$$

For $E_\gamma \gg m_e c^2$ (so $E_\gamma / m_e c^2 \gg 1$),

$$\sigma_{pe}^{K} = \left(\frac{m_e c^2}{E_\gamma} \right) 4\pi r_e^2 \alpha^4 Z^5 \qquad (2.2.6)$$

showing the following dependence:

$$\sigma_{pe}^{K} \sim \frac{Z^5}{E_\gamma} \qquad (2.2.7)$$

2.2.2. Compton Scattering

Compton scattering dominates for photons with energies greater than a few hundred keV to a few MeV. The incident photon transfers a part of its energy to an atomic electron. The resulting products of the Compton interaction are a recoil electron and a scattered photon. In the laboratory reference frame, for an incident photon with an energy E_γ, the scattered photon has an energy E_γ',

$$E_\gamma' = h\frac{c}{\lambda'} = \frac{E_\gamma}{1 + \frac{E_\gamma}{m_e c^2}(1 - cos\theta)} \qquad (2.2.8)$$

The energy of the recoil electron is

$$E_R = E_\gamma - E_\gamma' = E_\gamma \frac{\frac{E_\gamma}{m_e c^2}(1 - cos\theta)}{1 + \frac{E_\gamma}{m_e c^2}(1 - cos\theta)} \qquad (2.2.9)$$

For a forward collision, $\theta = 0$, $E_\gamma' = E_\gamma$ and $E_R = 0$. For a backward collision, $\theta = \pi$ and,

$$E_\gamma' = \frac{E_\gamma}{1 + 2\frac{E_\gamma}{m_e c^2}} \qquad (2.2.10)$$

$$E_R = E_\gamma \frac{\frac{2E_\gamma}{m_e c^2}}{1 + \frac{2E_\gamma}{m_e c^2}} \qquad (2.2.11)$$

which corresponds to a Compton edge, the maximum energy that can be deposited by a photon, which results from a complete backscatter. Depending on θ, a continuous distribution of energies is created from the recoiling electrons, defining the Compton continuum. The Compton edge is thus the continuum energy's upper limit.

The interaction cross section as a function of the atomic number of the absorber and the energy of the photon is

$$\sigma_C = \sigma_s + \sigma_a \sim \frac{Z}{E_\gamma}, \qquad (2.2.12)$$

where σ_s and σ_a are the scattering and absorption cross sections, respectively.

2.2.3. Pair Production

If the photon energy is $E_\gamma \geq 2m_e c^2 = 1.022$ MeV, and approaches an atomic nucleus, the photon can be converted into an electron-positron pair. If an electron is also in the vicinity, triplet production can occur. The created positron is annihilated immediately with the nearby electron, which causes the emission of two photons with equal energies (0.511 MeV). Pair production is not possible in vacuum as the presence of a nucleus is required for momentum conservation.

The dependence of the pair production interaction cross section on the atomic number of the absorber and on the photon energy is

$$\sigma_{PP} \sim Z^2 \log E_\gamma. \qquad (2.2.13)$$

The photon energy is

$$E_\gamma^{min} = 2m_e c^2 \left(1 + \frac{2m_e c^2}{2Mc^2}\right) \qquad (2.2.14)$$

If the mass M of the target particle is much greater than m_e, for example if it is an atomic nucleus, this enables pair production to occur. If the target is an electron, $M = m_e$, and a triplet is produced. The kinetic energy available is

$$T = h\nu - 1{,}022\text{MeV} \tag{2.2.15}$$

for pair production ($2m_e c^2 = 1{,}022$ MeV). It is

$$T = h\nu - 2{,}044\text{MeV} \tag{2.2.16}$$

for triplet production ($4m_e c^2 = 2.044$ MeV).

2.2.4. Photon Attenuation and Total Absorption

When photons travel through matter, their numbers decrease exponentially with the distance. This gives

$$I\left(x\right) = I_0 e^{-\frac{\mu}{\rho}\rho x}, \tag{2.2.17}$$

where ρ is the density of the material through which the photon travels, x is the distance travelled and μ is the total absorption coefficient. This quantity is proportional to the inverse of the mean free path of photons in that material.

The total interaction probability of a photon in the material is the sum of all possible interactions: photoelectric, Compton, pair production, Rayleigh scattering and photonuclear interactions.[2] The total cross section, σ, multiplied by the density of atoms, N, gives the interaction probability per unit of length, with the total absorption coefficient, μ, given by

$$\mu = \sigma N = \sigma N_A \frac{\rho}{A}, \tag{2.2.18}$$

---

[2]In Rayleigh scattering, a photon is re-emitted with the same energy as the incident photon. Photonuclear interactions are important for higher energy photons and depend on the binding energy of nucleus. Neither of these interactions are relevant to the studies found in this work.

where A is the molar mass and $\sigma = \sigma_{pe} + \sigma_C + \sigma_{PP}$. Thus, the probability that a photon interacts with the material is given by

$$P = 1 - e^{-\frac{\mu}{\rho}\rho x}. \tag{2.2.19}$$

2.3. Neutrons

Neutrons interact with matter via elastic and inelastic scattering and nuclear reactions. These interactions allow for their detection. The likelihood of a neutron interacting in matter depends on the neutron's energy.

2.3.1. Thermal Neutrons

Thermal neutrons have an energy $E = kT$ ($k = 8.617 \times 10^{-5}$ eV K^{-1}, $T = 295$ K), i.e. $E = 25$ meV. They undergo certain nuclear reactions which cause the emission of charged particles which are used for their detection.

A practical application that is used by the ATLAS-TPX3 silicon pixel detectors operated in the ATLAS experiment is to cover a portion of the detector's chip with a layer of ^{6}LiF that acts as a thermal neutron converter [48]. The resulting nuclear reaction caused by the thermal neutrons on the ^{6}LiF is the following:

$$n + {}^6_3Li \rightarrow \alpha + {}^3_1H. \tag{2.3.1}$$

The interaction cross section of this reaction is 940 barns. The α-particles and the tritium emitted have energies of 2.73 MeV and 2.03 MeV respectively and can be detected in Si. The ranges of these particles varies considerably, with α-particles being stopped in $\sim 5\mu$m and tritium in $\sim 30\mu$m. This causes the tritium signal to be significantly greater than that produced by the α-particles in the ^{6}LiF converter region of the TPX3 mosaic.

2.3.2. Fast Neutrons

Fast neutrons are those whose kinetic energy is typically greater than 100 keV. These neutrons are detected thanks to nuclei that recoil from a converter. The recoil energy of a nucleus in an elastic collision with a fast neutron is

$$E_A = E_n \frac{4A}{(A+1)^2} \cos^2 \theta, \qquad (2.3.2)$$

where E_n is the energy of the incident neutron, A is the atomic mass of the nucleus and θ is the scattering angle in the laboratory reference frame. The maximum recoil energy of the nucleus is obtained for $\theta = 0$.

$$\frac{E_A}{E_n} = \frac{4A}{(A+1)^2}. \qquad (2.3.3)$$

This relation makes evident the fact that those materials possessing small atomic numbers are more favourable for the detection of fast neutrons. Consequently, polyethylene (C_2H_4) is used for this purpose.

The mosaic of neutron converters used on the ATLAS-TPX3 detectors in the ATLAS experiment is shown in Figure 2.3.1.
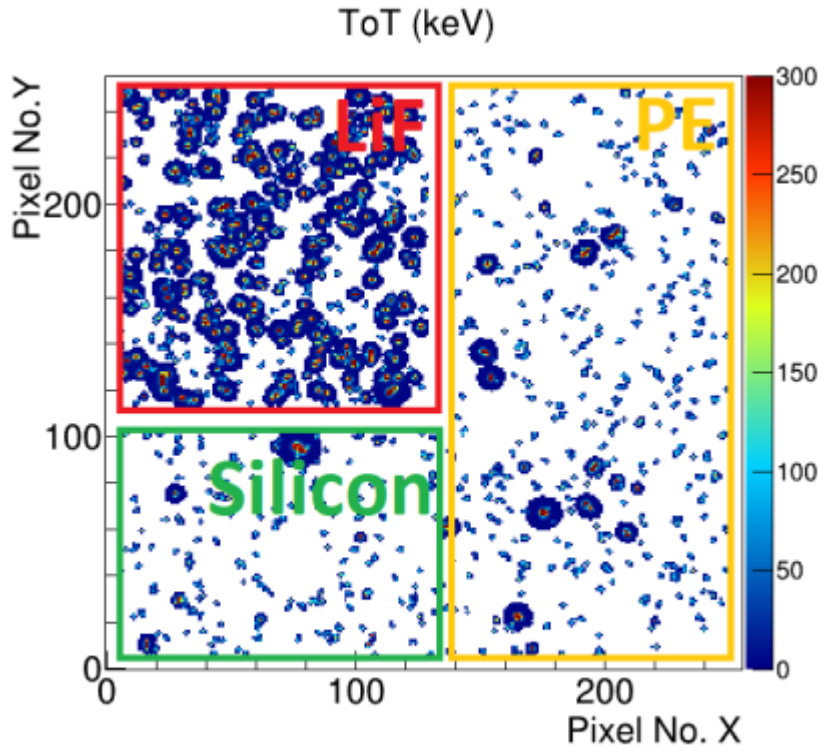
Fig. 2.3.1. An integrated frame of events in a Timepix3 detector (ATLAS-TPX3) covered by a mosaic of LiF (5 mg/cm^2) and Polyethylene (PE) (of 1.3 mm) neutron converters with an uncovered region of Si. Energy is expressed in terms of keV and labelled as ToT. [48]

Chapter 3

Temperature Stability

3.1. Context

Modern particle detectors are expected to withstand a variety of radiation environments and be functional for extended periods of sustained operation. The high amount of electronics equipping most modern semiconductor detectors also presents additional challenges with regards to radiation hardness and noise and requires one to evaluate the effect that this has on detection efficiencies. In pixel detectors like TPX3, these challenges are compounded by the existence of multiple pixels and their independent electronics circuits [49]. Such a detector is expected to be operational in both vacuum and in air, and should be able to tolerate the temperature changes that are characteristic of each of these environments.

In the vacuum environment, cooling systems are used for a host of reasons. Primarily, they prevent the detector from overheating and malfunctioning due to physical or structural damage caused to the chipboard. They also limit electronic noise and provide a clearer signal. Finally, in spectroscopic applications, cooling systems are able to ensure that the detector is maintained at an operational temperature close to that which was used during the energy calibration, an exercise which, many times, is performed in air environments, and therefore, at or a few degrees above room temperature.

Having a cooling system is, of course, an ideal scenario but may not always be practical. Occasionally, an experimental setup cannot accommodate the installation of such a system.

In this case, it is important to evaluate the tolerance of the detector to high amounts of heat and continuous operation. This tolerance is characterized by the device's ability to detect particles. It can be evaluated by investigating how well the detector maintains its detection efficiency and particle energy reconstruction capability in these elevated temperature contexts, in contrast to the control temperature range[1]. Alternatively, if its detection capabilities degrade in the high temperature environment, it is of interest to assess by how much and to determine whether this is a prohibitive environment for the detector's use.

Outside of the vacuum environment, detectors placed in air are also subject to temperature fluctuations, depending on the degree to which their sensor temperatures can be maintained through cooling systems. In these cases, and in the absence of cooling systems, hardware and cabling are the main conduits through which heat is exchanged with the surrounding environment.

For the ATLAS-TPX3 network of detectors, the surroundings can vary. Of the two detector units, one is installed in the ATLAS Central Barrel, densely surrounded by cabling and other supporting steel structures, encased in its own steel holder. The second detector unit was installed on the wall on Side A, again within a steel casing, but without much surrounding material save for the wall on which it was mounted and its own connected cables [**3**]. The two installed units are shown in Figure 3.1.1 along with their locations in ATLAS. In neither case was a cooling system implemented to regulate sensor temperature.

3.2. Vacuum measurements and heating

For many characterization tests of TPX3 at UdeM, it is necessary for nuclear particle beams to be measured. These beams are produced at the Tandem VdG accelerator. However, the beam energies are too low to be able to operate the detector in air due to the total absorption of these heavy particles in the steel walls containing the vacuum. The maximum energy available for a given particle that can be produced at the Tandem VdG is not high enough to produce a range that would surpass the thickness of the vacuum chamber walls.

---

[1]The control temperature range is considered to be roughly 20°-30°, as this is the typical temperature range in which energy calibrations are performed
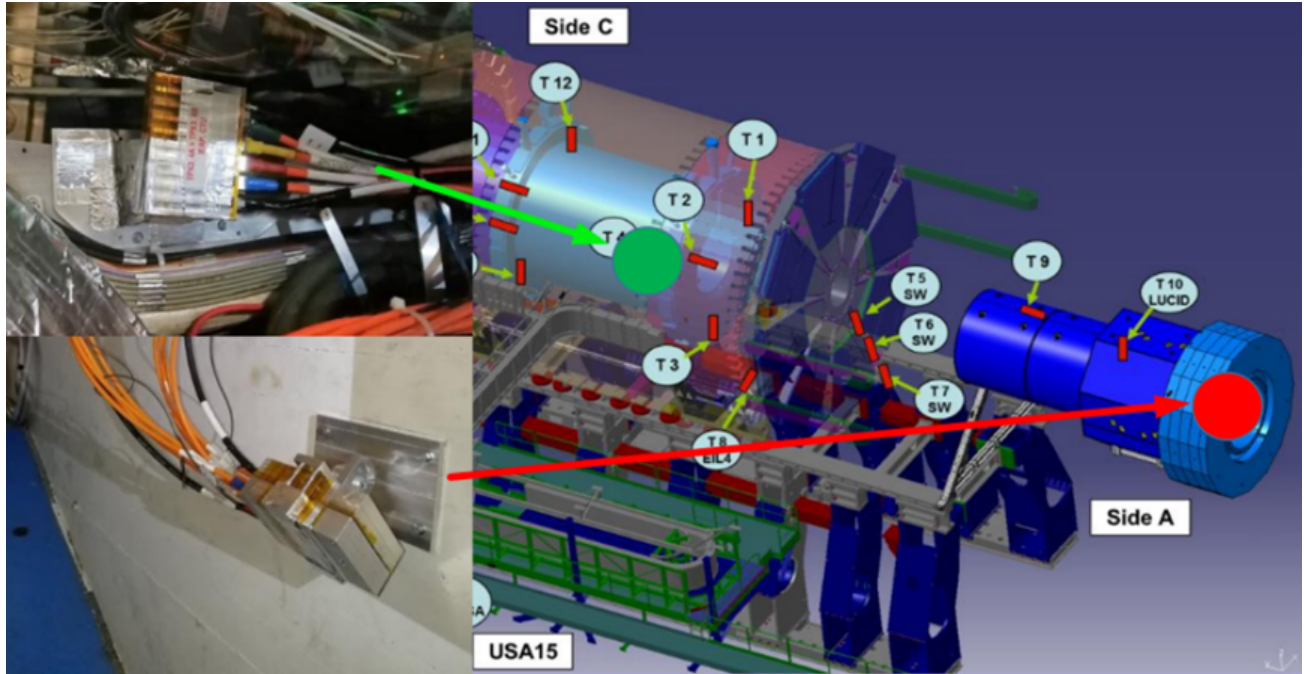
Fig. 3.1.1. Locations of two TPX3-Si devices installed in the ATLAS cavern in 2018.[**3**]

This makes in vacuum measurements necessary for any kind of thorough characterization and clustering studies.

The Katherine readout interface [**50**] is unfortunately unable to operate in vacuum for extended periods as it is subject to overheating. This required a retrofitting of the existing vacuum setup to properly accommodate this interface and the redesign of multiple hardware components. The details of this exercise are described in the publication that follows.

The heating technique used in this study utilizes light exposure onto the back of the support mount on which the TPX3 was placed. The retrofitted vacuum chamber can accommodate the installation of a 2 cm diameter portal which is positioned normal to the oncoming scattered beam and installed on a flange nipple. Even though the aperture through which light passes is small and only directly hits the back of the support mount, it is expected that some light can reach the front of the sensor through reflections on the curved chamber walls, originating from scattered light coming from the space between the nipple and the support. Any direct exposure of the Si to light must be avoided to prevent damaging the detector. For this reason, a tube of aluminum foil was fashioned and inserted into the flange nipple in the vacuum chamber, extending the corridor through which light passed toward

65

the support, without directly touching it. This refocused the light over the additional length to the support and reduced the ambient light present in the rest of the chamber.

3.3. Cluster Size

In the course of evaluating its temperature response, the detector's ability to dependably measure important quantities is tested. Other than the deposited energy, the cluster size of particles is measured. This cluster size is defined as the number of pixels that have been activated for a given particle event. For a sample of beam particles of a single type, angle of incidence, and energy, the cluster sizes of individual particles are centred around some mean value. It is this mean value which is usually cited as the cluster size of that particle type, at that angle, and at that energy. Although an individual particle's cluster size, by definition, is a whole number, the mean value cluster size of the collective is often not.

The main reason for the use of a non-integer mean value to represent a quantity which inherently describes discreet pixels is one of practicality. Cluster size is used for the purposes of particle identification and is helpful in making energy discriminations. Because it is known that cluster size depends on the deposited energy, even slight changes in energy are expected to result in slight changes in the cluster size, even if those changes are smaller than the size of an actual pixel. Therefore, the non-integer mean value communicates some of that information.

3.4. Publication: Temperature effects on clustering in TPX3-Si pixel detectors

My contributions to this publication are:

- Experimental design;
- Detector calibration;
- Collection of data;
- Analysis of data;

- Authorship of article.

Temperature effects on clustering in TPX3-Si pixel detectors

C. Leroy, C. Papadatos, M. Usman, M. Boussa*

Groupe de physique des particules, Université de Montreal

---
*Corresponding author

3.4.1. Abstract

The performance of a Timepix3 (TPX3) detector equipped with a 500 μm thick silicon sensor was evaluated while in vacuum and subjected to temperature variations. Proton beam measurements were performed at the Tandem Van de Graaff accelerator of the University of Montreal to determine the effect of sensor temperature on cluster parameters as well as measured energy. It was observed that temperature had a negative effect on the reconstructed energy obtained from the conventional calibration technique. The sizes of registered proton clusters increased as the sensor was heated up, indicating greater charge drift, resulting in additional charge sharing between neighbouring pixels.

3.4.2. Introduction

The growing interest in the usage of pixelated radiation detectors in space requires greater research into the functionality of these devices in that harsh environment for both crewed missions [8] and satellites [9, 11, 17, 12]. Low atmospheric pressures found around satellites in low earth orbit (approx. 10^{-10} to 10^{-8} Torr)[10], as well as dramatic temperature variations due to incident light radiation and limited thermal dissipation pose significant technical challenges for practical use of these instruments. The behaviour of these detectors when subjected to such extremes determines how well quantities such as ionizing radiation dose and energy can be measured, with x-ray energy reconstruction deteriorating as temperatures are increased[18, 15].

In order to sustain a long term measurement with the TPX3 device[2] connected to a Katherine readout interface[50], upgrades to the existing vacuum setup used at the Tandem Van de Graaff (VdG) facility at the University of Montreal (UdeM) were completed and used for this study. Before the upgrade, the temperature at which sustained beam measurements were made remained constant during operation of the device in the vacuum, at approximately 95°C. This elevated temperature can affect cluster size and energy by increasing the bias required for full depletion[14]. The applied bias is a parameter known to affect these quantities, with a lower bias weakening the electric field strength, and therefore, increasing

the radial extension of the charge carrier drift, resulting in clusters that are larger than those observed when the applied bias is much greater than that required for full depletion [27].

For protons at normal incidence to the detector, in addition to the bias effect, the cluster size is affected by the particle's deposited charge in the sensor, such that higher proton energies yield larger clusters [51]. An investigation into the effects of temperature on clustering thus requires one to observe these effects independent of energy by measuring them for multiple proton energies.

3.4.3. Materials and methods

3.4.3.1. Vacuum setup. All measurements were performed using a TPX3 device with a silicon sensor of 500 μm thickness. The sensor is divided into a matrix of 256 x 256 square pixels with a 55 μm pitch. Likewise, all TPX3 sensor temperature measurements were done using the temperature sensor in the ASIC. All readout temperature measurements were taken using Katherine's built-in temperature sensor[50].

The vacuum chamber housing the TPX3 has an internal diameter and height of 15 cm and 30 cm, respectively, and is integrated with the main beam line of the Tandem VdG accelerator at UdeM. Accelerated protons travel through the main line until they are deflected by a gold foil (0.12 μm thick) in the scattering chamber. The protons scatter at 90° with respect to the beam and continue their passage into the TPX3 chamber, where they are measured by the detector. All proton measurements are carried out in vacuum at 4×10^{-7} Torr.

Since the presently used Katherine readout requires two separate connections for communicating with the readout software and for its power, a new feed-through was designed. Katherine connects to a PC by Ethernet cable for communication with the readout acquisition software. It is powered using an AC/DC adapter. Therefore, a flange with two feed-throughs for each connection was made and installed at one of the chamber's available valves. This meant taking measurements with both TPX3 and Katherine together in vacuum. Although this setup was functional for measuring beams, it could only be done over
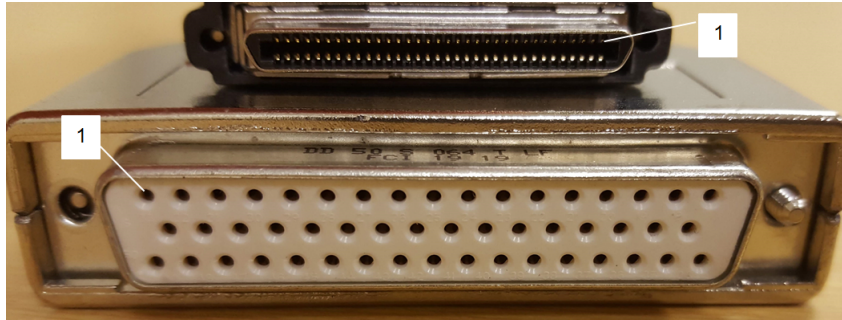
Fig. 3.4.1. D-sub 50 pin and VHDCI connectors used in the TANDEM TPX3-Si setup.

very short periods (shorter than 10 minutes) before the readout overheated in the vacuum. This setup will be referred to henceforth as the "old setup".

The solution to the overheating was for the readout to be left in air during the measurement, while the TPX3 was installed inside the vacuum. This required reconfiguring the existing equipment to accommodate the new feed-through and flange that needed installation. The new flange consists of a male-male 50-pin D-Sub feed-through, to which converter cables are connected, having on one side, 50-pin D-Sub female connecting ports, and on the other side, either male or female 68-pin VHDCI[2] ports (see Figure 3.4.1)[3]. This will be referred to as the "new setup".

The temperature stabilities of the sensor and readout were evaluated through the measurements of proton beams from 3 to 9 MeV for each setup, in 1 MeV steps, to observe the impact that changing the readout environment has on the reconstructed energy. Due to the expectation of charge saturation and the reduced applicability of the per pixel calibration at high per pixel energies ($\geq$ 900 keV/pixel)[16], an effort was made to minimize this by performing the energy measurements, first at normal incidence — where clusters would be subject to greater saturation in their central pixels — and again at high incidence (75°) — where charges would spread over a greater number of pixels, thereby reducing the amount of charge that is concentrated in any individual central pixel. Each energy measurement lasted 1 minute at 0° incidence and 5 minutes at 75° incidence.

---

[2]Very High Density Cable Interconnect.
[3]Initially designed and used at the VdG accelerator of the Institute of Experimental and Applied Physics (IEAP) in Prague[52]

3.4.3.2. Heating technique. To measure the effect of temperature variations on the detector behaviour, the TPX3 device was placed in vacuum during two proton measurements of different energies, once again motivated by the need to validate any temperature effects across more than one energy. The Katherine readout was left outside, in air, as in the previously described new setup.

Several proton measurements of 5 MeV and 7 MeV were done, each at normal incidence and at a constant operational bias of 230 V, guaranteeing full depletion over the 500 μm of Si. Two energies, 5 and 7 MeV were chosen in order to probe deeply into the centre region of the sensor (ranges between 215-385 μm), while minimizing charge losses in the dead layers of Al (1.2μm) and Si (2 μm) on the surface of the sensor. These losses would be greater at lower energies and would prohibit a deep probe at high angles of incidence (i.e. 75°). Choosing multiple energies allows one to observe any effect that charge saturation might have for the higher energy series (7 MeV).

The constant bias was maintained by the Katherine readout, which in turn was powered with the plug-in adapter. The TPX3 was heated using an external lamp shining white light emitted by an incandescent bulb into the vacuum chamber, through a portal, onto a 1.5 mm thick steel backplate on which was mounted the TPX3. This was done in order to increase the sensor temperature through thermal conduction across the thickness of the backplate, as well as to prevent direct sensor exposure to the light, thus protecting it from excessive damaging heating.

For the 7 MeV series of measurements, the exposure of the lamp into the portal was maintained, uninterrupted, throughout the entire series of measurements, with each measurement lasting 60 seconds. For the 5 MeV measurement series, a different approach was taken. This time, the lamp exposure measurement lasted 60 seconds. while the total light exposure exceeded that due to the time required to enter or exit the experimental area to manually turn the light on or off between measurements. After an exposure period elapsed, the vacuum chamber's portal was covered to cut off the illumination from the lamp and another measurement was taken for 40 seconds (after the same transit time between the beam

and monitoring rooms). A total of 20 temperature measurements were taken over 40 minutes. In the final 10 minutes, a sustained illumination was applied while several consecutive measurements were taken. The purpose of the stepwise technique was to observe cooling that took place during temporary periods of non-exposure to the light. Any cooling which would occur would be from heat diffusion through the cabling and the backplate. This allowed for the measurement of energies and cluster sizes after larger temperature drops — something that would be less likely to occur if the light exposure was consistently maintained.

To confirm the periodic cooling observed during the intermittent heating technique, a thermistor was connected to the exposed backplate in a subsequent measurement where temperature readings were taken at 60 second alternating intervals of light exposure and darkness. The readings were taken at the end of each interval, either after the 60 s heating period, or the 60 s cooling period. After the backplate was allowed to cool back down to the baseline temperature (~ 84°C), the backplate then underwent a constant exposure to the light so as to recreate the constant heating technique. The results of this exercise are shown in Figure 3.4.2. The constant heating technique eventually leads to a levelling off of the temperature near 102°C due to stabilization caused by heat diffusing away from the backplate (through the backplate support stem as well as through the TPX3 connector and cable assembly).

It must be mentioned that these heating methods are implicitly restricted by certain experimental limitations. One constraint is on the lower available temperature bound once a measurement is started. The nature of the experimental setup is such that the sensor must be fed by the DC power supply, via the Katherine readout, for a minimum of 45 seconds before initiating the acquisition software to begin the measurement. This period corresponds to the amount of time required for the connection to be established between the readout device and the software. Furthermore, in order to verify the quality of the proton beam created at the Tandem VdG accelerator, one must make several 20-30 s monitoring acquisitions with the TPX3-Si, over a period of roughly 10-15 minutes. During this time, the sensor's temperature is constantly increasing, as measured by a temperature sensor in the ASIC. By the time the
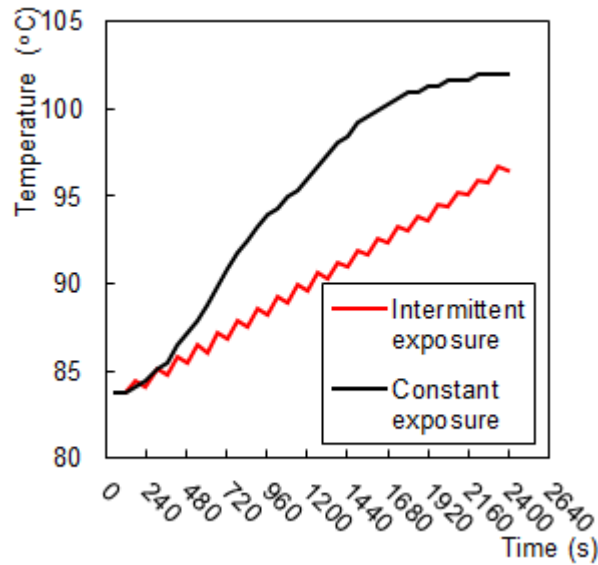
Fig. 3.4.2. Temperature measurements taken using a thermistor connected to the backplate. The intermittent heating technique features periods of cooling on the order of 0.5-0.7°C after the light has been removed for 60 seconds.

first proton beam is measured, the sensor has already reached roughly 84°C. The feasibility of installing a cooling system in the vacuum chamber was investigated, but due to space limitations, was deemed impossible under either the old or new setup.

3.4.4. Results

The results of the setup changes can be seen in Figures 3.4.3a and 3.4.3b. Here, the significant reduction in temperature is observed in both the TPX3's silicon sensor and readout. These readings were taken over the course of proton beam measurements for energies going from 3 MeV to 9 MeV. Using the old setup, the average temperatures across all measurements for the sensor and the readout were (123.3 ± 0.7)°C and (97 ± 1)°C, respectively. After the installation of the new setup, where the Katherine readout was left outside, in air, the temperatures decreased to (97.6 ± 0.3)°C and (46.41 ± 0.06)°C on average for the sensor and readout, respectively.

The energy resolutions expressed as the percent of the full width at half maximum (FWHM) of the measured energy distributions for each series of measurements can be seen in Figures 3.4.4a and 3.4.4b. These figures show the full energy series before (%Res old)
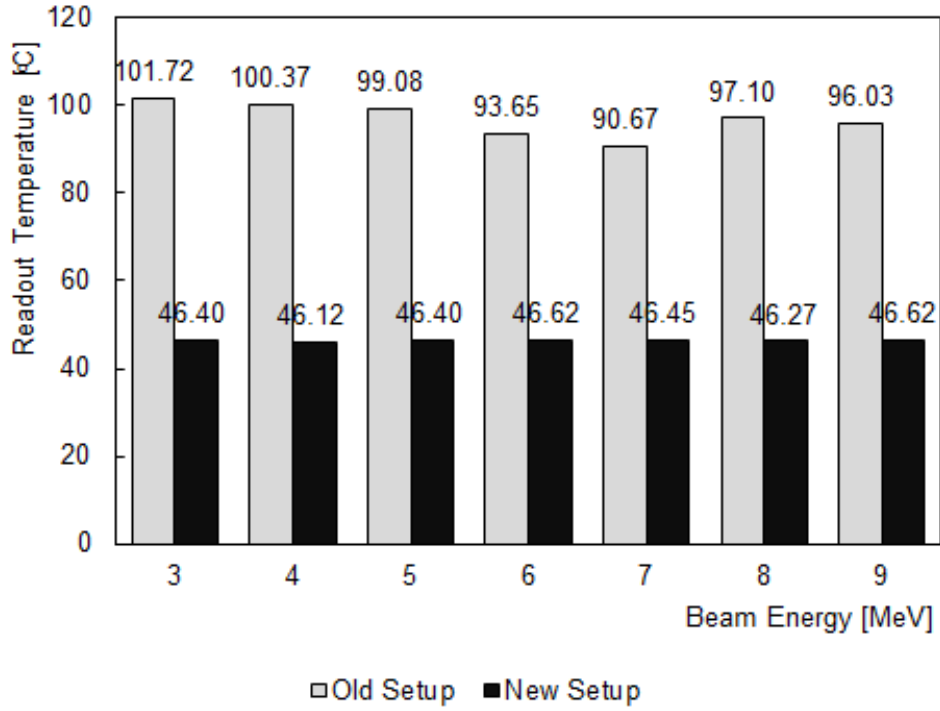
(a)
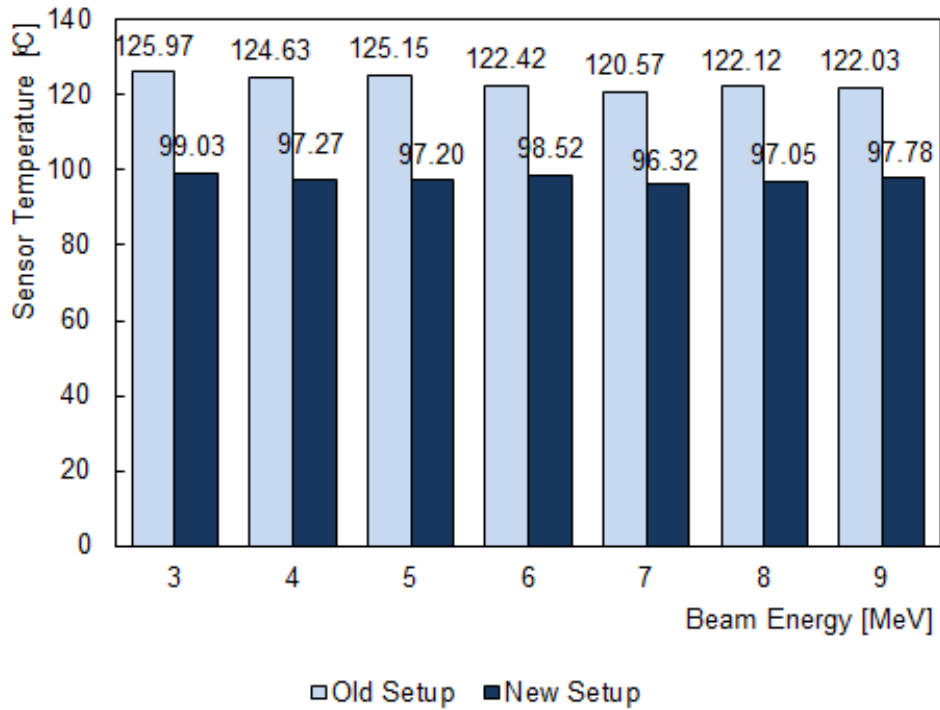
(b)

Fig. 3.4.3. The measured temperatures for the old (Katherine in vacuum) and new (Katherine in air) setups are compared for (a) the readout and (b) the sensor.
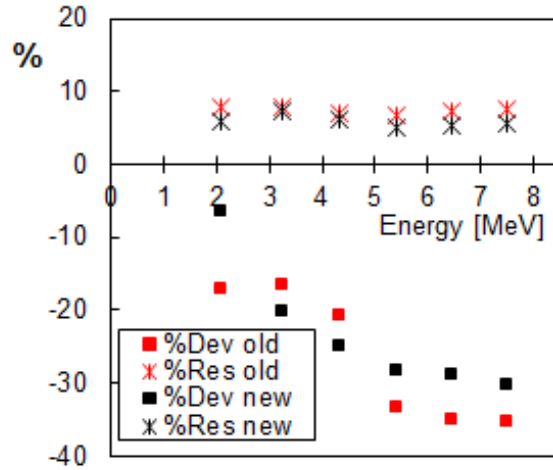
(a) 75°.
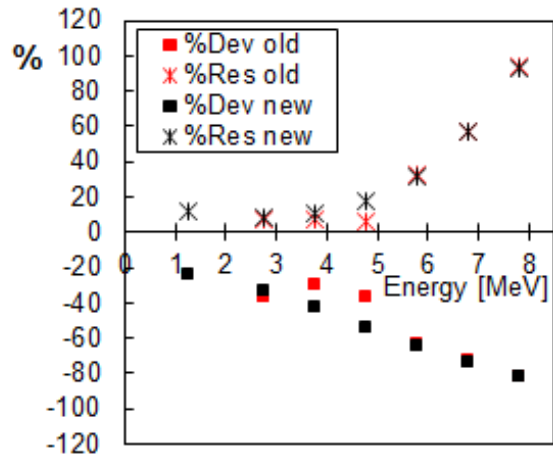
(b) 0°.

Fig. 3.4.4. Comparison of the calibration's performance under the in-vacuum readout setup (old) and the in-air readout setup (new) for proton measurements at several energies across two parameters: 1) measured energy resolutions (%Res) represented by the FWHM of the energy distributions, expressed as a percentage of the measured energy and 2) percent deviations (%Dev) between the measured and expected energies. Measurements were done at 75° and normal incidence, (a) 75° and (b) 0°. Greater charge saturation can be seen at high energies and at normal incidence, as indicated by the higher percent deviations in those cases.

and after (%Res new) the setup modification took place at the two evaluated angles of incidence. These figures also show the percent deviation in the energy measured compared to the expected energy for each measurement series.

The temperature of the sensor over the course of the measurement series for both the 5 MeV and 7 MeV measurements is shown in Figures 3.4.5a and 3.4.5b. The duration of each

measurement is indicated by the horizontal error bars, while in 3.4.5a, the periods of light exposure are highlighted in yellow. All points in Figure 3.4.5b are measurements during constant light exposure. The two cluster parameters which were investigated were cluster size and measured cluster energy. These are shown in Figures 3.4.6a, 3.4.6b, 3.4.7a, and 3.4.7b. The error bars in these cases correspond to the error on the mean of the gaussian fit applied to the cluster size and measured energy distributions. The keV energies have been reconstructed using the conventional TPX per-pixel calibration [16], at sensor temperatures between 60-70°C with the readout temperature near 45°C. The calibration was not corrected to compensate for temperature effects as this was the subject under investigation.

Linear fits applied to the cluster size (CS) measurement series yield CS= $(0.281 \pm 0.010)T + (105.39 \pm 0.95)$ with $R^2 = 0.98$ for 5 MeV and CS= $(0.235 \pm 0.014)T + (89.6 \pm 1.3)$ with $R^2 = 0.92$ for 7 MeV (Figure 3.4.6a, 3.4.6b), where T represents the temperature in degrees Celsius. Fits to the measured energy series give E (keV)= $(-6.70 \pm 0.41)T + (2887 \pm 39)$ with $R^2 = 0.94$ for 5 MeV and E (keV)= $(-6.85 \pm 0.72)T + (2396 \pm 70)$ with $R^2 = 0.77$ for 7 MeV (Figure 3.4.7a, 3.4.7b). The low R^2 in 3.4.7b can be attributed to the increased charge saturation present at 7 MeV since only the measured energy fit was of such low quality. This is addressed in greater detail in the Discussion section.

3.4.5. Discussion

3.4.5.1. Detector performance in vacuum. In the old setup, both the sensor and the readout parts were installed inside the vacuum chamber, leading to poor thermal dissipation away from both parts. Placing the heat generating readout in air was enough to reduce the sensor temperature by approximately 26°C, on average, as seen in Figure 3.4.3b.

In terms of detector performance, the differences in measured energy were small, with resolutions improving by 1.6% on average across all 75° energy measurements, where saturation effects are diminished compared with 0° incidence. This was coupled with an overall decrease in the percent deviation from the expected energy, demonstrating the improvement of the calibration's quality at lower temperatures (closer to the 60-70°C sensor temperature
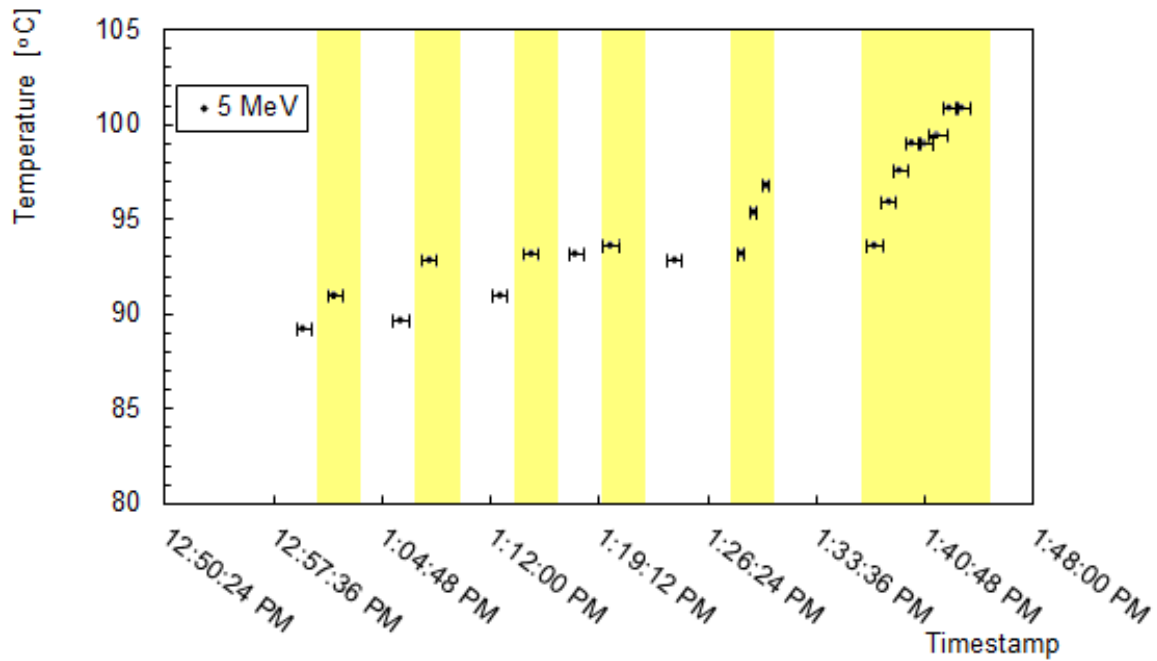
(a) 5 MeV.
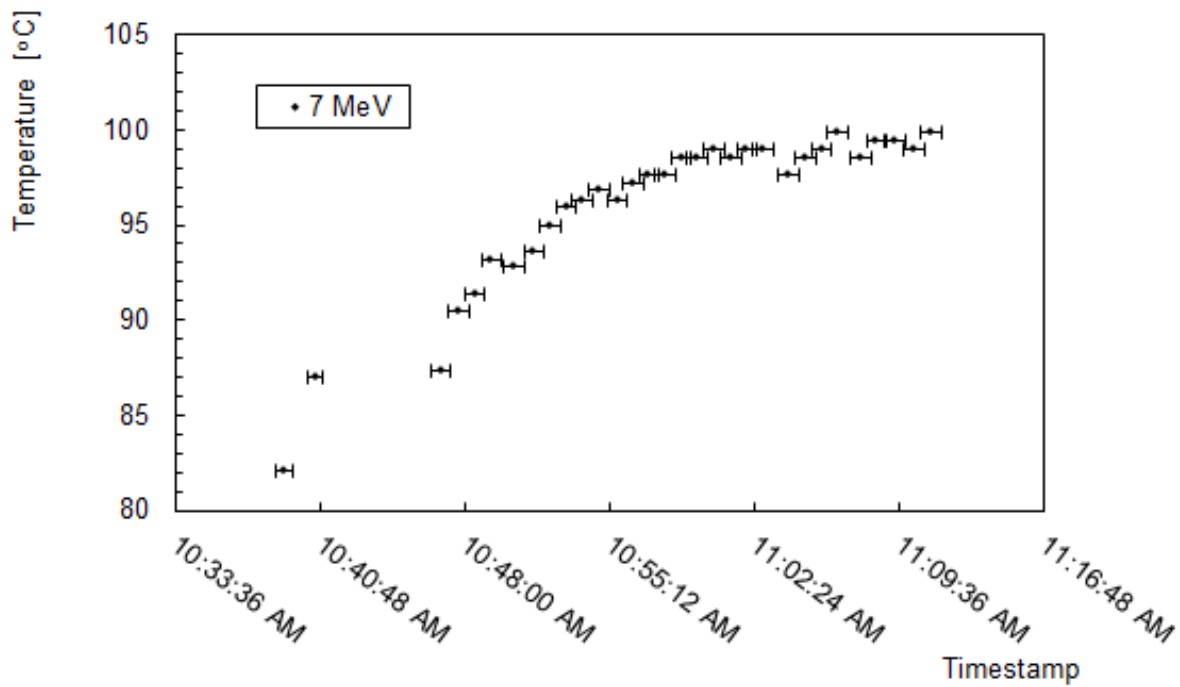
(b) 7 MeV.

Fig. 3.4.5. Sensor temperature as a function of time. In (a), the temperature was increased in stages through incremental exposure to the lamp for 5 MeV proton measurements. Yellow regions indicate periods of exposure. Error bars indicate the measurement duration. In (b), the lamp exposure was kept constant throughout the 7 MeV proton measurement series. The incremental exposure in (a) results in larger temperature drops compared to those in (b).
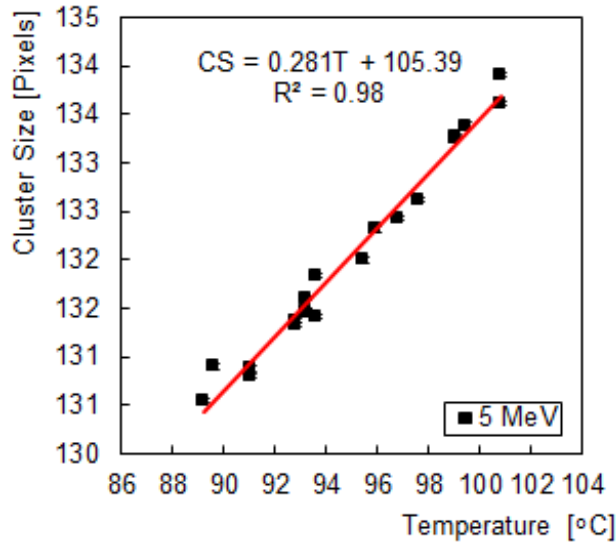
(a) 5 MeV.
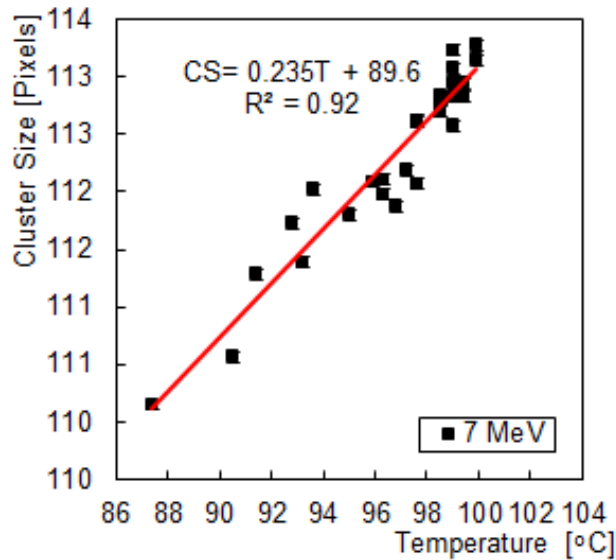
(b) 7 MeV.

Fig. 3.4.6. Cluster size of (a) 5 MeV and (b) 7 MeV protons as a function of the sensor temperature. The red lines correspond to fits to the data. Plots in (a) and (b) are from the application of the stepwise and constant temperature increase procedures, respectively.

in air, at which the calibration was done), as also seen in [**18**], albeit using x-rays instead of protons. It is more difficult to draw any such conclusion for measurements taken at 0° incidence, due to the stronger effect of charge saturation and deviation from the linearity of the energy calibration compared to the effect of reduced temperature. Figures 3.4.4a and 3.4.4b reflect these observations. These results, however, were not observed for two energy points (4 MeV, 5 MeV). It is possible that these proton energies produce cluster heights
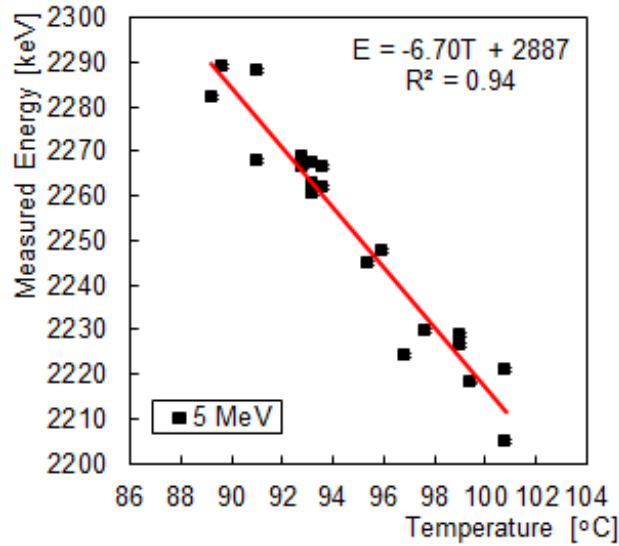
(a) 5 MeV.
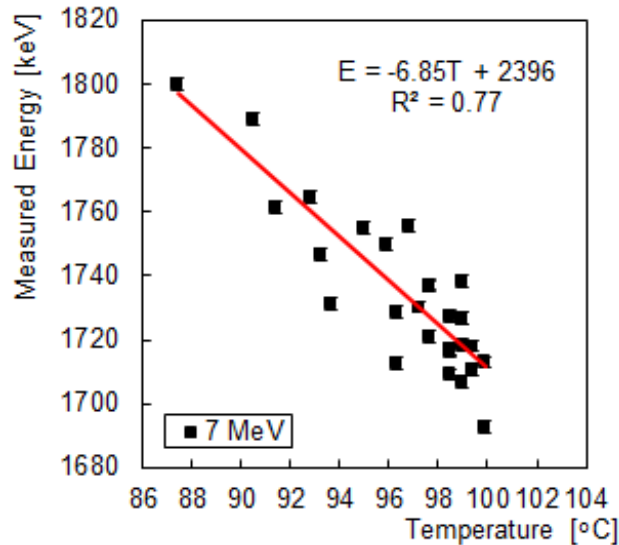
(b) 7 MeV.

Fig. 3.4.7. Measured per-cluster energies of (a) 5 MeV and (b) 7 MeV protons as a function of the sensor temperature. The red lines correspond to fits to the data. (a) and (b) are from the application of the stepwise and constant temperature increase procedures, respectively. Comparing with the slopes found in 3.4.6a and 3.4.6b, one observes an opposite behaviour between energy and cluster size.

(maximum per-pixel energy value for a given cluster) which straddle the approximate 900 keV threshold in the calibration curve between linear energy reconstruction and non-linearity [16]. As a comparison, for 4 MeV and 5 MeV in the old setup, the measured cluster heights are 388 keV/pixel and 406 keV/pixel, respectively, indicating a large degree of charge loss

in those pixels. Equivalent measured cluster height values are obtained in the new setup's measurements at 391 keV and 410 keV for 4 MeV and 5 MeV respectively.

3.4.5.2. Temperature variation and clustering. The first feature which is observed in Figures 3.4.5a and 3.4.5b is how the sensor already starts at an elevated initial temperature value with respect to the 60-70°C observed during the calibration, and during normal operation in air. This can be attributed to sensor warming in the vacuum during the initial setup of the first proton measurement at 5 MeV. As described earlier, there is a significant wait time between connecting the detector and the actual data taking. During this time — from the moment the sensor is connected to the power supply, through the initial beam monitoring, and finally up to the moment the temperature measurements begin — the sensor has already undergone an increase in temperature within the vacuum, up to about 84°C. Therefore, that value must be expected as the lower bound. The upper bound is expected at around 100°C, as shown in both figures. This is due to the eventual cooling resulting from the TPX3's contact with the steel backplate as well as through the cabling, which helps conduct heat away from the sensor.

Another observation is how the behaviour of the temperature change depends on the method of heating. In the 5 MeV case, the heating was performed in steps. Figure 3.4.5a shows how the temperature increases relatively slowly in a stepwise fashion and in correspondence with the light exposure and heating periods. As can be seen in the plot, the final two heating periods were subdivided into a series of multiple smaller measurements to track the sensor temperature during the exposures, with three 20 second measurements, followed by a longer cooling period, and the final long exposure. Generally speaking, with each jump, there comes a cool off. Overall, the behaviour of the temperature here follows sequential jumps to higher highs, followed by drops to higher lows. These drops indicate the periods after the light source was removed, and cooling of the sensor could take place by heat diffusion through materials which were in constant contact with it. Comparatively, the increase in the 7 MeV series is much smoother. This is an indication of the accumulation of heat through constant exposure to the light source. Where the temperature levels off,

as it approaches 100°C, an equilibrium is reached between inflow of heat due to the light source and outflow of heat due to diffusion through the chipboard and the steel backplate of the TPX3 holder (this point of stability is also observed in the independent temperature measurement shown in Figure 3.4.2).

The linear fits applied in, 3.4.6a, 3.4.6b 3.4.7a, and 3.4.7b yield different results for measured cluster sizes and energies. Cluster size is shown to increase consistently regardless of particle energy, as temperature increases. Conversely, the reconstructed energy is shown to do the opposite, again regardless of the incident proton energy. One notable feature between the 5 MeV and 7 MeV plots is how much lower the quality of the fits are for the 7 MeV functions compared to the 5 MeV fits. This can be explained by the presence of charge saturation having a greater effect for this higher deposited proton energy, leading to more instability in the measured proton energy. Under the current calibration scheme, which assumes linearity between energy and the time-over-threshold parameter except at low energies (≥ 5 keV), individual pixels enter into a non-linear regime above approximately 900 keV/pixel in deposited energy. Above this energy, the linearity becomes increasingly tenuous, resulting in underestimations in the measured energies for these highly charged pixels. This is one consequence of the inability of performing a per-pixel calibration with x-rays having energies greater than roughly 100 keV, as such x-rays generate few single pixel hits due to charge sharing among neighbouring pixels. In the case of the 5 MeV protons measured during the heating procedure, the most charged pixel in each cluster recorded an energy of only 382 keV/pixel on average after the calibration was applied. For 7 MeV, the most charged pixel in each cluster measured 429 keV/pixel on average. The greater amount of saturation is also indicated by the overall lower measured energy of the cluster at 7 MeV compared to 5 MeV. This would especially explain why the R^2 of the 7 MeV energy fit is so much lower than that of 5 MeV. The use of a different heating technique is unlikely to be the cause of the poor quality of this fit since the fit applied to the cluster size of the same measurement series did not yield an equivalently low R^2, indicating that the cause is limited

to energy reconstruction factors associated with the divergence between the reconstructed energy from the calibration curve and the true deposited energy.

Regardless of the heating technique used and proton energy, the general trends of measured energy decreasing with increasing temperature and cluster size increasing as a result of increasing temperature remain consistent.

Of note is the behaviour of the cluster size with respect to the energy as temperature is increased. It is typically expected that cluster size is strongly determined by the particle's energy and type (ion, electron or photon)[51]. In the present study, however, only protons are used. Therefore, as energy increases, so does the cluster size. In contradiction to this, Figures 3.4.6a, 3.4.6b, 3.4.7a, and 3.4.7b demonstrate an inverse relationship between energy and cluster size. In this case, despite the fact that energy is recorded as decreasing with increasing temperatures, cluster size undergoes an increase. This suggests that the temperature effect is especially pronounced given that it can overcome the typical energy-cluster size relationship.

One parameter which would cause this inverse relationship is the applied bias [27]. For a 500 μm sensor, above 90 V, increasing the bias increases the electric field strength across the sensor, which accelerates the carriers to the electrodes to a greater extent, thereby limiting their lateral drift and resulting in smaller cluster sizes. Meanwhile, more energy is collected due to increasing the active layer of the sensor, resulting in more pair production. The opposite is also the case: decreasing the bias results in less collected charge, but larger clusters, as observed in this study. An increase in temperature under constant applied external bias, therefore, has the same effect as a reduction in the bias at constant temperature, implying a reduction in the internal field strength such that the detector is operating at a lower effective bias than that which was actually applied.

While a conventional controlled scan would run from high to low temperatures to ensure stability, this procedure was not adopted for this study. However, although the general tendency here was to increase the temperature, this was done through light exposures, as described. The average temperature for each measurement period was measured by the TPX3, and the corresponding energy and cluster size measured during the same period generated

the plots in Figures 3.4.6a, 3.4.6b, 3.4.7a, and 3.4.7b. There are indeed a number of periods, especially during the 5 MeV runs, when the temperature drops from one measurement period to the next due to temporary cooling (see white regions in Figure 3.4.5a). Nonetheless, the energies and cluster sizes measured at those temperatures remain coherent with those measured when that same temperature is achieved after a temperature increase. This is also evidenced by the linearity seen in the mentioned plots.

Leakage current is expected to rise with increased temperature. In TPX3 devices, this can be compensated through the Krummenacher architecture[49] of the preamplifier for currents up to 10 nA per pixel. Further targeted studies should be pursued to investigate the thresholds of this compensation for higher temperatures and to determine how this is related to cluster size, in particular.

3.4.6. Conclusion

The feasibility of using TPX3 devices at high temperatures and in low pressure environments has been tested within the available technical limitations. It was observed that higher temperatures result in a deterioration of the calibration's quality, leading to lower measured energies, as expected. However, a better understanding of the role that sensor temperature plays in clustering is required. It was found that increasing the sensor temperature also increases the degree of charge sharing, as evidenced by larger proton clusters, indicating a decrease in the electric field strength across the sensor. Future investigations should be carried out over a wider temperature range, such as with the use of a cooling system in a redesigned vacuum chamber setup to access temperatures lower than 84°C. Similarly, isolated studies of the leakage current should be done.

Acknowledgments

Chapter 4

Clustering

4.1. Context

Given the noticeable effect that temperature is observed to have on the size of proton clusters, independent of the proton's energy, it was necessary to study clustering in a more general and complete way. Cluster size is an important parameter when performing particle identification. The size of a cluster carries with it information on the energy of a particle, its trajectory, and, as shown in the previous publication, the sensor's temperature[55, 20].

In addition to these physical parameters, applied bias and particle mass also exert an influence on the number of pixels that are activated for a single particle event. This makes cluster size a complex and multifaceted variable that depends on several physical quantities, the better understanding of which would benefit particle identification efforts in the ATLAS-TPX3 program.

4.2. Cluster Types used in the ATLAS-TPX3 Collaboration

Over the history of the Medipix and Timepix devices, a host of analytical techniques have been developed to study the behaviour of clusters that can be observed, depending on the variety of particles that are incident on a pixelated sensor during beam runs at the LHC.

Dots		Photons and electrons
Small blobs		Photons and electrons
Heavy blobs		Heavy ionizing particles
Heavy tracks		Heavy ionizing particles → Incidence is not perpendicular to the detector's surface (Bragg curve)
Straight tracks		MIP
Curly tracks		Energetic electrons

Fig. 4.2.1. An assortment of cluster types based on the number of activated pixels and the geometric properties of the pixel group.[**53**]

A conventional lexicon was created which classified clusters according to their various shapes and sizes giving each category a name.

Clusters made up of one or two neighbouring pixels are designated as dots, and frequently will be qualified as single or double hits respectively. Once a cluster has three pixels or more, it can either be what is called a "blob", where its pixels surround a common geometric centre, more or less symmetrically, or it can be called a "track". There are then three types of tracks: heavy tracks, which are essentially blobs that are spread linearly across the length of several more pixels in one direction, curly tracks, which are groups of adjoining pixels that follow random (often curly) paths across several pixels, and lastly, straight tracks, which are long straight lines of adjoining pixels whose lengths depend on the incidence angle of their incoming particles.

In Figure 4.2.1, a list of archetypical examples of each cluster type is shown. The particle type can often be distinguished by this simple categorization. For instance, a long, thin, straight track will undoubtedly be a MIP whose incidence angle can be calculated through measurement of its track's length, whereas a meandering thin track will be that of an electron whose energy is high enough to give it a range spanning several pixels.

4.3. Heavy Blobs and Tracks

In ATLAS, the vast majority of cluster types that are observed in TPX and TPX3 detectors are dots and small blobs produced by photons, followed by curly tracks coming from high energy electrons, and straight tracks, usually created by occasional muons. While proton-proton collisions do not favour the production of atomic nuclei, which would produce heavy blobs and tracks in TPX3 detectors, neutrons, which are detected using ^{6}LiF (thermal neutrons) and polyethylene (fast neutrons) converter layers placed on top of the silicon sensors, will produce such blobs[56]. Since the energies of the recoil protons and α-particles involved in these secondary processes possess energies that are very close to one another — 2.73 MeV for recoil protons and 2.03 MeV for α-particles — it requires dividing the sensor into regions covered separately by each converter material. This has the obvious consequence of reducing the cross sectional area that is collecting these neutrons. The upside is that there are now dedicated regions for fast and thermal neutrons respectively, but with lower statistics for each.

Thermal and fast neutrons are then separated through comparison to the uncovered sensor region with the knowledge that:

$$n + Si \longrightarrow p + Al \qquad (4.3.1)$$

and

$$n + Si \longrightarrow \alpha + Mg \qquad (4.3.2)$$

reactions still occur there. Aluminum foil 80 μm thick can be placed over the polyethylene layer, providing a kinematic threshold of approximately 4 MeV.[48]

If it were possible to distinguish between the proton and α-particle clusters simply on the basis of cluster morphology, their similar energies notwithstanding, this would eliminate the need for dedicated neutron converter regions. Consequently, this would allow for an increase of the collection surface area and a higher sample size of neutrons.

4.4. Ion Measurement

In the paper that follows and the study described therein, the focus is on heavy blobs and heavy tracks and the physical parameters that determine their sizes.

A matter of great importance is the calculation of correct deposited energy values for beams of a variety of different ions. In gold foil RBS, ions will lose energy through scattering as well as through stopping across the travelled path in the gold, given by its thickness $D_{Au}/\cos\theta$, where θ, in this case, is $45°$. This leads to a range of energies exiting the gold foil for a monoenergetic beam of a given particle. The maximum and minimum energies of particles emerging from the foil can therefore be calculated. The particle that undergoes a $90°$ scattering process first, and then loses energy through stopping across the travelled path in gold gives a minimum energy, whereas the particle that undergoes stopping through the gold foil and subsequently scatters at $90°$ before exiting the foil provides the maximum energy. The beam of particles emerging from the foil will then have an energy representing the average of these limiting energies. A diagram of the process is shown in Figure 4.4.1.

In the case of He nuclei, these were obtained from an ^{241}Am source with a face 1 cm in diameter. The source was placed in a secured holder, in the vacuum chamber that was used for beam measurements, at a distance of 4 cm away from the sensor. An aluminum foil covered the source in order to slow the He nuclei to achieve a lower deposited energy. One consequence that this different setup has on the results of the measurement is that it widens the deposited energy distribution. The reason for this comes from the necessity of placing the source so close to the sensor, precluding its consideration as a point source. The lowest deposited energy He nuclei will travel at $0°$ through the stopping aluminum foil and through the inactive layers, whereas the maximum angle of approach is approximately $13°$ for nuclei incident at the edges of the sensor, and up to $17°$ for nuclei incident at the corners. In the latter case, the energy loss experienced due to the additional path through various inactive materials can be as great as $\sim$250 keV.
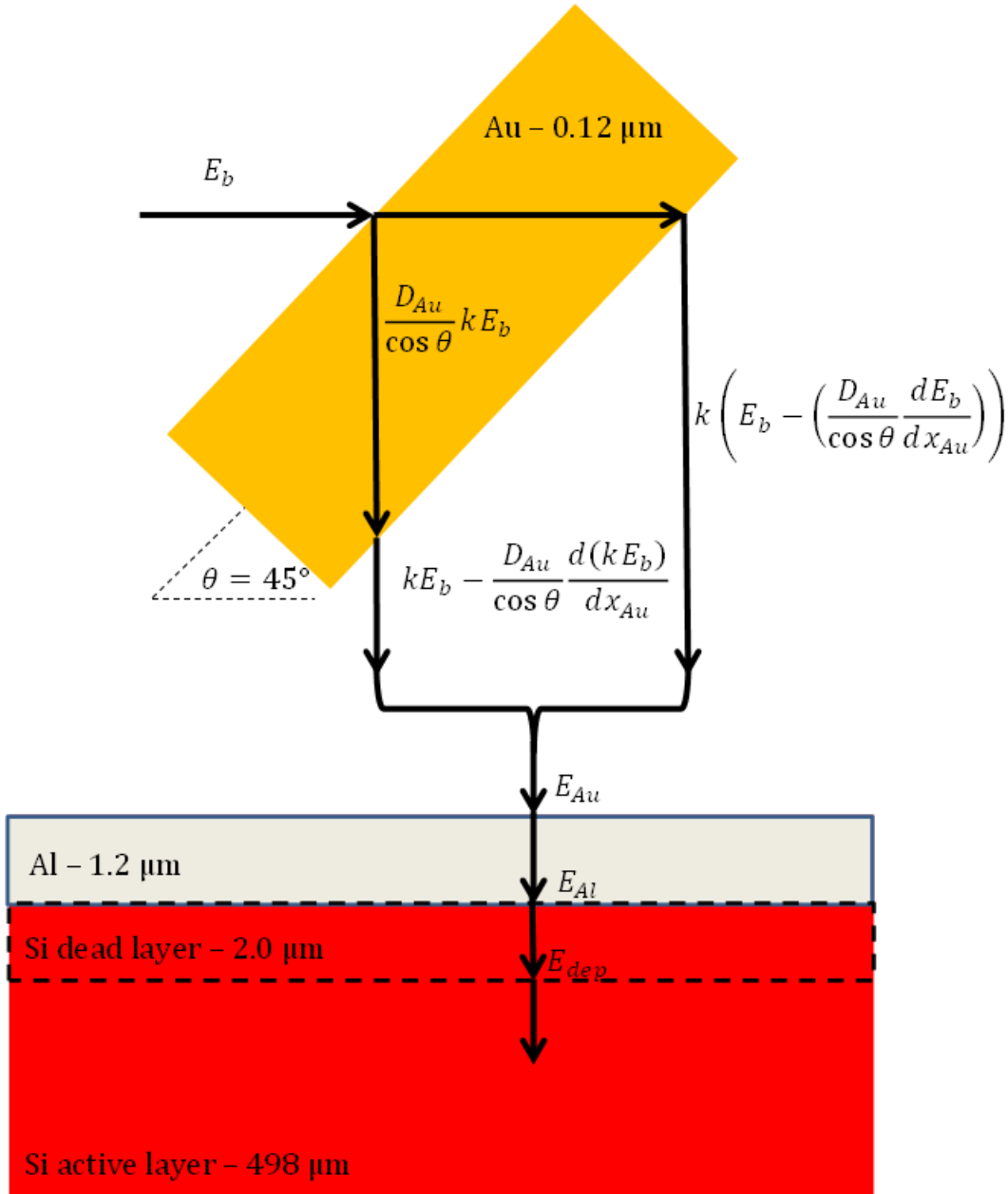
Fig. 4.4.1. The RBS process including stopping across the Au foil. Indicated energies correspond to the energy of the particle at each region. E_{Au} is the average of the maximum and minimum energies emerging from the Au foil, E_{Al} is the energy of the particle at the end of its path through the Al layer, and E_{dep} is the energy deposited in the active layer of the sensor, after losses in the dead layer have been subtracted.

4.5. Publication: Charge sharing investigation in a Timepix3 (TPX3) detector through ion probing

My contributions to this publication are:

- Experimental design;

- Detector calibration;

- Collection of data;

- Analysis of data;

- Authorship of article.

Charge sharing investigation in a Timepix3 (TPX3) detector through ion probing

C. Leroy, C. Papadatos*, M. Usman, M. Boussa

Groupe de physique des particules, Université de Montreal

_____

*Corresponding author

4.5.1. Abstract

The phenomenon of charge sharing in pixelated particle detectors and its relationship to a variety of physical parameters is investigated using a Timepix3 (TPX3) detector with a 500 μm thick silicon sensor. A probing technique is used with H, Li, and C ion beams produced at the Tandem Van de Graaff (VdG) accelerator at the University of Montreal (UdeM), as well as alpha particles from an ^{241}Am radioactive source, to determine a direct relationship between particle depth and cluster size. Additionally, the primacy of a particle's energy on the determination of its corresponding cluster's size is confirmed.

4.5.2. Introduction

All measurements reported in this study were performed using a Timepix3 (TPX3) device. This device is a hybrid pixel detector which consists of a 500 μm thick silicon layer bump-bonded to an integrated circuit (ASIC). The sensor is divided into a matrix of $256{\times}256$ square pixels with a pitch of 55 μm. It has time over threshold (ToT) and time of arrival (ToA, time granularity of 1.56 ns) capabilities in a self-triggered readout scheme (data driven)[2]. One of the advantages of high precision pixelated detectors, such as the TPX3 detector is their ability to identify a variety of particle species through indirect detection (photons, neutrons) and direct detection (charged particles). This can be done through analysis of the shapes and sizes of the tracks left by incident particles in the pixel matrix. Heavy ionizing particles such as ions create large clusters of pixels that have registered hits. These so-called "heavy blobs" are symmetrical and circular in appearance, spanning multiple pixels for a single particle[53].

Several physical parameters determine how much charge is shared between pixels, as this is the consequence of carrier drift within the sensor which, in the case of this TPX3-Si device, comes from hole collection [51]. These parameters include: incident energy, incident angle, applied bias and internal electric field, sensor temperature, and penetration depth of the incoming particle. A higher particle energy will create more charge carriers, thus increasing the pixel area of a cluster. Angled incidence will deform the circular symmetry of a blob

94

by elongating its form. The internal electric field strength determines how fast charges get collected by the electrodes, and therefore, how much time they have to diffuse radially from their point of creation. A higher external bias thus produces smaller cluster sizes. Increasing the sensor temperature effectively reduces the internal bias and, therefore, increases charge sharing. This temperature effect on clustering in this TPX3-Si is investigated in another work [20]. Lastly, penetration depth influences the cluster size such that charge carriers which are produced further away from the collecting electrodes will take more time to be collected than those which are located closer. In principle, this longer drift time creates larger clusters.

4.5.3. Methods

All measurements were performed at the Tandem VdG beam facility at UdeM, under a high vacuum of 4×10^{-7} Torr. For all beam measurements, Rutherford Backscattering (RBS) was performed at $90°$ from the main beam line, through a 0.12 μm gold foil into the integrated detector chamber, where they were measured by the TPX3[20]. Measurement of alpha particles using the source was also performed with the TPX3 in the same position but with the VdG beam turned off.

The measurements were divided into two sets according to specific parameter under investigation. The first set targeted a constant deposited energy in the active layer of the sensor for all investigated ion species, while the depth remained variable. Figure 4.5.1 shows the range of a simulated group of low Z nuclei in silicon for a given energy of 3 MeV for each ion species[39]. The second set probed the sensor at constant depth for each ion species, which was made possible by depositing a unique energy for each. In this way, the isolated influence of depth or energy on cluster size could be studied, independent of the other. The internal field was kept fixed due to the application of a constant bias of 230 V for all measurements. This value is determined to represent a fully depleted sensor, as shown in Figure 5.2.1, where the number of photon hits are shown as a function of the applied bias,
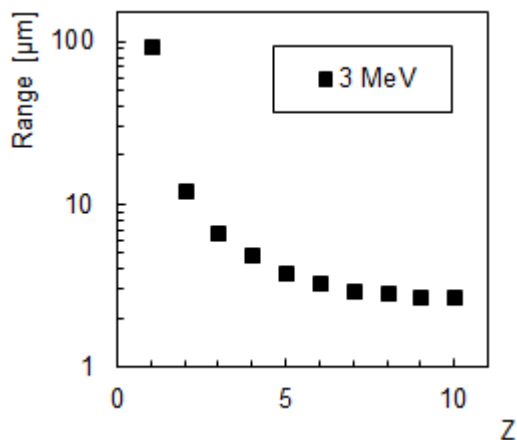
Fig. 4.5.1. Range of 3 MeV particles in silicon as a function of their atomic number, calculated using a SRIM simulation [**39**].

using fluorescent x-rays created with an x-ray tube that irradiated a copper plate. Higher values of bias voltage are usually avoided in standard operation to limit noise.

The temperature of the sensor was measured to have remained constant for all measurements at approximately 95°C, removing its ability to vary the cluster size from measurement to measurement. This temperature is reached during the TPX3's operation in vacuum, where the only dissipative cooling process is heat transfer through the supporting steel backplate. Lastly, the angle of incidence was kept at 0° normal to the sensor plane.

The influence of the applied bias was investigated for each ion by performing a scan of several bias voltages from 10 V to 230 V. In this case, nearly all parameters but that of the field remained constant. The one exception is the deposited energy, due to incomplete depletion at lower bias voltages. The implications of this fact are detailed in the discussion section.

A general study of the impact angle's effect on cluster size was performed using protons with beam energies of 3 - 9 MeV in steps of 1 MeV, with angles of incidence of 0° to 75° in increments of 15° for each energy. This angle scan measurement was done at a constant bias of 230 V as well. Lastly, the measurements of protons at multiple beam energies provided a range of cluster energies, enabling further investigation into the cluster energy - cluster size relationship.
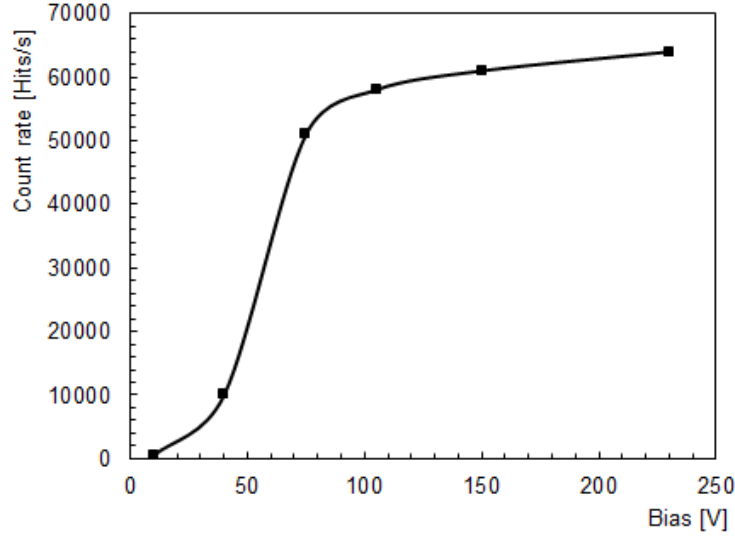
Fig. 4.5.2. Count rate of photons (x-ray fluorescence) as a function of applied bias. The maximum count rate is observed at 230 V within a plateau of small slope, indicating a fully depleted layer of Si.

4.5.3.1. Source measurement. He nuclei were measured with TPX3-Si using alpha particles from an ^{241}Am source. After losses in the surface dead layers of the sensor, 5.1 MeV were deposited in the active layer, which corresponded to a particle range of 25 μm [**39**]. This range represented the target probing range for later ion beam measurements.

Likewise, a measurement with the same ^{241}Am source was performed placing a thin aluminum foil (13 μm) between the source and the detector, with both being placed in the detector's vacuum chamber (4×10^{-7} Torr). In this setup, the emitted source energy of 5.49 MeV can be reduced through stopping in the filter, the contact, and the dead layer, down to 3 MeV. Thus, 3 MeV represented the target energy for the ion beam measurements as well.

4.5.3.2. Beam measurements. Ion measurements were carried out at the UdeM Tandem Van der Graaff accelerator using H, Li, and C ions as probing particles. Each beam was measured after undergoing RBS through a gold foil 0.12 μm thick at an angle of 90° to the beam line using a TPX3 detector equipped with a silicon sensor 500 μm thick. In all cases, the measurements were again taken under high vacuum conditions (4×10^{-7} Torr).

As mentioned, the 3 MeV target energy was based primarily on the limitations of the source measurement. Lower alpha energies could have been possible, for example, using more

or thicker stopping filters, however, consideration was taken in order to allow for sufficient penetration of the longest range probe, the proton, at 96 μm for 3 MeV deposited energy, so as to increase the spread in range between the longest and shortest probing particles in this analysis.

Technical limitations also prohibited going much higher than 3 MeV, assuming thinner filters were used for the source measurement. This is due to the energy ceiling of the VdG accelerator for heavier ions. Increasing the target energy would have eliminated the possibility of using a C beam, thus reducing the number of ion points in the analysis to three. Consequently, the selection of ions was restricted to the listed four. For ions heavier than carbon, the beam energy required to probe 25 μm into the sensor was too great (over 35 MeV for oxygen). For carbon ions to reach 25 μm, a beam of 27 MeV was needed, which was the highest beam energy used in this study. Additionally, Be and B sources were unavailable for use. Conveniently, the use of low Z probes is advantageous since this offers the widest spread in terms of penetrating power between ions than would a group of ions with higher Z.

4.5.3.3. Energy calculation. The TPX3-Si chip is composed of several inactive layers of material on its surface. These include a 1.2 μm aluminum contact, and a 2.0 μm thin dead layer of silicon, which does not become depleted and, therefore, does not create charge carriers during an ionizing particle's path through it. In order to determine the beam energies necessary to deposit the required energy, 3 MeV, in the active sensor, at normal incidence, the following calculation was performed for each ion beam:

$$E_{Au} = \frac{\left(kE_b - \left(\frac{D_{Au}}{\cos\theta}\right)\left(\frac{d(kE_b)}{dx_{Au}}\right)\right) + k\left(E_b - \left(\frac{D_{Au}}{\cos\theta}\right)\left(\frac{dE_b}{dx_{Au}}\right)\right)}{2} \qquad (4.5.1)$$

$$E_{Al} = E_{Au} - D_{Al}\left(\frac{dE_{Au}}{dx}\right)_{Al} \qquad (4.5.2)$$

$$E_{dep} = E_{Al} - D_{Si}\left(\frac{dE_{Al}}{dx}\right)_{Si} \qquad (4.5.3)$$
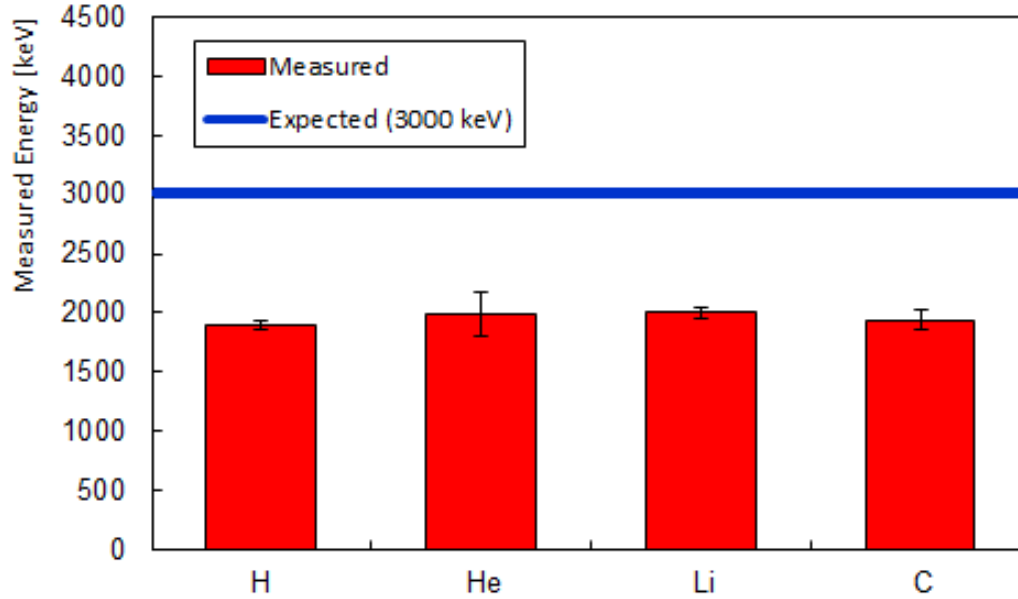
Fig. 4.5.3. Measured energies for H, He, Li, and C ions compared to the expected deposited energy of 3000 keV obtained through the calculation (Eqs. 2.1-2.3). The measured energies average to a value of 1957 keV. Error bars represent the full width at half maximum of the gaussian fit functions applied to the energy distributions.

where E_b is the beam energy, E_{Au} is the ion energy upon exiting the Au foil, E_{Al} is the ion energy upon exiting the Al contact, and E_{dep} is the ion energy upon exiting the Si dead layer. E_{dep} is equal to the energy deposited in the active layer of the sensor at normal incidence. D_{Au} represents the thickness of the Au foil used for RBS (0.12 μm), D_{Al} is the thickness of the Al layer on top of the sensor (1.2 μm), D_{Si} is the thickness of the Si dead layer (2 μm), and k is the kinematical factor in RBS in gold at a 90° scattering angle. The result of this calculation (Eq. 2.1 - Eq. 2.3) applied to the four ion species is shown in Figure 4.5.3. The measured energies are all lower than the calculated energy due to charge saturation effects in pixels which receive the greatest amount of deposited energy. Nonetheless, consistent deposited energies have been measured between ion species.

4.5.4. Results

Figure 4.5.4 shows the impact of deposited energy and angle of incidence on the extent of charge sharing, represented by the cluster size parameter. These are energies deposited after scattering in the gold foil and partial stopping in the Al and Si inactive layers, therefore

greater incident angles will cause more energy losses. Figure 4.5.5 shows the cluster size measured for each 3 MeV ion measurement, for each angle of incidence that was measured. The linear fit applied to these points yields a relationship of the form CS= $(0.03016 \pm 0.00048)E_{dep} + (15.8 \pm 1.2)$, with $R^2 = 0.99$, where CS is the cluster size and E is the deposited energy in keV. Cluster sizes were also evaluated over a varying bias scan for each ion measurement series. This is shown in Figure 4.5.6. Figure 4.5.7 shows the cluster size variation with each measured ion according to the particle's range in Si. Cluster size is seen to drop off with range according to the fit function CS= $(-0.056 \pm 0.012)range + (109.96 \pm 0.56)$, with $R^2 = 0.92$, where CS is cluster size expressed in the number of pixels and $range$ is the particle's range in μm.

Maintaining a constant 25 μm depth of carrier pair creation, Figures 4.5.8a and 4.5.8b display how cluster sizes are affected. The deposited energy E_{dep} is calculated, as in Eqs. 2.1 - 2.3, by subtracting energy losses due to stopping in the Au foil, the Al contact electrode, and the inactive layer of Si from the initial beam energy E_b. With respect to the deposited energy, cluster size varies as CS= $(96.4 \pm 8.5) \ln(E_{dep}) - (648 \pm 74)$, with E_{dep} expressed in keV and $R^2 = 0.98$. Evaluated against measured energy, which represents the energy measured by the TPX3 and reconstructed from its calibration, CS= $(0.0634 \pm 0.0083)E_{meas} - (19 \pm 30)$ with E_{meas} in keV and $R^2 = 0.97$.

4.5.5. Discussion

Dependence of cluster size on each parameter (angle of incidence, energy, bias, particle range) was evaluated, keeping the rest fixed. First, Figure 4.5.4 shows the behaviour of the cluster sizes for protons only, at varying angles of incidence, for a series of energies between 3 MeV and 9 MeV. Several features emerge from this plot. At first glance, the size seems to depend highly on the angle of incidence, especially as the energy is increased. However, this is an incomplete picture, since one must consider energy as the driving factor behind cluster sizes. Figure 4.5.5 demonstrates this fact, showing a proportional relationship between deposited energy and the resulting cluster sizes. This applies for all ion species which
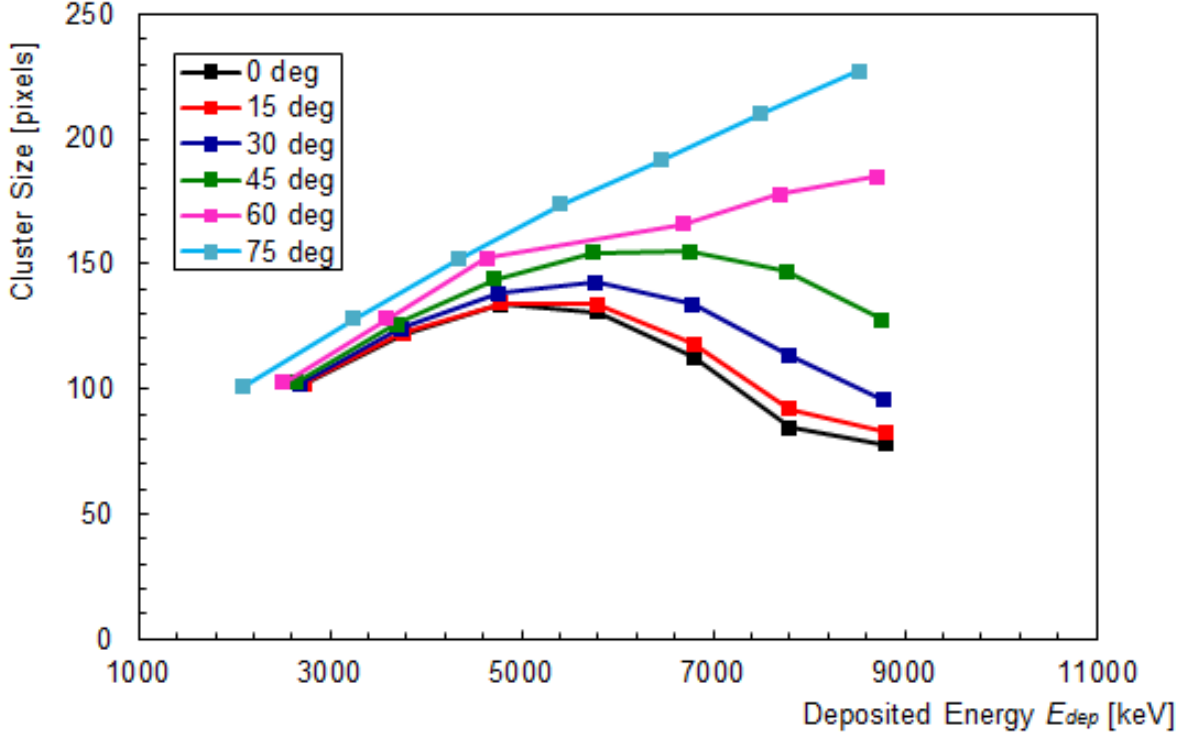
Fig. 4.5.4. Cluster sizes (CS) as a function of deposited energy (E_{dep}) for proton beams between 3 MeV and 9 MeV, carried out for different incident angles, from 0° up to 75°. Note that each particle deposits a reduced energy after partial stopping in the inactive layers of the sensor. Cluster size is shown to be highly dependent on a particle's deposited energy. The energy deposited is less than the beam energy and decreases as the incident angle increases due to greater stopping in the sensor's inactive layers. Error bars are too small to be resolved in this plot.

were deposited with normal incidence at 3 MeV incident energy. In Figure 4.5.5, rather than increasing the beam energy, the angle of incidence was increased. As a consequence, more charge is lost in the dead layers, reducing the energy that is deposited in the active layer of the sensor. In doing so, one decreases the amount of charge lost through charge saturation in pixels that would have normally received high energy depositions.

The effect of bias on cluster size is confirmed in Figure 4.5.6. There are two distinct bias ranges that indicate the presence of two main drivers of charge sharing. The first is that of energy deposition increasing the cluster size between 0 V and approximately 90 V. In this range, the layer of Si is rapidly reaching full depletion, thereby enabling the collection of more charge as bias is increased. Beyond this point, each additional bias increase only
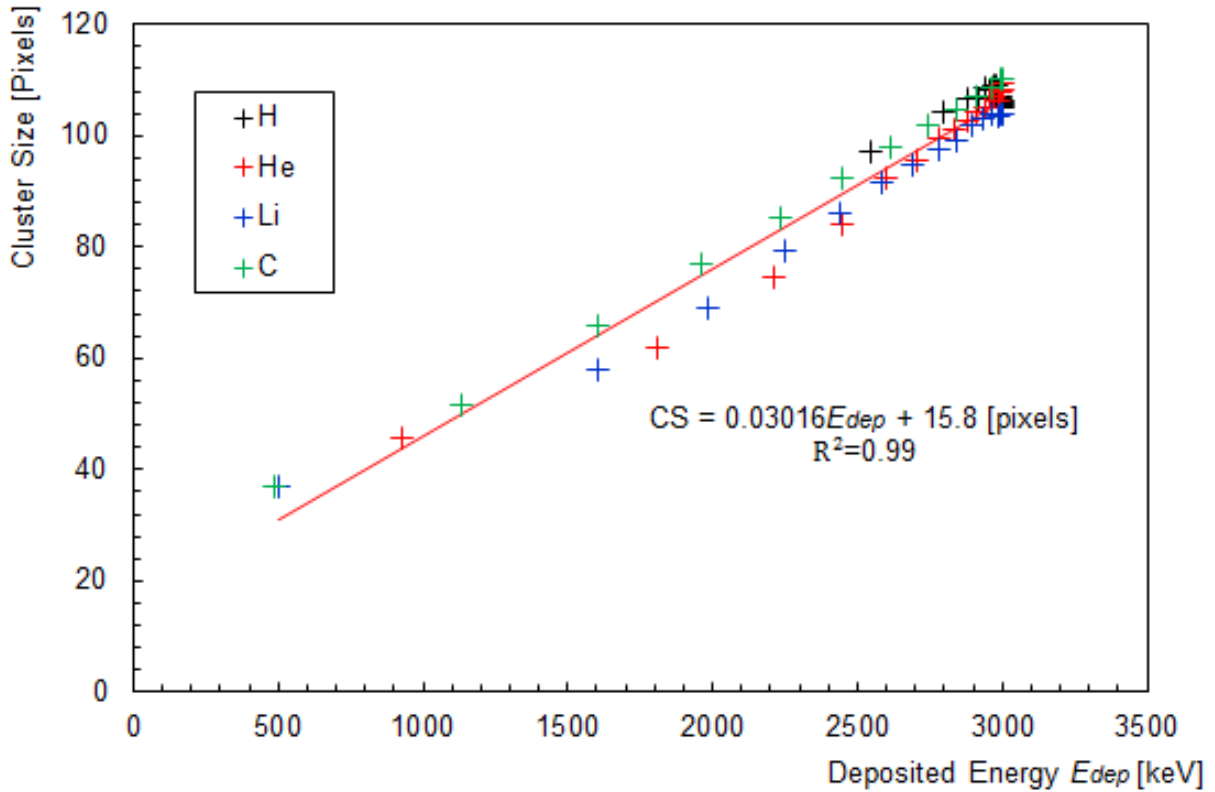
Fig. 4.5.5. Measured cluster sizes (CS) for the four ion species at an incident beam energy of 3 MeV for all measured angles of incidence from 0° up to 75°. The deposited energy (E_{dep}) is reduced for higher angles due to the longer ranges travelled through the inactive parts of the sensor. A linear fit is applied confirming the relationship of cluster sizes on deposited energy.

marginally increases the depleted thickness and the collected charge. Alternatively, it is beyond this point that the pronounced effect of the electric field begins to dominate. As the bias continues to increase, the electric field becomes stronger, accelerating charge carriers towards the electrodes and limiting them from laterally radiating away from their points of creation. This leads to the decrease in observed cluster sizes at high biases.

In Figure 4.5.7, since the energy, bias, angle, and temperature are held constant, the only changing parameter is the ion species, and therefore, its range in the sensor. It is found that the amount of charge sharing is higher for low ranges (measured from the front face of the sensor which receives the beam first). Charge sharing decreases on average by as much as 5 pixels for particles that probe around 87 μm into the sensor. This means that, since the charges — in this case holes — are collected on the cathode (the back side, closest to
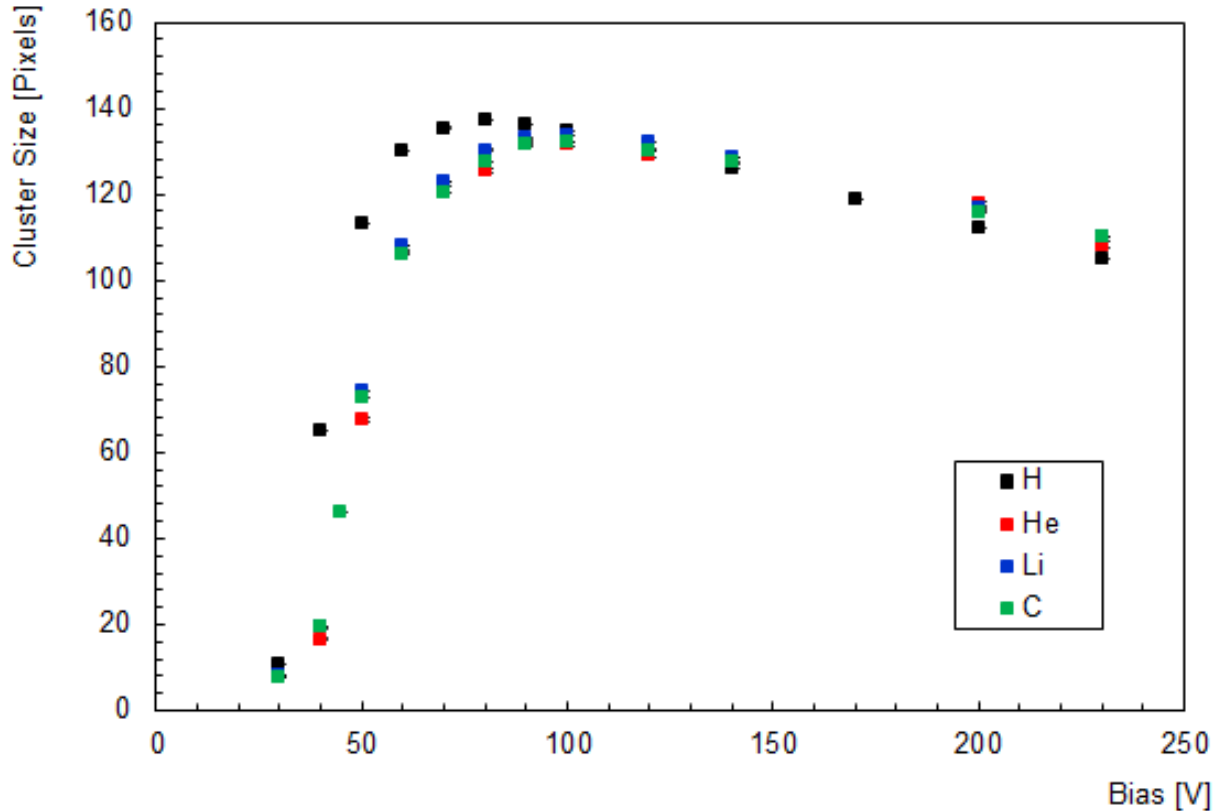
Fig. 4.5.6. Cluster sizes as a function of applied bias voltage for the four ion species at a constant 3 MeV deposited energy. All measurements were done at normal incidence. Error bars are too small to be resolved in this plot. The initial increase in cluster size is produced by an increasing depletion region, collecting more charge, followed by a gradual size decrease for higher bias, as the charges are collected before being able to drift radially.

the chipboard), the extra distance that low range ions need for their carriers to travel to be collected allows those carriers to drift radially into neighbouring pixels. The large error bars on the He point are explained by the fact that this measurement was done using a source placed at short distance away from the sensor. This causes alphas to be incident on the detector at angles that deviate from 0°. These deviated alphas lose more energy across the dead layers since their trajectories there are longer, resulting in lower deposited energies in the sensor and therefore, wider energy and cluster size distributions, since cluster size is mainly proportional to energy.

Finally, it is seen in Figure 4.5.8b that the dominant relationship between cluster size and measured energy is maintained. The purpose of these measurements was to keep range, bias, angle, and temperature fixed, such that only energy changes may drive charge sharing. This
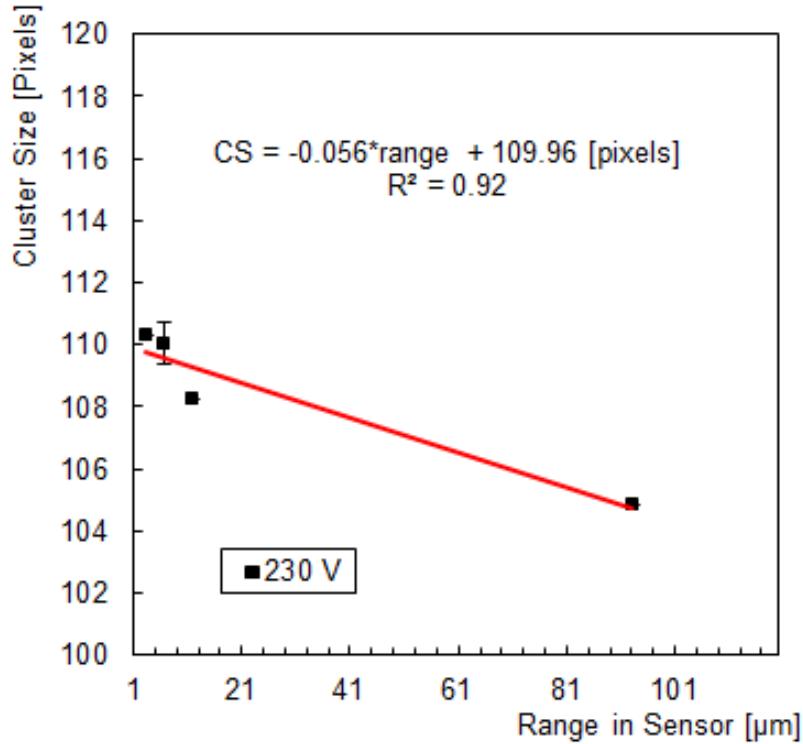
Fig. 4.5.7. Cluster sizes of four measured ion species at constant 3 MeV deposited energy as a function of range. The applied bias was kept at 230 V and measurements were done at normal incidence. The error on the He point is larger due to the higher variation in the deposited energy from the source measurement.

can then provide a clearer picture as to the exact role that energy plays in determining how large clusters will be, as opposed to the results obtained in Figure 4.5.4, where the energy was subject to variation based on the angle of incidence cutting off charge in the dead layers at high angles.

Charge sharing in heavy blobs, therefore, tends to saturate as the deposited particle energy is increased, and does not follow a linear relationship. Turning now to the energy measured by the detector using a per pixel calibration[16] (Figure 4.5.8b), the expected proportional relationship once again is found. The dissimilarity between the two plots shows the degree by which charge saturation alone can, not only affect the energy measured in the TPX3, but also the cluster sizes, which can have important implications when attempting particle recognition.
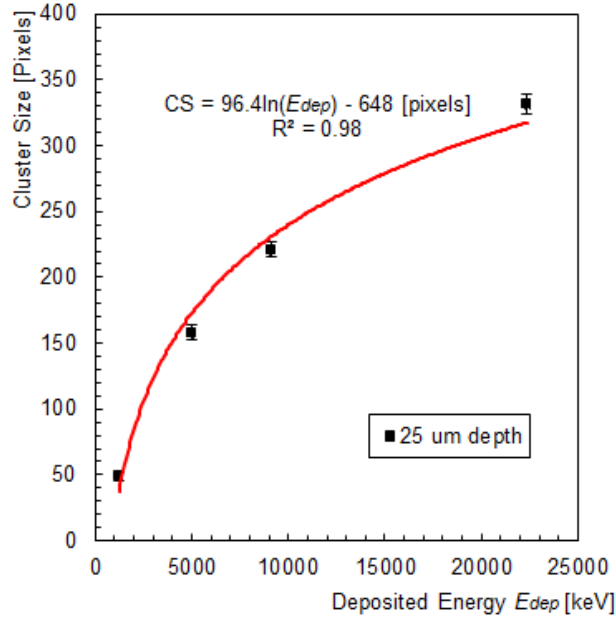
(a) Deposited Energy.
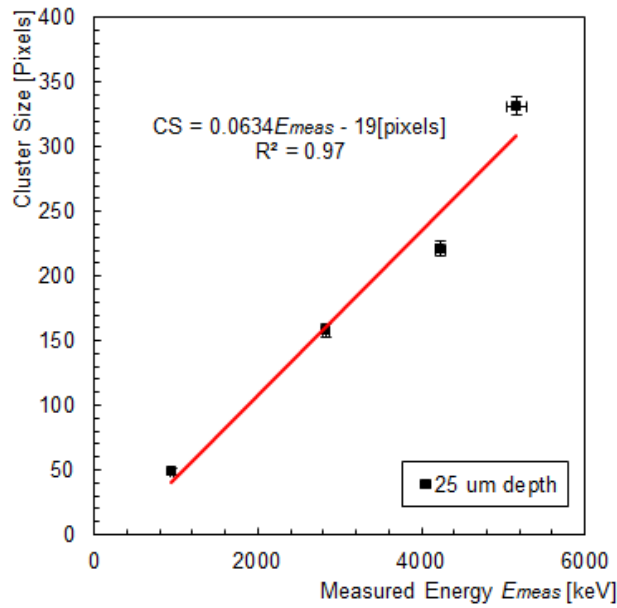
(b) Measured Energy.

Fig. 4.5.8. Cluster sizes of four measured ion species at constant 25 μm range and variable energy: a) deposited energy E_{dep} after ion stopping in the Au foil, Al contact, and Si dead layer, and b) measured energy E_{meas}. The applied bias was kept at 230 V and measurements were done at normal incidence. Energy represents the only parameter affecting cluster size here.

4.5.6. Conclusion

The dependence of charge sharing on a number of physical quantities was evaluated through cluster size investigations using H, He, Li, and C ions at energies ranging from 3 to 27 MeV. The quantities investigated were particle energy and charge created in the sensor, detector bias, incident angle, and particle range. Energy was revealed to be the primary driver of charge sharing between pixels. The relationship between charge sharing and bias was described, linking it to both the increasing charge resulting from a larger depletion thickness and the increasing internal electric field. It was also observed that cluster size does indeed correlate weakly with particle range through the application of an ion measurement process which fixed each particle's incident energy at a constant value, while varying its range in the sensor.

Acknowledgments

Chapter 5

Context

An important area of interest for the ATLAS-TPX3 collaboration is that of neutron measurements. Neutrons are measured using converters of different materials layered in a mosaic upon the sensor area in order to discriminate between neutrons of different energy ranges [**48**]. For thermal neutrons, nuclear reactions in ^{6}LiF layers generate 2.73 MeV α-particles and 2.03 MeV tritium which are then detected in the Si sensor. For fast neutrons, polyethylene (C_2H_4) is used to produce recoil nuclei, often those of hydrogen, that go on to be detected in the sensor. Kinematic suppression at around 4 MeV can be done through the placement of an 80 μm thick Al layer between part of the polyethylene converter and the sensor. In this way, the ^{28}Si(n,p)^{28}Al reaction can be suppressed from the rest of the neutron signal in the C_2H_4 region through the stopping of the protons that this reaction generates.

Neutron signals therefore are always characterized as low atomic number nuclei like hydrogen (proton signal) or helium (α-particle signal) that have energies that occupy a small range around 2-3 MeV. Presently, neutron discrimination relies upon cluster counting in the designated mosaic regions on the device — either the ^{6}LiF layer for thermal neutrons or the C_2H_4 for fast neutrons. Within the ^{6}LiF layer, it is assumed that pairs of ionizing particles correspond to one neutron event. This is an incomplete picture, however, as both the two particles in the reaction pair will not necessarily reach the sensor due to one getting absorbed in the layer. This leads to an underestimation of neutron events during analysis on account of the lower number of blobs which are observed that should each pair up with another blob

in principle. It is worth noting that the range of α-particles in the ^{6}LiF layer is also much shorter than that tritium, meaning that the tritium events are always overrepresented. Another part of the challenge is that discrimination between the α-particles and the protons are very difficult using the current understanding of clustering. This was, in part, the motivation behind the clustering study in Article 2 [21].

Additionally, the energies associated with each particle differ by a mere 0.70 MeV, making spectroscopic discrimination difficult with the current calibration techniques.

5.1. Device Threshold and Equalization

In principle the first point on the calibration curve is given by the device's threshold energy. This is the minimum energy value which can be measured by the detector. For the present detector, this value is 2.7 keV, and is determined by means of a scan on the detector performed using x-rays and extracted through a threshold equalization of the entire pixel matrix. The need for an equalization emerges from the fact that each pixel can be considered as an independent diode. Just as each pixel must be calibrated independently, so too must it possess its own threshold energy. The threshold equalization procedure aims to render all these thresholds as homogeneous as possible. The equalization scan performed on the present TPX3 is displayed in Figure 5.1.1.

5.2. Energy Calibration in TPX3

The energy calibration technique that is commonly employed by the ATLAS-TPX3 collaboration, and in most TPX3 research, uses the fluorescence of x-rays ranging between 4 keV and 60 keV to obtain a calibration curve for each pixel in the pixel array [16]. In this procedure, a TPX3 is exposed to x-rays corresponding to the fluorescence peaks of a number of metals for the approximate energy range of 2 - 30 keV. For the device used in this work, these were titanium, copper, zirconium, and cadmium samples that were irradiated with a beam of x-rays emitted by an Amptek Mini-X x-ray tube, as shown in Figure 5.2.2. In some instances, lead may also be used, however this was not the case for the current device. The

M6-W00036 Equalization

	Mean	Std. Dev.	Pixel Hits
Low Th	1535.03	18.97	65530
High Th	1678.97	19.84	65530
Final Th	1612.02	3.3	65522

Masked pixels: 6
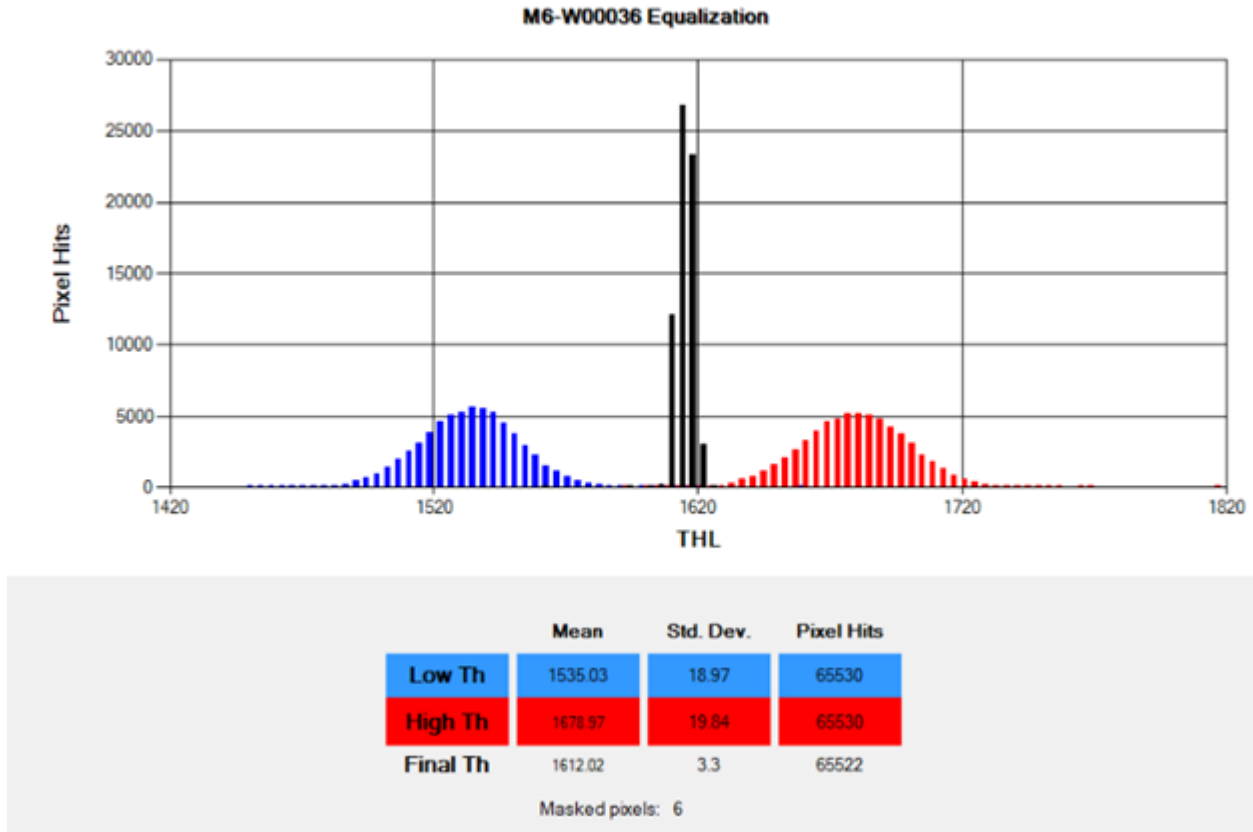
Fig. 5.1.1. The threshold (THL) equalization of the pixel matrix for the current TPX3 device. The blue and red distributions represent the minimum (Low Th) and maximum (High Th) noise edge responses for all the pixels. The black distribution represents the mean threshold value across the entire matrix.

Source	Energy (keV)
Ti	4.512
Cu	8.046
Zr	15.775
Cd	23.173
^{241}Am	59.5409

Table 5.2.1. Calibration sources and their x-ray energies used in the conventional TPX3 calibration.

last calibration point comes from x-rays emitted by an ^{241}Am source. The x-ray energies for each source are given in Table 5.2.1. All calibration points were collected at an operational bias voltage of 230 V (see Figure 5.2.1).

109
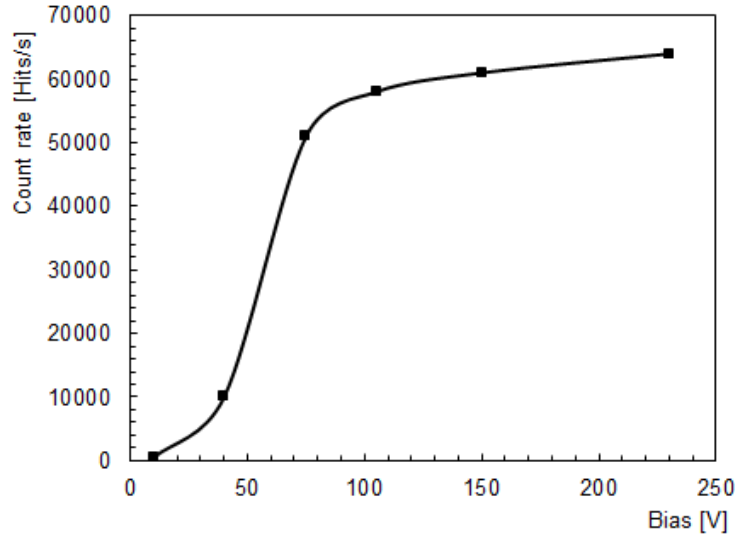
Fig. 5.2.1. Count rate of photons (x-ray fluorescence) as a function of applied bias. The maximum count rate is observed at 230 V within a plateau of small slope, indicating a fully depleted layer of Si.

Fig. 5.2.2. The TPX3-Si, connected with a Katherine interface[50], in the calibration setup. The detector, fluorescence sample (Cu is shown), and Amptek Mini-X tube are housed in a radiation-hermetic lead lined box. The calibration is performed at the IEAP in Prague.

From a practical standpoint, ^{241}Am is the highest energy photon source that can be used as a calibration point for 55 μm pixels. This limit in energy is due to the observed increase in charge sharing for higher energy photons, making it increasingly rare to observe single

pixel events. The consequence of this limit is that the linear calibration curve is only valid for each pixel up to around 500 keV. It is worth noting that this value is widely variable in the literature and is sometimes cited as low as 400 keV and as high as 800 keV [**57, ?, 58**]. For the current device, a limit of around 500 keV has been seen to be valid. Beyond this per-pixel energy, collected charge is observed to be saturated and the measured energy actually underestimates the true deposited energy of the particle.

Nevertheless, for each calibration energy, mean ToT values for each pixel are measured upon x-ray irradiation coming from the sources and a relationship between ToT and keV energy is determined. This relationship is fitted with the parametrized function[**16**]:

$$ToT = aE + b - \frac{c}{E - t},\tag{5.2.1}$$

where a, b, c, t are parameters (t is the threshold), different for each pixel, and E is the deposited energy. It can be seen analytically that, as the measured energy approaches the threshold t, the relationship deviates from linearity. Conversely, for large values of E, the relationship is treated as linear. In fact, this linearity is so strong that it allows one to cover the 5 - 500 keV range using only calibration points below 60 keV.

5.3. Publication: A proposed energy calibration procedure taking into account high per pixel energies using a silicon TPX3 detector

My contributions to this publication are:

- Experimental design;
- Detector calibration;
- Collection of data;
- Analysis of data;
- Authorship of article.

A proposed calibration procedure taking into account high per pixel energies using a silicon TPX3 detector

C. Leroy, C. Papadatos[*]

Groupe de physique des particules, Université de Montreal

[*]Corresponding author

5.3.1. Abstract

An adapted method to the conventional per-pixel energy calibration technique is proposed using a Timepix3 (TPX3) detector to correct energy saturation effects that become present at high per-pixel energies. The correction is based on proton measurements at energies that generate these charge saturation. Its efficiency has been tested using measurements of ions produced at the Tandem Van de Graaff (VdG) accelerator at the University of Montreal (UdeM). The adapted calibration was found to improve the accuracy of energy reconstruction. Energies given by the new calibration improve upon the conventional calibration by an average of 12.1% in the range of 1.2 MeV - 7.8 MeV deposited at normal incidence in the sensor and by 30.4% for the energy range of 2.1 MeV - 7.5 MeV deposited at 75° incidence.

5.3.2. Introduction

The conventional calibration protocol used for Timepix3 detectors [2] is performed on a per-pixel basis using x-ray fluorescence sources [16]. Its range of applicability is understood to be between 2 keV up to about 500 keV at the pixel level, where 2 keV corresponds roughly to the energy threshold achievable with a Timepix3 provided ToA functionality is disabled. The TPX3 used in this work has a threshold of 2.7 keV. Above approximately 10 keV and below 500 keV, time-over-threshold (ToT) and energy obey a linear relationship. The precise energy value at which linearity is lost at the high end is unknown, and limits as high as 850 keV can also be found in the literature [19]. Above that range, this relationship no longer applies, and larger charge concentrations in each pixel result in losses in reconstructed energy. This as well as other related charge loss phenomena are variously referred to as saturation or volcano effects [54]. Likewise, as charge concentrations in pixels increase, the result is greater charge sharing with neighbouring pixels, making a per-pixel calibration increasingly difficult for higher photon energies [53]. Corrections to this phenomenon have been proposed and tested for Timepix devices, the generation of devices that preceded TPX3 [19] [59].

When an ionizing particle creates charge carriers in silicon, the majority of the charge is created in the initial pixel. Charge will spread to neighbouring pixels, however, the initial one

will have the highest amount of charge. Knowing this, one can calculate the missing charge — i.e. the correction E_{cor} — for a given cluster by subtracting the expected deposited energy, E_{dep} of that particle from the measured energy, E_{meas}, given by the conventional calibration:

$$E_{cor} = E_{dep} - E_{meas} \tag{5.3.1}$$

To remedy the saturation effect of the standard calibration, the use of low MeV range heavy ionizing particles is proposed for additional calibration point sources. These particles produce symmetrical cluster shapes, known as "heavy blobs" over many pixels, with the incident energies approximately following a normal distribution centred around the centre of the cluster. Therefore, for small clusters, one can use the cluster's height — the energy value of the pixel containing the most charge — as an additional calibration point for that pixel. In the case of heavy blobs produced by nuclei at normal incidence, this is the centre-most pixel of the blob.

5.3.2.1. ATLAS-TPX3. TPX3 devices have been installed in the ATLAS experiment at the Large Hadron Collider and are an integral part of the TPX-ATLAS experimental program [3]. Their ability to measure energy is an important part of dosimetry studies and, amongst other applications, luminosity measurement. It could more specifically be beneficial in neutron detection studies done by TPX-ATLAS with neutron converter materials [48]. In these situations, secondary particles like alphas and tritium result from neutron interactions and possess energies of 2.05 MeV and 2.73 MeV respectively. This requires an energy calibration that extends to energies higher than those covered by the conventional calibration technique. Nevertheless, this standard technique is long established and is a standard part of the preparation of these detectors for their implementation into the ATLAS experiment. It would therefore be preferable to extend the pre-existing technique by adding to it, rather than to develop an entirely new one. Such an extension must aim to be as practical as possible for the TPX-ATLAS collaboration. It should therefore use technological and material resources that are readily available to the collaboration.

5.3.3. Methods

5.3.3.1. Calibration Points. Proton beams with known energies of 1 358, 3 117, and 4 000 keV were produced at the Tandem Van der Graaff accelerator at the University of Montreal. The beams were each measured after undergoing Rutherford backscattering (RBS) through a gold foil 0.120 ± 0.005 μm thick at 90° using a TPX3 detector equipped with a 500 μm thick silicon sensor and an energy threshold of 2.7 keV, with pixels measuring 55 μm $\times$ 55 μm each. The detector possesses inactive layers of material on its surface. The first layer through which incoming particles pass is an a 1.2 μm aluminum contact and the second is a 2.0 μm dead layer of silicon that does not become depleted at the applied bias of 230 V which was maintained for all measurements [60][1]. All measurements were taken under high vacuum (4×10^{-7} Torr). The device was connected to a computer running the Burdaman acquisition software using a Katherine readout interface [50]. The measurement of each beam lasted several minutes, such that a minimum of 1.31×10^7 proton cluster hits were recorded on the detector. This ensured that each pixel was a blob's central pixel a minimum of 200 times, and thus had at least that many instances of being a cluster height pixel.

Only the maximum pixel count per cluster was taken into account and the pixel which possessed that value was kept. To do this, custom thresholds for each energy were required since the cluster heights tend to increase with increasing proton energy. These values are given as **ToT Cut** in Table 5.3.1. All cluster height pixels whose ToT values are greater than **ToT Cut** are kept. Table 5.3.1 lists each proton beam's known initial energy, expected deposited energy in the silicon active layer after scattering through the gold foil and passage through aluminum and silicon surface layers (E_{dep}), measured energy and height using the conventional calibration (E_{meas} and CH_{meas}, respectively), measured height in terms of ToT (CH_{ToT}), and corrected cluster height energy (CH_{cor}) which represents the new calibration point energy. The value of CH_{cor} is obtained by adding E_{cor} from Eq. 5.3.1 to CH_{meas}.

---

[1]Technical information about the thickness of the inactive layers was provided by the IEAP electronics engineer who prepared the chip.

Beam Energy	E_{dep}	S_{Au}	S_{Al}	S_{Si}	E_{meas}	CH_{meas}	CH_{ToT}	CH_{cor}	ToT Cut
1,358	$1{,}243.9 \pm 47.6$	10	12	18	946.7	275.7	238.6	572.9	150.0
3,117	$2.999.6 \pm 128.7$	27	31	48	1,896.0	395.7	336.4	1,499.2	200.0
4,000	$3{,}765.5 \pm 156.2$	32	37	57	2,174.1	399.6	370.2	1,991.1	250.0

Table 5.3.1. Distribution means of energy, deposited energy in the silicon active layer (E_{dep}), straggling in gold (S_{Au}), aluminum (S_{Al}) and silicon (S_{Si}) layers, measured energy (E_{meas}) and height using the conventional calibration (CH_{meas}), height in terms of ToT (CH_{ToT}), and corrected cluster height energy (CH_{cor}). All energy values are expressed in keV, while all ToT values represent the ToT counter value.

The ToT cut on each dataset was thus dependent upon the value of CH_{ToT} recorded for each beam. The cut value was placed suitably below this mean value such that all members of the distribution exceeded it.

This creates a new dataset of single pixel clusters whose total expected cluster energies are the expected cluster height energy, calculated as the measured cluster height value added to E_{cor}. For 1,243.9 keV protons, the conventional calibration yields a measurement of 946.7 keV, indicating a loss of 297.2 keV per cluster, on average. This is E_{cor}, the energy that is missing from this measurement. The cluster height measured using the conventional calibration for the same particle is 275.7 keV. The lost energy, E_{cor}, is then added to the central (cluster height) pixel as a correction to reconstruct its original expected energy. For this proton energy, the expected cluster height becomes 572.9 keV. Therefore, this energy corresponds to a ToT value of 238.6 for this proton energy and for this pixel.

As in the standard calibration, this procedure is applied to each pixel individually. The cluster height for a given particle of a known energy does not change as it is a characteristic property of that particle, at that energy, in silicon. Were a different energy, heavy ionizing particle, or sensor material to be used, this procedure and calculation would need to be redone accordingly.

5.3.3.2. Beam and Source Measurements. The calibration's effectiveness was tested by applying it to the analysis of heavy ionizing particles across a range of low MeV energies. Protons (H nuclei) were measured using a TPX3-Si device connected to the Katherine interface for beam energies ranging from 1,358 keV to 8,000 keV at normal incidence and at an

Particle	E_{conv} (keV)	σ_{conv} (keV)	$\%Dev_{conv}$	E_{new} (keV)	σ_{new} (keV)	$\%Dev_{new}$
Li - 3,000 keV	2,002.5	99.1	-33.25	3,131.7	271.6	4.39
Li - 8,923 keV	4,231.1	120.8	-52.58	6,868.7	318.7	-23.02
C - 3,000 keV	1,940.1	165.4	-35.33	3,283.5	342.0	9.45
C - 21,923 keV	5,164.8	255.6	-76.44	9,835.0	405.5	-55.14

Table 5.3.2. Reconstructed energy means of Li and C ions for the conventional ("conv") and new calibration procedures.

incidence of 75°, the maximum angle achievable with the detector placed inside the current vacuum chamber. In addition, Li ions depositing energies of 3,000 keV and 8,923 keV as well as C ions depositing energies of 3,000 keV and 21,923 keV were measured at normal incidence to verify the validity of the calibration on heavy ionizing particles other than the ones used for the calibration (protons). The ion energies were first reconstructed with the conventional low energy calibration. This was then compared to the reconstructed energies produced using the extended high energy calibration. In all cases, the measurements were done with an applied bias on the sensor of 230 V.

5.3.4. Results

Figure 5.3.1a shows the reconstructed energies for a dataset of protons ranging from 1,400 - 8,000 keV, at normal incidence to the detector, calibrated using the conventional (in black) and the proposed new (in red) calibration procedures. Figure 5.3.1b gives the corresponding results for 75° incidence. A sample comparison between the energy spectra produced with each calibration procedure is provided in Figure 5.3.2, showing the reconstructed energy spectra of the same beam of protons depositing an expected 2,731 keV into the active part of the Si sensor. Reconstructed energies of lithium and carbon nuclei are displayed in Table 5.3.2 for both calibrations.

5.3.5. Discussion

The adapted calibration procedure improves energy reconstruction, as indicated by the deviations observed in Figures 5.3.3a and 5.3.3b, albeit with significant disadvantages. One can see the percent deviation of each measured proton energy with respect to the target
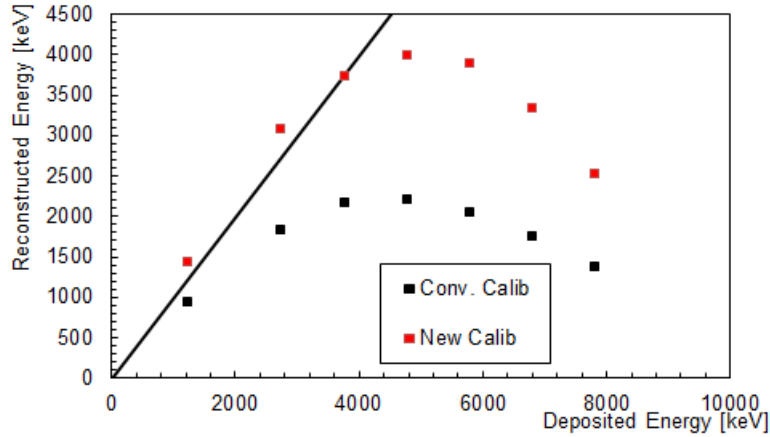
(a) $0°$.
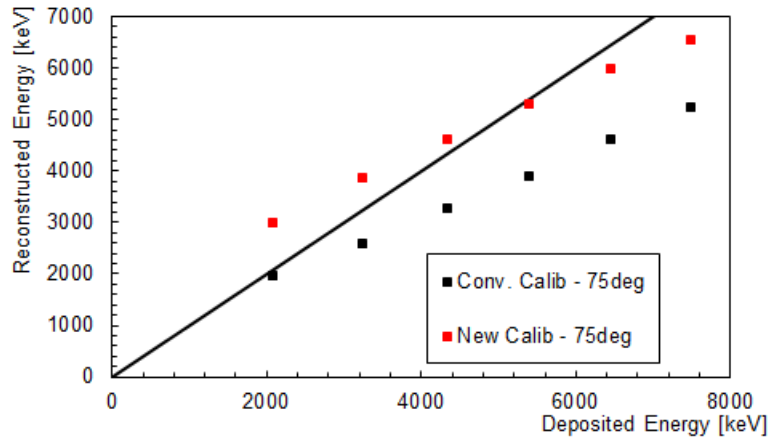
(b) $75°$.

Fig. 5.3.1. Comparison between the conventional (Conv.) calibration in black and the new calibration in red for protons at a) $0°$ incidence, and b) $75°$ incidence. In each case, a straight black line represents the ideal exact correspondence between deposited and reconstructed energies.

deposited energy. Comparing the distance of each deviation point away from the target energy, or from 0% deviation:

$$\%Improvement = \mid \%Dev_{old} \mid - \mid \%Dev_{new} \mid \qquad (5.3.2)$$

On average, the new calibration gives an improvement at normal incidence of 30.4%, with lower energy particles in particular arriving at more accurate reconstructed energy values. A more modest but still noteworthy average improvement of 12.1% is observed for protons measured at the high incidence angle limit of $75°$, as shown in Figure 5.3.3b.
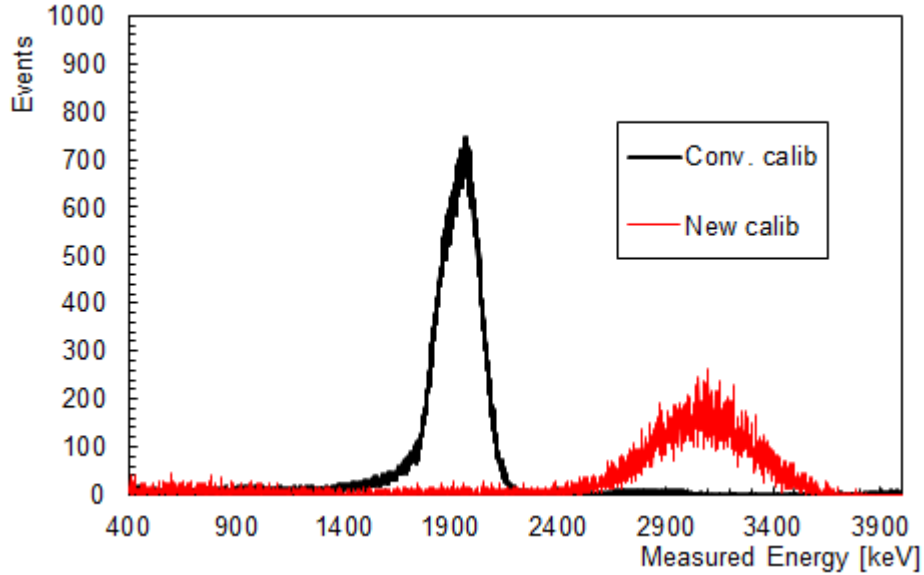
Fig. 5.3.2. Energy spectra of a 2,731 keV (deposited energy) proton beam dataset. The conventional calibration's reconstruction is shown in black and the new calibration is shown in red. The widening of the new calibration's distribution reflects a deterioration of the energy resolution.

The deviations are similarly reduced for the measured ions, as indicated in Table 5.3.2, with improvements ranging between 20%- 30% for the new calibration.

Whereas the accuracy of the new calibration has improved, allowing one to reconstruct an energy value that is closer to the expected one, the precision of the calibration is lower compared to the conventional calibration. That is, the energy resolutions calculated from the gaussian fitting of the spectral distributions are mostly larger in this new approach, as shown in Figures 5.3.4a and 5.3.4b. This feature can be seen by the widening and flattening of the new calibration's distribution in Figure 5.3.2, for 2,731 keV protons arriving at normal incidence to the sensor. An explanation for this result comes from noting the relationship between ToT and energy at energies beyond the linear regime. At these energies, the relationship between ToT and energy is no longer one-to-one [19]. The presented calibration ignores those variations and continues to assume a direct relationship between ToT and energy. The consequence of this assumption is that, while energies are shifted closer to their true values on average, ToT values which have higher deviations from the assumed linearity
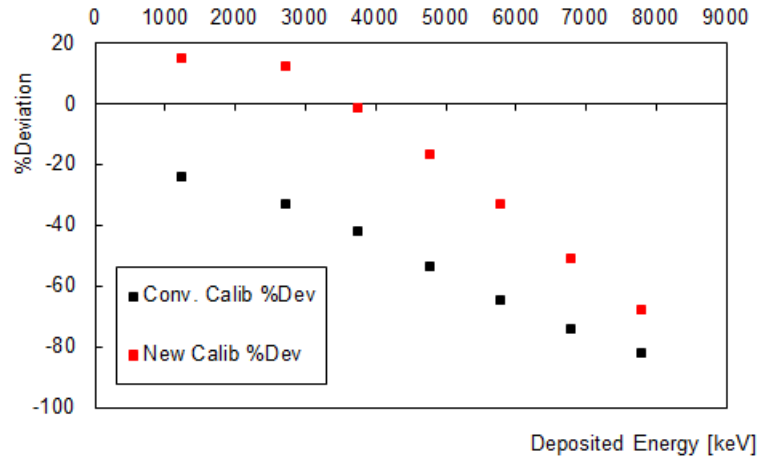
(a) 0°.
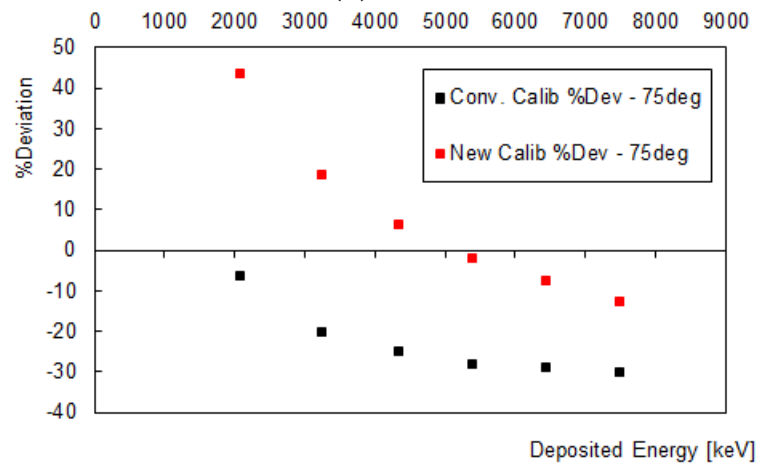
(b) 75°.

Fig. 5.3.3. Comparison between the percent deviations from the expected deposited energy values produced by the conventional (Conv.) calibration in black and the new calibration in red for protons at a) 0° incidence, and b) 75° incidence.

will be calibrated to energies which may not actually reflect their true value, yet which conform to the curve. This would thus result in a wider range of reconstructed energy values for a given proton energy.

The second main assumption of this calibration is that it is the central pixel of each cluster that experiences all the energy loss. This choice was made for two reasons. Firstly, at lower proton energies, cluster sizes are small enough to assume this to be approximately correct. This is reflected by the results showing greater accuracy in reconstructed energy for low energies. Secondly, in the absence of a well modelled cluster volume profile function which could determine how much charge should be found in each pixel, choosing any greater

121
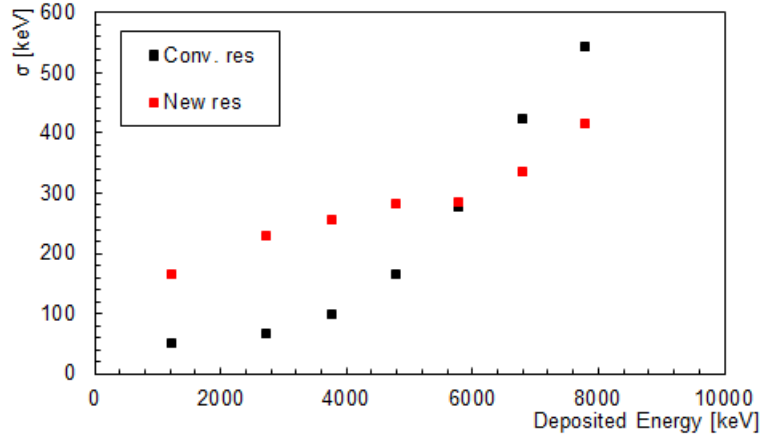
(a) 0°.
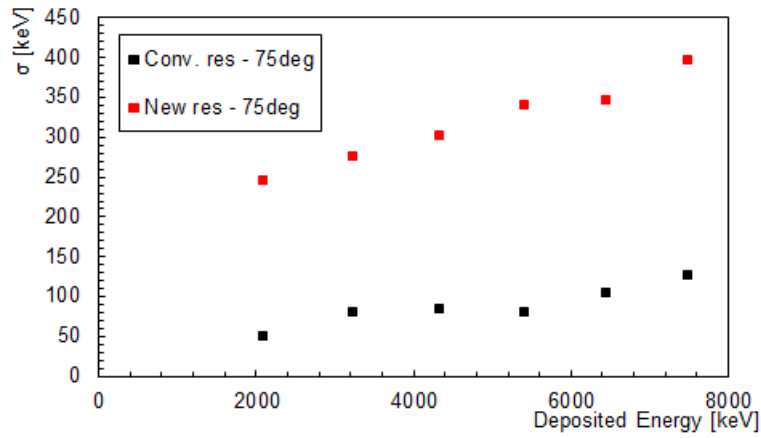
(b) 75°.

Fig. 5.3.4. Comparison between the resolutions, expressed as the standard deviation of the gaussian function fitted to each energy distribution, for proton energies reconstructed using the conventional (black) and new (red) calibrations at a) 0° incidence, and b) 75° incidence.

number of pixels was deemed equally arbitrary. Therefore, the single-pixel assumption was chosen for the advantage of allowing the user to easily implement a single pixel calibration, as is done in the conventional calibration, and the proton energies were selected to accommodate that choice.

This procedure appears to be most successful for heavy blobs at the low MeV range, suggesting an advantage in its use in the previously mentioned neutron studies, where the range in energy of secondary particles is squarely within the range evaluated in the present investigation.

5.3.6. Conclusion

An extension to the conventional per-pixel TPX3 calibration was developed to correct energy saturation effects that become present at high particle energies. The efficiency of the new high energy calibration was evaluated for heavy ionizing particles (H, Li, and C ions) for deposited energies ranging between 1 - 25 MeV. In all cases, the high energy calibration improved energy reconstruction capabilities by reducing the share of charge which is lost through saturation effects. This resulted in more accurate energy reconstructions. An increase in accuracy came at the cost of a deteriorated resolution, which was observed to increase in most cases, with more significant deteriorations for measurements at high angles of incidence. In other words, the reconstructed energy was observed to be closer to the expected deposited energy but was less resolved compared to the conventional calibration technique.

The applicability of this calibration technique can be supported by two important features. Firstly, this is a simple technique to execute as it requires the additional calibration points to be heavy blob-producing particles (like protons or higher Z nuclei such as alphas or Li ions), that have low MeV energies. The energy ranges necessary for these particles being roughly 1-4 MeV. These particles can be produced at most Van de Graaff beam facilities. Alternatively, a realistic option would be to use a radioactive source, such as ^{241}Am, which produces ^{4}He at an energy of 5.486 MeV. The drawback of the source option is that, from a practical point of view, the calibration time is dependent upon the activity of the source. In the present study, although a source was available, it was much more efficient to use proton beams to achieve the minimum of 200 hits per pixel. Secondly, this method has been designed to be complementary to the existing conventional calibration technique, used in the ATLAS-TPX collaboration, for instance. It thus requires minimal additional software resources for a user tasked with performing it.

Improvements to this calibration are needed to address several weaknesses. The corrected energy can be more accurately calculated if the energy volume profile of the cluster is modelled precisely. In the current approach, the energy is assumed to have been lost in

the central pixel. While this may work for low MeV protons, whose cluster sizes are small, this becomes increasingly inaccurate as calibration particle energies and their cluster sizes increase. In that case, charge is lost over a greater number of pixels. Future work that builds upon this framework must therefore address the challenge of obtaining good models for the volume profiles of clusters. This would also allow one to more accurately target the critical energy at which saturation begins and apply corrections to the appropriate number of pixels.

Acknowledgements

Conclusion

The ATLAS-TPX collaboration can be described in terms of two facets: 1) detector development, characterization, and testing and 2) implementation and analysis of ATLAS data. The work presented in this thesis serves as a complement to the ongoing operation of the ATLAS-TPX3 network at the LHC by means of a thorough and controlled investigation into several aspects of this detector's operation, relevant to its function in the ATLAS-TPX context. While this was the motivation and guiding principle of the presented studies, the results obtained herein are applicable in contexts beyond the scope of ATLAS-TPX. Similarly, many methods and results are also applicable and can be of interest beyond the scope of Timepix or Timepix3 detectors. These methods, within certain limitations, can be applied more generally to similar high granularity, hybrid pixel semiconductor detectors.

The tolerance of the detector to temperature variation was evaluated, with results revealing an effect on clustering and energy reconstruction. This is consequential in the ATLAS cavern, where cooling systems for TPX3 devices are impractical — if not impossible — to install, and where the high volume of surrounding equipment makes heat transfer away from the sensor more difficult. Not only is this of interest in the ATLAS context, but significantly so for any vacuum measurements in which TPX3 might be found, such as those in space missions and on satellite experiments.

The indication that temperature could affect clustering motivated the need to investigate all other conceivable factors that could affect it too. As clustering is the main method of particle identification in the ATLAS-TPX and ATLAS-TPX3 programs, the study found in this thesis provides valuable insight into the parameters which all contribute towards forming

the clusters observed during and after beam collisions. Where particle identification was once reliant upon general particle types, the results obtained here show that there is a high degree of nuance that comes from a variety of physical factors.

Finally, a proposed calibration technique has been presented as a supplement to the current procedure widely used by the ATLAS-TPX3 group. This technique is easily implemented and improves energy reconstruction in the range of energies important for the ATLAS-TPX3 program — namely, the detection of neutrons through nuclear reactions and particle recoils, which generate particles in the range of 2-3 MeV. This technique reduces the impact of charge saturation, an effect which plagues all TPX and TPX3 devices, and is, therefore, far-reaching in its utility.

All of these results have allowed for the improved understanding of a family of detectors which have been in continuous use in the ATLAS experiment since 2008. As these detectors are a part of our toolkit in probing the universe, this knowledge is valuable in pursuing that goal. While it is more appealing to use a tool to arrive at a scientific result, our ability to arrive at that result is limited by our understanding of the tool itself.

References

[1] The ATLAS Collaboration et al, The ATLAS Experiment at the CERN Large Hadron Collider, *Journal of Instrumentation*, 3 (2008) S08003. `https://iopscience.iop.org/article/10.1088/1748-0221/3/08/S08003`

[2] T. Poikela et al., Timepix3: a 65K channel hybrid pixel readout chip with simultaneous ToA/ToT and sparse readout, *Journal of Instrumentation*, 9, (2014) C05013. `https://iopscience.iop.org/article/10.1088/1748-0221/9/05/C05013`

[3] P. Burian et al., Timepix3 detector network at ATLAS experiment, *Journal of Instrumentation*, 13 (2018), C11024. `https://inspirehep.net/literature/1707342`

[4] T. Billoud, C. Leroy, C. Papadatos, M. Pichotka, S. Pospisil, and J.S. Roux, Homogeneity study of a GaAs:Cr pixelated sensor by means of X-rays, *Journal of Instrumentation*, 13 (2018) P04002. `https://iopscience.iop.org/article/10.1088/1748-0221/13/04/P04002`

[5] T. Billoud, C. Leroy, C. Papadatos, M. Pichotka, S. Pospisil, and J.S. Roux, Characterization of a pixelated CdTe Timepix detector operated in ToT mode, *Journal of Instrumentation*, 12 (2017) P01018. `https://iopscience.iop.org/article/10.1088/1748-0221/12/01/P01018`

[6] A. Studen, K. Brzezinksi, E. Chesi, et al. Silicon detectors for combined MR-PET and MR-SPECT imaging, *Nuclear Instruments and Methods in Physics Research Section A: Accelerators, Spectrometers, Detectors and Associated Equipment*, 702 (2013) 88-90. `https://www.ncbi.nlm.nih.gov/pmc/articles/PMC3578311/`

[7] G. Reitz, R. Beaujean, E. Benton et al. Space radiation measurements on-board ISS — the DOSMAP experiement, *Radiation Protection Dosimetry*, 116, (2005) 374-379. `https://pubmed.ncbi.nlm.nih.gov/16604663/`

[8] N. Stoffle et al, Timepix radiation environment monitor measurements aboard the International Space Station, *Nuclear Instruments and Methods in Physics Reasearch A.* 782 (2015) 143-148 144. `https://www.sciencedirect.com/science/article/abs/pii/S0168900215001977`

[9] C. Granja et al, The SATRAM Timepix spacecraft payload in open space on board the Proba-V satellite for wide range radiation monitoring in LEO orbit, *Planetary and Space Science.* 125 (2016) 114-129 115. `https://www.sciencedirect.com/science/article/abs/pii/S0032063316300216`

[10] NASA, *Low Earth Orbit Spacecraft Charging Design Handbook*, NASA 2007. `https://standards.nasa.gov/sites/default/files/standards/NASA/A/0/nasa-hdbk-4006a.pdf`

[11] R. Filgas et al, RISEPix—A Timepix-based radiation monitor telescope onboard the RISESAT satellite, *Astronomische Nachrichten.* 340(7) (2019) 674-680. `https://onlinelibrary.wiley.com/doi/10.1002/asna.201913674`

[12] R. Gaza et al, Comparison of novel active semiconductor pixel detector with passive radiation detectors during the NASA Orion Exploration Flight Test 1 (EFT-1), *Radiation Measurements.* 106 (2017) 290. `https://www.sciencedirect.com/science/article/pii/S135044871730224X`

[13] W.H. Bell, L. Casagrande, C. Via et al. Temperature dependence of the charge collection efficiency in heavily irradiated silicon detectors, *Nuclear Instruments and Methods in Physics Research Section A: Accelerators, Spectrometers, Detectors and Associated Equipment*, 435 (1999) 187-193. `https://www.sciencedirect.com/science/article/abs/pii/S0168900299004398?via%3Dihub`

[14] L. Beattie et al, Dependence of Depletion and Capacitance on Temperature and Frequency in Heavily Irradiated Silicon Diodes, *ROSE Technical Note.* 97/4 (1997) `https://www.sciencedirect.com/science/article/abs/pii/S0168900202013530?via%3Dihub`

[15] M. Urban, D. Doubravova, Timepix3: Temperature influence on X-ray measurements in counting mode with Si sensor, *Radiation Measurements.* 141 (2021). `https://www.sciencedirect.com/science/article/abs/pii/S1350448721000184#:~:text=It%20was%20found%20that%20the,the%20incident%20X%2Dray%20energy.`

[16] J. Jakubek, Precise energy calibration of pixel detector working in time-over-threshold mode, *Nuclear Instruments and Methods in Physics Research A.* 633 (2011) S262. `https://www.sciencedirect.com/science/article/abs/pii/S0168900210013732`

[17] M. Kroupa et al., Techniques for precise energy calibration of particle pixel detectors, *Rev. Sci. Instrum.* 88 (2017) 033301. `https://aip.scitation.org/doi/10.1063/1.4978281`

[18] D. Turecek and J. Jakubek, Dependence on temperature and pixel threshold of the calibration for the Timepix detector and its correction method, *Journal of Instrumentation.* 8 (2013) C01010. `https://iopscience.iop.org/article/10.1088/1748-0221/8/01/C01010`

[19] M. Kroupa et al, A semiconductor radiation imaging pixel detector for space radiation dosimetry, *Life Sciences in Space Research.* 6 (2015) 69. `https://www.sciencedirect.com/science/article/abs/pii/S2214552415000620`

[20] C. Leroy, C. Papadatos, M. Usman, and M. Boussa, Temperature effects on clustering in TPX3-Si pixel detectors, *Journal of Instrumentation.* 16 (2021) P09007. `https://iopscience.iop.org/article/10.1088/1748-0221/16/09/P09007`

[21] C. Leroy, C. Papadatos, M. Usman, and M. Boussa, Charge sharing investigation in a Timepix3 (TPX3) detector through ion probing, *Journal of Instrumentation.* 16 (2021) P11020. `https://iopscience.iop.org/article/10.1088/1748-0221/16/11/P11020/meta`

[22] C. Leroy, C. Papadatos, A proposed energy calibration procedure taking into account high per pixel energies using a silicon TPX3 detector, *Nuclear Instruments and Methods in Physics Research A. submitted for publication — under review.*

[23] P. Roos, *Semiconductor Detectors*, Handbook of Nuclear Medicine and Molecular Imaging for Physicists: Instrumentation and Imaging Procedures, Volume I (2022),129.

[24] G. Valchev et al. *Contemporary review of commercially available medical X-ray detectors.* Varna Medical Forum. (2022). `https://journals.mu-varna.bg/index.php/vmf/article/view/8162`

[25] D. Baudin et al. *IDeF-X HDBD: low-noise ASIC for imaging spectroscopy with semiconductor detectors in space science applications.* IEEE Transactions on Nuclear Science, Volume 69, 3, 620-626,(2022). `https://ieeexplore.ieee.org/document/9684911`

[26] O. Grimm. *CdTe Sensors for Space-Based X-ray Detectors.* Advanced X-ray Detector Technologies. Springer, Cham, (2022). 109-133. `https://link.springer.com/chapter/10.1007/978-3-030-64279-2_5`

[27] M. Campbell et al, Charge collection from proton and alpha particle tracks in silicon pixel detector devices, *IEEE Nuclear Science Symposium Conference Record.* 2 (2007) 1047-1050. `https://ieeexplore.ieee.org/document/4437190`

[28] Ali Omar. *Elementary Solid State Physics.* Adison-Wesley, 4th edition, (1993). ISBN: 978-020-1607-33-8.

[29] Diamond Cubic System. `https://en.wikipedia.org/wiki/Diamond_cubic`

[30] Semiconductors.`https://en.wikibooks.org/wiki/Semiconductors`

[31] Charles Kittel. *Introduction to Solid State Physics.* John Wiley and Sons, Inc., 8th edition, (2005). ISBN: 978-047-1415-26-8.

[32] G. Ariño-Estrada, M. Chmeissani, G. de Lorenzo, M. Kolstein, C. Puigdengoles, J. García, and E. Cabruja. Measurement of mobility and lifetime of electrons and holes in a Schottky CdTe diode. *Journal of Instrumentation*, Volume 9, C12032 (2014). `https://iopscience.iop.org/article/10.1088/1748-0221/9/12/C12032`

[33] Direct and indirect band gaps.`https://en.wikipedia.org/wiki/Direct_and_indirect_band_gaps`

[34] M. Campbell. 10 years of the Medipix2 Collaboration. *Pixel Detectors: From Fundamentals to Applications, Particle Acceleration and Detection.* ISBN 978-3-540-28332-4. Springer-Verlag Berlin Heidelberg, 2006, 01 (2006). `https://www.sciencedirect.com/science/article/abs/pii/S0168900210012969`

[35] X. Llopart, R. Ballabriga, M. Campbell, L. Tlustos, W. Wong. Timepix, a 65k programmable pixel readout chip for arrival time, energy and/or photon counting measurements. *Nuclear Instruments and Methods in Physics Research Section A*, Volume 581, 485-494, (2007). `https://www.sciencedirect.com/science/article/abs/pii/S0168900207017020`

[36] N. Asbah on behalf of the ATLAS and Medipix2 Collaborations. Luminosity Monitoring in ATLAS with MPX Detectors. *Astroparticle, Particle, Space Physics and Detectors for Physics Applications*, 317-326, (2014). `https://www.worldscientific.com/doi/abs/10.1142/9789814603164_0048`

[37] The ATLAS collaboration. ATLAS Experiment — Detector and Technology. `https://atlas.cern/Discover/Detector`

[38] P. Burian, P. Broulim, M. Jara, V. Georgiev, B. Bergmann, Katherine: Ethernet Embedded Readout Interface for Timepix3, *Journal of Instrumentation.* 12 (2017) C11001. `https://iopscience.iop.org/article/10.1088/1748-0221/12/11/C11001`

[39] J. Ziegler. Stopping and Range of Ions in Matter. `http://www.srim.org/`

[40] William R. Leo. *Techniques for Nuclear and Particle Physics Experiments.* Springer, 2nd revised edition, (1994). ISBN: 978-038-7572-80-2.

[41] H. Bethe and J. Ashkin. *Experimental Nuclear Physics*, ed. E. Segre, J. Wiley, New York, (1953), p. 253.

[42] C. Leroy, P-G. Rancoita. *Principles of Radiation in Matter and Detection.* World Scientific (Singapore), 4th edition, (2016). ISBN: 978-981-4603-18-8.

[43] H. Bichsel. *Straggling in thin silicon detectors*, Reviews of Modern Physics. 60, 3, 663 - 669, (1988). `https://journals.aps.org/rmp/abstract/10.1103/RevModPhys.60.663`

[44] N. J. Carron. *An Introduction to the Passage of Energetic Particles through Matter.* CRC Press, Tayler and Francis Group, (2007). ISBN: 978-0-7503-0935-6. `https://library.oapen.org/handle/20.500.12657/50879`

[45] K. A. Olive et al (Particle Data Group). Review of Particle Physics. *Chin. Phys*, Volume C38, 090001, (2014). `https://iopscience.iop.org/article/10.1088/1674-1137/38/9/090001`

[46] Shielding of Gamma Radiation Page. `http://www.nuclear-power.net/nuclear-power/reactor-physics/atomic-nuclear-physics/radiation/shielding-of-ionizing-radiation/shielding-gamma-radiation/`

[47] F. Berghmans et al., An introduction to radiation effects on optical components and fiber optic sensors, *Optical Waveguide Sensing and Imaging*, (2008) 127-165. `https://link.springer.com/chapter/10.1007/978-1-4020-6952-9_6`

[48] B. Bergmann et al. Relative luminosity measurement with Timepix3 in ATLAS, *Journal of Instrumentation*, 15 (2020) C01039. `https://iopscience.iop.org/article/10.1088/1748-0221/15/01/C01039`

[49] F. Krummenacher, Pixel detectors with local intelligence: an IC designer point of view, *Nuclear Instruments and Methods in Physics Research Section A.* 305 (1991) 527. C01079. `https://www.sciencedirect.com/science/article/abs/pii/016890029190152G`

[50] P.Burian et al., Katherine: Ethernet Embedded Readout Interface for Timepix3, *Journal of Instrumentation*, 12 (2017) C11001. `https://iopscience.iop.org/article/10.1088/1748-0221/12/11/C11001`

[51] N. Asbah, C. Leroy, S. Pospisil, P. Soueid, Measurement of the efficiency of the pattern recognition of tracks generated by ionizing radiation in a TIMEPIX detector, *Journal of Instrumentation.* 9 (2014) C05021. `https://iopscience.iop.org/article/10.1088/1748-0221/9/05/C05021`

[52] P. Burian, private communication.

[53] J. Bouchami et al., Study of the charge sharing in silicon pixel detector by means of heavy ionizing particles interacting with a Medipix2 device, *Nuclear Instruments and Methods in Physics Research A.* 633, (2011). `https://ieeexplore.ieee.org/document/4774668`

[54] M. Kroupa et al., Energy resolution and power consumption of timepix detector for different detector settings and saturation of front-end electronics, *Journal of Instrumentation*, 9 (2014), C05008. `https://iopscience.iop.org/article/10.1088/1748-0221/9/05/C05008`

[55] T. Holy et al., Pattern recognition of tracks induced by individual quanta of ionizing radiation in Medipix2 silicon detector, *Nuclear Instruments and Methods in Physics Research A.* 591, 1 (2008) 287-290. `https://www.sciencedirect.com/science/article/abs/pii/S0168900208004592?via%3Dihub`

[56] J. Bouchami et al., Fast neutron detection efficiency of ATLAS-MPX detectors for the evaluation of average neutron energy in mixed radiation fields, *Nuclear Instruments and Methods in Physics Research A.* 633 (2011) S226-S230. `https://www.sciencedirect.com/science/article/abs/pii/S0168900210013641`

[57] C. Granja et al., Response of the pixel detector Timepix to heavy ions, *Nuclear Instruments and Methods in Physics Research Section A.* 633, S198-S202, (2011). `https://www.sciencedirect.com/science/article/abs/pii/S0168900210013562`

[58] S. Hoang et al., Data Analysis of Tracks of Heavy Ion Particles in Timepix Detector, *Journal of Physics: Conference Series*, 523,(2014), 012026. `https://iopscience.iop.org/article/10.1088/1742-6596/523/1/012026`

[59] S.P. George et al., Very high energy calibration of silicon Timepix detectors, *Journal of Instrumentation*, 13 (2018), P11014. `https://iopscience.iop.org/article/10.1088/1748-0221/13/11/P11014`

[60] Y. Mora, private communication.

Appendix A

Calibration Code

The following is the code written to process the data files for use in the high energy calibration technique:

```
#include <stdio.h>

#include <stdlib.h>

#include <iostream>

#include <fstream>

#include "TROOT.h"


using std::cout; using std::cerr;

using std::endl; using std::string;

using std::ifstream;

using namespace std;


void hicalib2(){


string filename("test.txt");

FILE *fp = fopen(filename, "r");

FILE *newfile = fopen(filename, "w");
```

```c
if(fp == NULL){

perror("Unable to open file!");

exit(1);

}


char chunk[200];  // 1 array for each line of text

int i = 1;


while(fgets(chunk, sizeof(chunk), fp) != NULL && i < 38) {  //reads each line from 1-37


fputs(chunk, stdout);

fputs(chunk, newfile);

i++;

}


int values[1000000000000][100]; //creates the table of values for lines 38 and up

while(fgets(values[i], sizeof(values[i]), fp) != NULL && i > 37){ //reads the first line

fgets(values[i][j],sizeof(values[i][j]));

fputs(values[i][j], stdout);

fputs(values[i][j], newfile);

i++

}


int number;

ifstream input_file(filename);

while (input_file >> number){

cout << number<< "; ";

}
```

```
cout << endl;

fclose(fp);

fclose(newfile);


}
```